The influence of engineered and non-engineered Nanoparticles on mesenchymal stromal cells: implications for toxicity and applications

vorgelegt von
Dipl.-Ing.
Frank Schulze
geboren in Potsdam-Babelsberg

von der Fakultät III – Prozesswissenschaften
der Technischen Universität Berlin
zur Erlangung des akademischen Grades

Doktor der Ingenieurwissenschaften
- Dr.-Ing. -

genehmigte Dissertation

Promotionsausschuss:

Vorsitzender: Prof. Vera Meyer
Gutachter: Prof. Georg N. Duda
Gutachter: Prof. Roland Lauster

Tag der wissenschaftlichen Aussprache: 31. Juli 2015

Berlin 2015

List of content

List of Figures

List of Tables

List of Abbreviations

Abbreviation	Full term
ALP	Alkaline phosphatase
A-PVA	Amino-Polyvinyl alcohol
A-PVA-SPION	Amino-Polyvinyl alcohol superparamagnetic iron oxide nanoparticle
AR	Alizarin Red
AVN	Avascular necrosis
BMP	Bone morphogenetic protein
BSA	Bovine serum albumin
CFU	Colony forming unit
CoC	Ceramic-on-ceramic
CoCr	Cobalt-chrome
CoCrMo	Cobalt-chrome-molybdenum
CoM	Ceramic-on-metal
CoP	Ceramic-on-polyethylene
CXCR4	C-X-C chemokine receptor type 4
DAPI	4′,6-Diamidin-2-phenylindol
DEA	Diethanolamine
DMEM	Dulbecco's modified Eagle's medium
dUTE	Difference Ultra-short Echo time
EDTA	Ethylenediaminetetraacetic acid
EGF	Endothelial growth factor
FCS	Fetal calf serum
FGF	Fibroblast growth factor
FTIR	Fourier Transformation Infrared spectroscopy
hMSC	Human mesenchymal stromal cell
HIF	Hypoxia inducible factor
ICP-OES	Inductively coupled plasma optical emission spectrometry
IL-1	Interleukin-1
IL-1β	Interleukin-1 beta
IL-6	Interleukin-6
ISCT	International Society for Cellular Therapy
ISDD	*In vitro* Sedimentation, Diffusion and Dosimetry model
ITS	Insulin-Transferrin-Selenium
MACS	Magnetic Activated Cell Sorting
MHC	Major histocompatibility complex
MIM-1	Myb-induced myeloid protein-1
MMP-14	Matrix metalloproteinase 9
MMP-9	Matrix metalloproteinase 9
MNP	Metallic nanoparticle
MoM	Metal-on-Metal
MoP	Metal-on-Polyethylene
MRI	Magnetic resonance imaging

Abbreviation	Full term
MSC	Mesenchymal stromal cell
M-SCF	Monocyte colony stimulating factor
NET-trap	Neutrophil extracellular trap
NJR	National Joint Registry of England, Wales and Northern Ireland
NP	Nanoparticle
OA	Osteoarthritis
OB	Osteoblast
OECD	Organisation for Economic Co-operation and Development
OPG	Osteoprotegerin
PAK-1	Serine/threonine-protein kinase 1
PB	Phosphate buffer
PBS	Phosphate buffered saline
PE	Polyethylene
PET	Positron emission tomography
PLAUR	Plasminogen activator, urokinase receptor
PMMA	Polymethyl-methacrylate
*p*NPP	*p*-nitrophenyl phosphate
PTK 2	Protein tyrosine kinase 2
PVA	Polyvinyl alcohol
QD	Quantum dot
RA	Rheumatoid arthritis
RANKL	Receptor activator of nuclear factor κB ligand
rMSC	Rat mesenchymal stromal cell
ROCK1	Rho-associated, coiled-coil-containing protein kinase 1
ROM	Range of motion
ROS	Reactive oxygen species
S1P	Sphingosine 1-phosphate
SDF-1	Stromal cell-derived factor 1
SDS	Sodium dodecyl sulphate
SPECT	Single-photon emission computed tomography
SPION	Superparamagnetic iron oxide nanoparticles
TEM	Transmission Electron Microscopy
TGF-β1	Transforming growth factor beta one
THA	Total hip arthroplasty
THR	Total hip resurfacing
TNF-α	Tumor necrosis factor alpha
Tris-HCl	Tris(hydroxymethyl)-aminomethan-HCl
TXM	Transmission X-Ray microscopy
UHMWP	Ultrahigh-molecular-weight polyethylene
UniGen	University of Geneva
UTE	Ultra-short Echo time
UV	Ultraviolet
VEGF-A	Vascular endothelial growth factor A

Deutsche Zusammenfassung

Nanopartikel (NP) gehören zur Klasse der Nanomaterialien die, im Vergleich zu ihren makroskopischen Gegenstücken, eine Reihe ungewöhnlicher Eigenschaften besitzen, die sie interessant für die Anwendung in Industrie, Wissenschaft und Medizin machen. NP können als „nicht-gefertigt“ klassifiziert werden wenn ihre Entstehung das Resultat natürlicher Umweltprozesse oder ungerichteter menschlicher Aktivität ist und als „gefertigt“ wenn sie das Produkt gezielter menschlicher Herstellung. Die ungewöhnlichen Eigenschaften der NP resultieren möglicherweise in negativen Effekten auf biologische Systeme wie einzelne Zellen oder mehrzellige Organismen. Aus diesem Grund rückt der Einfluss von NP auf Mensch und Umwelt in den letzten Jahrzenten immer stärker in den Fokus der Wissenschaft. In dieser Arbeit werden gefertigte und nicht-gefertigte NP, die eine Rolle im Kontext von Diagnose und Behandlung muskuloskeletaler Erkrankungen spielen, hinsichtlich ihrer Effekte auf Mesenchymale Stromazellen (engl. MSC) analysiert. Amino-polyvinyl-alcohol beschichtete superparamagnetische Eisenoxid NP (engl. A-PVA-SPIONS) wurden als theranostisches Werkzeug im Kontext arthritischer Erkrankungen entwickelt und stellen das Beispiel für gefertigte Nanopartikel. A-PVA-SPIONs werden *in vitro* von humanen MSCs (engl. hMSCs) internalisiert und finden sich in intrazellulären Vesikeln und als zytosolisch vorliegende NP wieder. A-PVA-SPIONs sind nicht toxisch gegenüber hMSCs und haben keinen Einfluss auf deren Fähigkeit zur Differenzierung in andere Zell-Arten. Überraschenderweise war die Migrationsrate der hMSCs erhöht. Die A-PVA-SPIONs konnten zur Visualisierung von hMSCs durch Magnetresonanztomographie (engl. MRI) *in vitro* und *in vivo* genutzt werden. Im Tierversuch an der Ratte resultierte die intravenöse Gabe von A-PVA-SPIONs in einer Akkumulation der NP im Knochenmark, was die metabolische Aktivität und Migrationsrate der lokalen Ratten-MSCs (engl. rMSC) erhöhte. Zusammenfassend haben A-PVA-SPIONs keine nachteiligen Einflüsse auf hMSCs und rMSCs. Jedoch ist ein Einfluss auf die Biologie dieser Zellen evident, welcher weitere Forschung nötig macht. Im MRT erlaubt der Einsatz von A-PVA-SPIONs die Visualisierung von markierten hMSCs und kann auch als Kontrastmittel im Knochenmark benutzt werden. Nanoskalige Metallpartikel (MNPs) können als Folge von Abrieb in Metallimplantaten *in situ* generiert werden und stellen das Beispiel für nicht-gefertigte NP. Die Präsenz von Abrieb-MNPs hat erhöhte Konzentrationen von Kobalt und Chrom in der periprosthetischen Region zur Folge und verursacht außerdem ein verringertes osteogenes Potential der lokalen hMSCs. Die Exposition mit *in-situ* generierten MNPs hat den Verlust des osteogenen Differenzierungspotentials der hMSCs zur Folge und stellt somit ein unakzeptables Risiko für den Patienten dar. Die großen Differenzen hinsichtlich des Effektes von gefertigten und nicht-gefertigten NP auf MSCs in dieser Studie zeigen Beispielhaft, wie die gezielte Manipulation der physiochemischen Eigenschaften von gefertigten NP deren sicheren Einsatz ermöglicht, während die undefinierten Eigenschaften von nicht-gefertigten NP immer ein Risiko darstellen.

English Abstract

Nanoparticles (NPs) are one class of nanomaterials that exhibit unique features when compared to their bulk counterparts, making them attractive to a number of applications in industry, science and medicine. NPs can be classified as “non-engineered” when they are generated by natural processes in the environment or by unintentional anthropogenic activities and “engineered” when they are of intentional anthropogenic design. The unique properties of NPs might provoke adverse effects on biological systems such as cells and multicellular organisms. Therefore, research has focused on the influence of NP on human health and the environment within the last decades. In this work, engineered and non-engineered NPs that both play a role in the context of diagnosis and treatment of diseases in the musculoskeletal system are evaluated for their impact on mesenchymal stromal cells (MSCs). Amino-polyvinyl-alcohol coated superparamagnetic iron oxide NPs (A-PVA-SPIONs) where designed as a theranostic tool in the context of arthritic diseases and are used as examples for engineered NPs. A-PVA-SPIONs were internalized by human MSCs (hMSCs) *in vitro* and found in intracellular vesicles and as cytosolic single particles. A-PVA-SPIONs were found to be non-toxic to hMSCs and non-destructive towards their multi-lineage differentiation potential. Surprisingly, hMSC migration was increased. In MRI, A-PVA-SPION-labeled hMSCs were successfully visualized *in vitro* and *in vivo*. When administered systemically in animal experiments, A-PVA-SPIONs were found to accumulate in bone marrow and increase the rat MSCs’ (rMSC) metabolic activity and migration rate. In conclusion, A-PVA-SPIONs had no unfavorable influences on MSCs, although it became evident how sensitive their functional behavior is towards SPION-labeling. Furthermore, A-PVA-SPIONs allowed MSC-monitoring *in vivo*. In bone marrow, A-PVA-SPIONs appear suitable for contrast enhancement while the current data suggest an influence on the local rMSCs biology. The observed alterations in the MSCs biology upon A-PVA-SPION exposure *in vitro* and *in vivo* necessitate future research. Metallic nanoparticles (MNPs) can be *in situ* generated from wear of metal-on-metal hip implants, thereby exposing the local joint compartments and will serve as an example for non-engineered NPs. The presence of MoM wear MNPs leads to increased concentration of Cobalt and Chrome ions in the periprosthetic region and is accompanied by a reduced osteogenic differentiation potential of local MSCs in humans. The *in situ* generation of MoM wear NPs leads to a loss-of-function in local hMSCs thus posing an unacceptable risk for the patients’ wellbeing. The vast differences in cellular reactions by MSCs on the engineered and non-engineered NPs employed in this study, exemplify that the careful manipulation of their physiochemical properties enables the safe use of engineered NPs while non-engineered NPs always pose a potential hazard due to their undefined properties.

1. Introduction

1.1. The musculoskeletal system

1.1.1. The physiology and function of bone

The musculoskeletal system provides mechanical support for the bodies' shape, the protection of the inner organs and for locomotion. To achieve these functions, more than 200 bones are connected through rigid or articulating joints within the human body. Apart from these mechanical purposes, bone facilitates a variety of functions within the body such as forming a major reservoir for calcium, magnesium and phosphorus.[1] Furthermore, bone contains bone marrow which is of paramount importance for the formation of blood- and immune-cells by providing the niche for hematopoietic stem cells. The ability to heal fractures without the formation of scars exemplifies the excellent regenerative potential of bone. Compared to other tissues, bone undergoes significant turnover facilitated by constant tissue resorption and formation through different cell types.[2] The tissue matrix of bone is a composite material that surrounds the resident cells and consists of organic and inorganic components. The so called osteoid is the organic part of bone matrix and consist of collagens predominantly type I that make up approximately 90%. Other components of the osteoid are non-collagenous glycoproteins, bone specific proteoglycans and proteins necessary for mineralization such as alkaline phosphatase (ALP) or osteocalcin.[3, 4] The organic matrix is hardened by hydroxyapatite, the inorganic component of bone that consists of a crystalline salt of calcium and phosphorous ($[Ca_3(PO_4)_2]Ca(OH)_2$).[5] This matrix composition is common throughout the two different histological types of bone tissue termed cortical and cancellous bone. Cortical bone has a dense ordered structure, while cancellous bone is lighter and has an irregular structure. These differences in their density and porosity cause different mechanical properties. In the diaphysis of long bones and the surface of flat bones, the dense cortical bone provides resistance to torsion and bending, while cancellous bone provides mechanical flexibility and occurs at the ends of long bones and the inner of flat bones. The main functional unit of cortical bone is the osteon. Multiple layers of osteoblasts and osteocytes are located around the Haversian canal that is situated in the center of the osteon and contains blood and nerve vessels. The Haversian canals are interconnected by Volkmann's canals. On its outer surface, cortical bone is covered by the periosteum while the inner surface is covered by the endosteum that serves as a boundary between the cortical bone and the cancellous bone (**Figure 1**).[4]

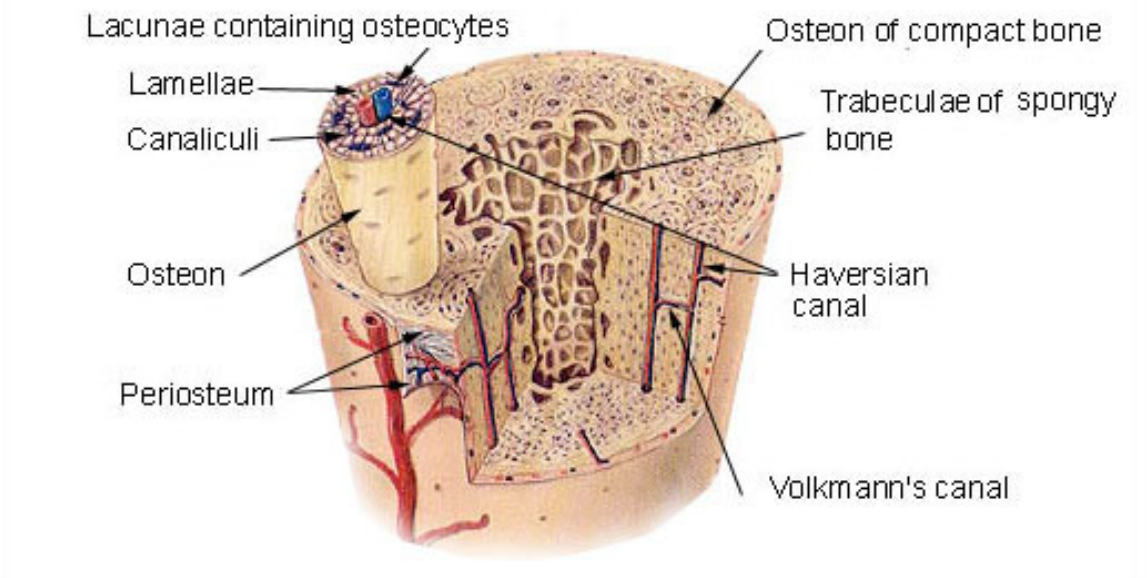

Figure 1. The physiology of bone.

Shown are the main characteristics of bone physiology

(©U.S. National Cancer Institute's Surveillance, Epidemiology and End Results [6])

In cancellous bone, the main functional unit is the trabecula that aligns according to the mechanical load a bone encounters.[7, 8] Bone marrow can be found in the cavities of cancellous bone and can be divided into the red active hematopoietic marrow and yellow inactive fat marrow. Red marrow is predominant during embryogenesis and is continuously converted to yellow bone marrow during skeletal maturation.[9, 10] In summary, bone appears rather dynamic than rigid and has various abilities and functions such as tissue repair, tissue maintenance, reacting on changing mechanical loads and retaining the body's calcium, phosphate and acid-base homeostasis. To facilitate these diverse physiological roles, bone is initially resorbed and then replaced, a process termed bone remodeling.

1.1.2. The process of bone remodeling

During the process of bone remodeling, distinct bone cells that differ in their morphology, function and characteristic location, interact with each other in a coordinated fashion (**Figure 2**).[2] The involved cells are derived from progenitors of mesenchymal and hematopoietic origin that reside in red bone marrow. Osteoblasts (OBs) are the progeny of local mesenchymal stromal cells (MSCs) and can further specialize to lining cells (also termed resting osteoblasts or surface osteocytes) and to osteocytes.[11-13] The hematopoietic line gives rise to the multinucleated osteoclasts.[14, 15] These four different cell types coordinately interact with each other to continuously resorb and restore bone tissue matrix. The process of bone remodeling starts with lining cells that lie directly against the surface of bone. Lining cells possess cytoplasmic extensions that penetrate bone matrix and come into contact with embedded osteocytes. When confronted with external cues such as parathyroid hormones lining cells can secrete proteolytic enzymes to remove the thin layer of non-mineralized fibrous tissue that covers the mineralized matrix.[4] Bone resorption is then facilitated by multinucleated osteoclasts which originate from mononucleated precursor cells that proliferate and fuse in response to monocyte colony stimulating factor (M-SCF) and receptor activator of nuclear factor κB ligand (RANKL), respectively.[16, 17] RANKL is thought to be expressed by lining cells at the sites of bone resorption but can also be secreted by osteoblasts. The expression of RANKL is up-regulated in response to the expression of inflammatory cytokines such as interleukin-1 (IL-1) or tumor necrosis factor α (TNF-α).[18] Osteoclasts facilitate bone resorption by tightly binding to the surface of the mineralized bone. For this, they make use of a complex folded cytoplasmic membrane that is termed ruffled border and is used to create a sealed space. The mineralized part of the bone matrix is then degraded by lowering the pH within this sealed space from approximately 7 to 4. This acidification is facilitated by the fusion of proton pump containing vesicles with the cell membrane of the ruffled border.[4, 19] The remaining organic matrix is degraded through secretion of acid proteases such as cathepsin K or matrix metalloproteinase 9 (MMP-9).[20, 21] In addition, remaining matrix fragments might be phagocytized and further degraded within cytoplasmic vacuoles of the osteoclast. The termination of this bone resorbing activity is accompanied by the apoptosis of osteoclasts and is followed by the recruitment of osteoblasts. The attraction and differentiation of osteoblasts might be facilitated through chemokines that are liberated in the course of bone matrix degradation (e.g. bone morphogenetic proteins (BMPs) or fibroblast growth factors (FGFs)) and by secretion products of osteoclasts (e.g. sphingosine 1-phosphate (S1P), myb-induced myeloid protein-1

(mim-1)).[18, 22-24] Recruited osteoblasts then start to form new bone matrix by synthesis and secretion of the osteoid components such as collagens and proteins.[25] After the organization of collagen fibrils, the osteoblasts start to mineralize the organic matrix and eventually became entrapped by the bone matrix they created. They then turn into a quiescent state and become terminally differentiated osteocytes with a significant reduced ability to form new bone, while those osteoblasts not entrapped by their matrix will undergo apoptosis.[26] Osteocytes constitute 90% of adult bone cells and interact with other cells through a network of dendritic processes that run inside lacunar canaliculi. There is increasing evidence that osteocytes can act as mechanosensors through their processes within the bone and are able to govern the remodeling process in response to altered mechanical loading.[12] Bone resorption and formation of new bone are usually in balance, resulting in a permanent remodeling of bone according to mechanical and biochemical stimuli. Bone pathologies can arise when the number or function of the different cell types involved in bone remodeling is altered. However the most prevalent causes for disabilities of the musculoskeletal system are diseases that affect the bodies' joints.

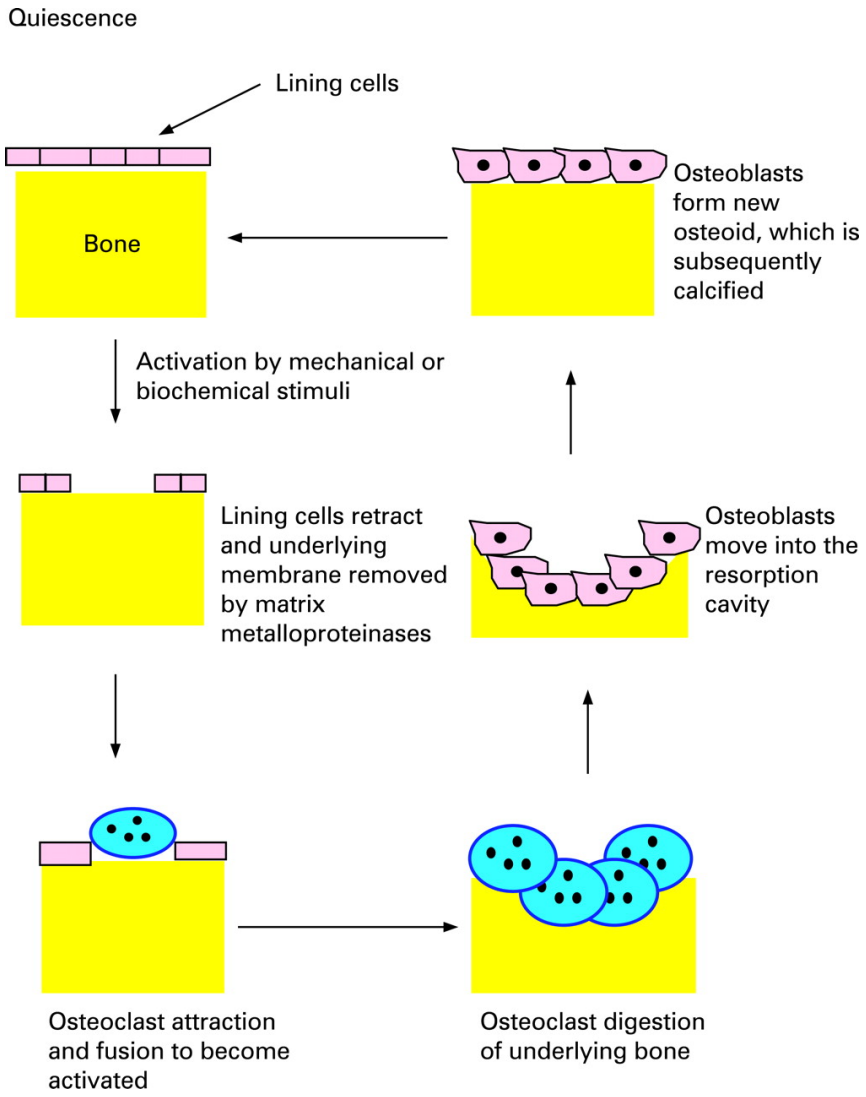

Figure 2. The cyclic activities of osteoclasts and osteoblasts in bone remodelling.

Shown is a schematic representation of the bone remodelling process and the cells involved.

(© Journal of clinical pathology [2])

1.1.3. Degenerative diseases of the musculoskeletal system affecting the hip joint

The hip joint, also referred to as the acetabulofemoral joint, provides the connection between the lower extremities and the pelvis. Its primary function is to facilitate bipedal locomotion by supporting the weight of the body in static and dynamic postures. The hip joint is classified as a synovial joint, where the articulating surfaces are separated by a joint cavity (**Figure 3 A**). The articulating surfaces are covered with cartilage and enclosed by the joint capsule that consists of the outer fibrous membrane and the inner synovial membrane. The joint capsule is filled with synovial fluid to reduce friction between the articulating surfaces by providing constant lubrication. There are six different types of synovial joints that can be classified according to their general anatomy and the range of motion (ROM) that they allow for. The hip joint belongs to the class of ball-and-socket joints, where a ball-shaped end of one bone fits into the cup-like cavity of another bone (**Figure 3 B**). This joint anatomy allows for a high ROM, since it is capable of movement around an unlimited number of axes.[27] There are several diseases that can affect the articulating surfaces of the hip joint and make medical intervention necessary.

Osteoarthritis (OA) is one of the most widespread disabling diseases and affects approximately 10% of men and 18% woman worldwide.[28] In OA the articulating surfaces of the synovial joint are characterized by a thinned out and sometimes irregular cartilage layer. It is believed that OA primary develops as a consequence of a mechanical trauma of the joints articulating surfaces.[29, 30] Secondary factors that influence disease progression might be found in overweight or intense physical labor on a regular basis. The physical changes in the cartilage layer are early events in the disease progression and coupled to other alterations in the joint. To compensate the higher mechanical load on the worn articulating surfaces, more synovial fluid is produced within the joint that causes swelling which can reach a painful state. In addition, subchondral bone thickens and becomes irregular thereby causing the overlying cartilage layer to become irregular too which causes small bumpers on the articulating surfaces, unlike the smooth layer of cartilage found in healthy joints (**Figure 3 C**).[31] The destruction of the cartilage layer also causes the release of matrix molecules and fragments that are believed to trigger a local inflammation within the joint capsule, thus worsening the process of cartilage destruction.[32] In consequence, the cartilage layer of the joint degenerates until the bones grind on each other, causing severe pain and immobility.

Rheumatoid arthritis (RA) is a complex autoimmune disease where a persistent synovial inflammation leads to the damage of cartilage and subchondral bone. In industrialized countries, 0.5–1.0% of the adult population develops signs of RA. The progression of RA is mainly attributed to genetic predispositions and affects mostly woman and elderly people.[33] Smoking is believed to be the main secondary risk for RA. The joints affected in RA usually involve hands, feet, and cervical spine but can also include the hip joint. RA might also be associated with lung fibrosis, vasculitis, coronary heart disease and premature mortality.[34] The pathology of RA is characterized by several inflammatory cascades with differences in the underlying mechanisms that all lead to a final common pathway that causes a persistent synovial inflammation. One key inflammatory cascade involves the overexpression of TNF-α which affects T and B lymphocytes, synovial cells and macrophages. In turn, these cells overproduce cytokines such as interleukin-6 (IL-6) that drive the inflammation processes in the joints.[35-37] Another characteristic in the pathology of RA is the production of autoantibodies that are directed against immunoglobulin G or citrullinated peptides.[34] Similar to the disease progression in OA, the destruction of the joint's chondrogenic layers causes deformations, a loss of mobility and pain ultimately leading to severe disability.

Avascular necrosis (AVN), also termed osteonecrosis, is characterized by the necrosis of bone tissue due to the interruption of local blood supply.[38, 39] AVN has a high prevalence in young patients and most commonly occurs in the upper femur but can also affect the humerus and the knee or shoulder joint.[40] Till date, the exact pathophysiology behind AVN remains unclear.[41, 42] Current research indicates that AVN in the upper femur including the femoral head may be associated with a premature conversion of red marrow into fatty yellow marrow that can result in alterations of the intramedullary vascularization.[39] If untreated, AVN can progresses into collapsing bone and the development of OA with all its consequences for mobility and the possibility for an early development of disability.

All of these medical conditions affecting the hip joint require medical interventions to preserve or restore the patients' mobility. Once injured, cartilage is not capable of repair or regeneration. Classical treatments of OA, RA or AVN aim to alleviate symptoms, while none of these diseases can be cured till date. Replacement through artificial joint components is an established method and is currently the only possible approach once the degeneration of the hip joints' cartilage layers reaches a state that causes pain and immobility. Novel experimental approaches aim for cartilage and bone regeneration by using cellular grafts with a special focus on the multi-potent MSC.

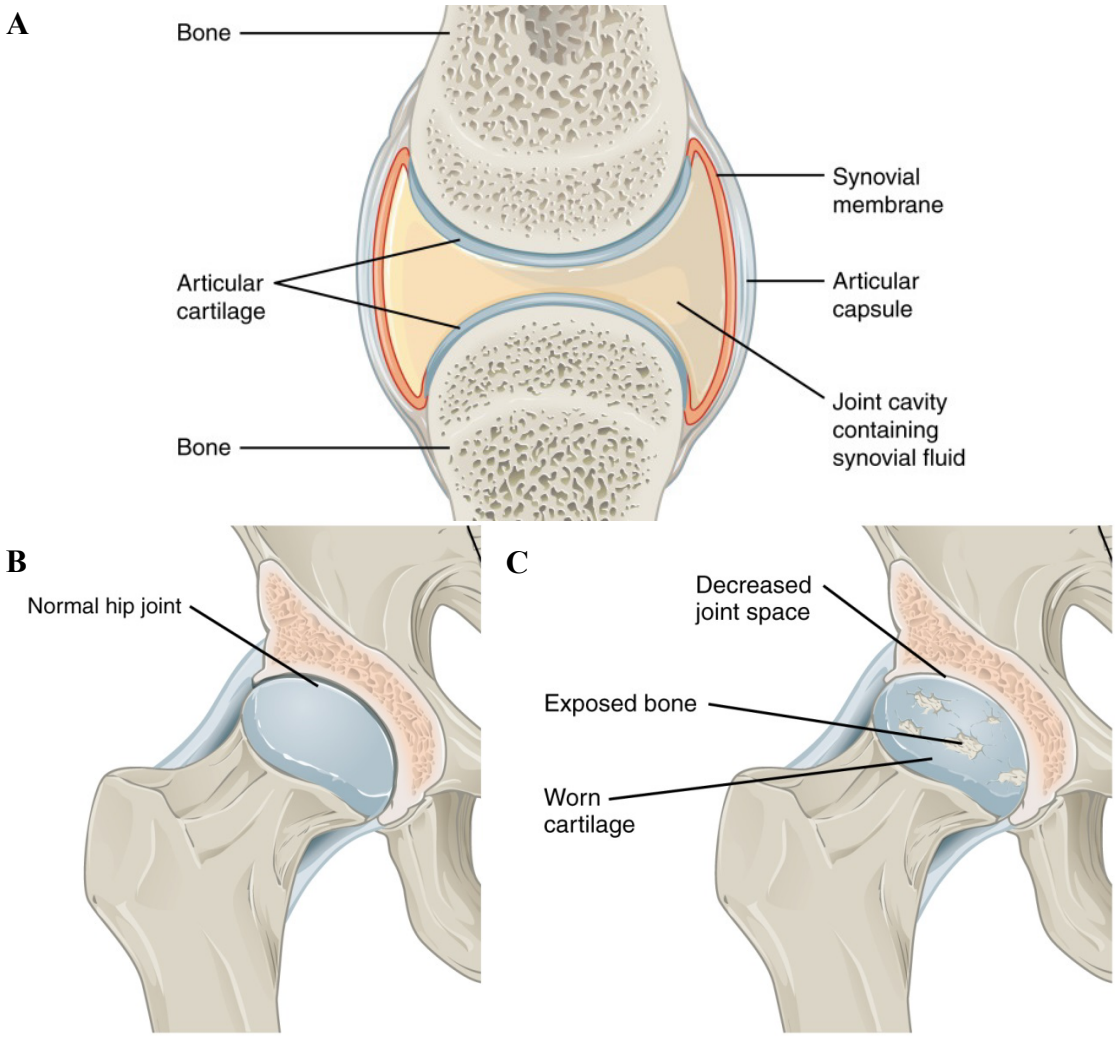

Figure 3. Anatomy of synovial joints and the hip joint.

(A) Shown is the common anatomy of synovial joints: The joint cavity is surrounded by an articular capsule and filled with synovial fluid. A thin layer of cartilage covers the opposed bone surfaces on each side of the joint, thereby allowing smooth movement. (B) Shown is the cartilage layer in the healthy and (C) arthritic hip joint. (© OpenStax [43])

1.2. Mesenchymal stromal cells

1.2.1. Mesenchymal stromal cells in bone

MSCs can be isolated from different tissues including bone marrow, fat and muscle. Till the present day, most studies use MSCs that were isolated from bone marrow by density gradient centrifugation followed by positive selection for adherence on plastic culture vessels.[44] In cell culture, the MSCs' morphology can be best described as spindle shaped fibroblast like cells. MSCs are characterized by their multi-potency, i.e. the ability to differentiate into the adipogenic, chondrogenic and osteogenic lineage in cell culture.[45] To confirm the MSCs' identity the analysis of cell surface marker can be employed. There are, however, no cell surface markers that would be unique to MSCs; instead a panel of markers is needed to identify cells with an MSC phenotype. According to the International Society for Cellular Therapy (ISCT), MSCs should express CD44, CD73, CD90 and CD105 on their surface while CD45, CD34 and CD14 should be absent.[46] MSCs are able to migrate towards injured tissue, since they express several chemokine receptors on their surface. This ability is exemplified by the expression of C-X-C chemokine receptor type 4 (CXCR4) by MSCs that binds the chemo-attractant stromal cell-derived factor 1 (SDF-1).[47, 48] Due to their ability of self-renewal, differentiation into a variety of specialized cell types and migration towards chemokine gradients, MSCs have been attributed with the potential to regenerate damaged tissue.[49] And indeed, it is well investigated that in case of bone fractures, MSCs migrate to the site of injury where they orchestrate the healing process.[50, 51] Furthermore, MSCs indirectly participate in the resorption and formation of bone by providing constant replenishment for the rather short lived osteoblasts and their progeny *in vivo*.[11] In addition, MSCs can influence RANKL mediated osteoclastogenesis by the expression of RANKL itself or the RANKL decoy receptor osteoprotegerin (OPG).[52] The MSCs' ability to interact with other types of immune cells is well described by the field of osteoimmunology.[53] For example, several studies report immunemodulatory and immunosuppressive properties of MSCs towards dendritic- and T-cells.[54-56] In turn, there is also evidence that immune cells can induce apoptosis of MSCs or modulate their regenerative functions such as differentiation into the osteogenic lineage.[57-59] In bone marrow, MSCs also participate in providing the niche for hematopoietic stem cells that are needed for the formation of the immune system.[60] These interactions with various cells of the immune system indicates that MSCs fulfill a variety of functions *in vivo* that are beyond a sole replenishment of cells. Their role in fracture healing and their involvement in bone remodeling underline that MSCs are vital for

skeletal growth, maintenance and repair. The *in vivo* functions of MSCs might be manipulated and harnessed for their application in cell-based regenerative therapies.

1.2.2. MSCs in regenerative therapies of the musculoskeletal system

MSCs have gained high interest in the context of bone and cartilage repair and the therapy of arthritic diseases since their ease of isolation and expansion in cell culture as well as their regenerative capabilities. Here, the MSCs' potential to differentiate into the osteogenic and chondrogenic lineage and their immunomodulatory properties are believed to be beneficial [39, 61, 62]. Furthermore, MSCs are thought have high potential for allotransplantation, since they express major histocompatibility complex (MHC) class I but not MHC II molecules. Thus MSCs were thought not to activate an allogeneic immune response mediated by T-Cells. And indeed, allogeneic transplantation of MSCs has been successful used to treat auto-immune diseases.[63] However, recent evidence suggests that anti-donor immune responses of the host can occur under certain circumstances.[64] For example, it is reported that the progeny of allogeneic MSC grafts might elicit immune-responses.[65] In arthritic joints, MSCs might be of use for the repair or replacement of damaged cartilage due to their chondrogenic differentiation potential. MSCs could be differentiated in a 3D scaffold to replace the impaired cartilage, or injected directly into the synovia where they could engraft, modulate the inflammation process or activate local progenitor cells.[66] The systemic injection of MSCs lead to a significant reduction of pro-inflammatory cytokines in a mouse model of RA and was able to prevent severe arthritis, while in a sheep model of OA cartilage destruction was decreased. [67, 68] Interestingly, there were no engrafted MSCs found in the joint cartilage in both studies, which raises questions about the exact mechanism behind the beneficial effects observed. The absence of transplanted MSCs in the joint cartilage indicates that their mode of action is mediated by paracrine effects rather than engraftment. However, engraftment of MSCs might be underestimated or overlooked due to limitations in the employed cell imaging methods might. In two clinical trials, MSCs were seeded into collagen type I hydrogels to repair cartilage defects in humans. In one case, two patients with a patellar defect were treated and the defect was found filled with fibrocartilaginous tissue after 1 year.[69] In the second case published by the same group, a cartilage defect in the medial femoral condyle was treated with MSCs and found filled with a hyaline-like type of cartilage indicating the chondrogenesis of grafted cells.[70] Although anecdotal, both trials exemplify how the local application of scaffold seeded MSCs can be used for the repair of cartilage

defects in humans. For AVN of the femoral head, it was demonstrated that the size of the femoral lesion can be reduced up to 75% by grafting MSCs into necrotic regions in an early stage of the disease.[71] In a different study, the application of autologous MSCs reduced the chance for severe disease progression that necessitates the replacement of the joints articulating surfaces with artificial implants.[72] Yet, another study presented conflicting results that did not indicate a positive effect of MSC transplantation on the progression of AVN.[73] Among the possible explanations for these different outcomes, cell number seems to be a limiting factor for successful MSC based treatment of AVN.[42] In summary, numerous clinical trials have been conducted and some revealed a degree of success. Yet a broad clinical application of MSCs based therapies for the treatment of degenerative conditions in the musculoskeletal system, especially the hip joint, is still not available. Critical parameters for successfully transferring results from initial trials to clinical application include the number of transplanted cell and their cultivation and delivery process.

1.2.3. Cell labeling methods for regenerative therapies

Successful implementation of cell based therapies requires information about the temporal and spatial distribution of transplanted cells. Several methods for non-invasive tracking of transplanted cells *in vivo* are available all with certain benefits and limitations. Currently, available visualization methods require either direct or indirect labeling techniques.[74] Direct labeling encompasses the use of probes such as nanoparticles (NPs), radioisotopes or fluorescent dyes that are used to detect cells by relevant imaging modalities.[74, 75] The use of direct markers can be achieved relatively easy and usually grant high contrast between the cellular graft and host tissue. However, direct labeling suffers from comparably limited observation time since the amount of applied probes diminishes over the course of mitotic division. Indirect labeling methods make use of reporter gene constructs that allow for stable cell visualization over prolonged time periods without the problem of signal decay.[75] Reporter genes used for indirect labeling encode for luciferase, green fluorescent protein or enzymes that facilitate the generation of iron oxide NPs such as ferritin or MagA.[76-78] However, a major disadvantage of this technique is the demand for genetic engineering which might interfere with the functionality of the cellular graft and also hampers clinical translation.[75] Visualization of direct or indirect labeled cells *in vivo* can be achieved by using different molecular imaging modalities such as magnetic resonance imaging (MRI), radionuclide imaging, positron emission tomography (PET), single-photon emission

computed tomography (SPECT) and optical imaging.[79, 80] Although none of these imaging techniques is optimal, MRI is still the preferred imaging modality for visualization of exogenously delivered cells, because of its non-destructive and non-invasiveness, deep penetration, high spatial resolution and widespread clinical availability.[81]

1.3. Total hip arthroplasty

1.3.1. The operation of the century

Total hip arthroplasty (THA) is an established method to restore mobility and to improve quality of live in patients that suffer from degenerative conditions of the weight-bearing surfaces in the hip joint. Due to its high incidences and its relevance in modern society, THA has also been termed "The operation of the century".[82] In 2011, approximately 1.6 million THAs were performed within 27 of the 32 member states that belong to the Organisation for Economic Co-operation and Development (OECD). More than 500.000 of these procedures were performed on patients aged 65 and younger and an absolute increase of 35% for performed THAs from the year 2005 to 2011 was reported for this part of the population.[28] These numbers reflect a change among the patients undergoing a primary THA, from elderly and infirm individuals with limited motility to rather young individuals with high expectations towards their life quality.[82] According to the 2014 report of the National Joint Registry of England, Wales and Northern Ireland, 91,4% of all patients were diagnosed with OA as the primary indication for their THA (**Table 1**). However the age of the patient strongly influences the prevalence of diagnosis that indicate the need for a primary THA other than OA. In the more elderly patient cohorts aged 60 years and older, fracture of the femur was the second most frequent indication (4.3%) followed by AVN (1.6%) (**Table 1**). For patients aged 59 and younger, hip dysplasia (6%) was the second most frequent indication followed by AVN (5.5%). This trend is more pronounced for patients younger than 30 years, were the indications for primary THA are even more differentiated with 41% suffering from OA, while 24.7% needed a primary THA due to hip dysplasia and 21.2% due to AVN.[83] Thus, not only the frequency of primary indications for THA but also the patients' expectations towards function, lifetime and general performance of modern hip implants have shifted accordingly. To meet the individual requirements of patients, hip implants of varying designs and material compositions are available.

Table 1. Indications for primary THA (adapted from [83]).

	≤59 years		≥60 years		all	
Indication	No.	%	No.	%	No.	%
All	3898		15293,25		9596	
Osteoarthritis	3377	86,6	14165	92,6	8771	91,4
Avascular necrosis	216	5,5	244	1,6	230	2,4
Femoral neck fracture	69	1,8	643	4,2	356	3,7
Congenital dislocation/dysplasia	236	6,0	71	0,5	153	1,6
Inflammatory atrophy	83	2,1	168	1,1	125	1,3
Failed hemi-arthroplasty	2	0,1	32	0,2	17	0,2
Trauma chronic	76	1,9	174	1,1	125	1,3
Previous Surgery, non-trauma	54	1,4	16	0,1	35	0,4
Previous Arthrodesis	3	0,1	7	0,0	5	0,1
Previous Infection	11	0,3	8	0,1	10	0,1
Other	96	2,5	148	1,0	122	1,3

1.3.2. Hip implants

In THA, the weight-bearing joint components of the patient are replaced completely by a hip endoprosthesis that usually consist of a femoral stem and head and an acetabular cup and liner (**Figure 4 A and B I**).[84] The implants' stem and acetabular shell are usually made out of titanium and only occasionally out of stainless steel or a cobalt-chrome-molybdenum (CoCrMo) alloy. The femoral head and acetabular liner represent the implant's articulating surfaces and can be made of different materials in varying combinations. The most common pairing that is also regarded as the gold standard in THA is metal-on-polyethylene (MoP), were a CoCrMo alloy is used for the femoral head and polyethylene (PE) or ultrahigh-molecular-weight polyethylene (UHMWP) for the acetabular liner. One alternative pairing is metal-on-metal (MoM) were the articulating components of the implant are exclusively made out of a metallic CoCrMo alloy. Ceramic bearings like ceramic-on-polyethylene (CoP), ceramic-on-metal (CoM) or ceramic-on-ceramic (CoC) are also available and have gained increasing interest within last years due to the good material properties of newly developed third and fourth generation ceramics.[85] For individual patient specific fitting of the endoprosthesis, modular-neck components that are connected through taper-locks were introduced.[86] Most of these femoral taper-neck components are made out of CoCrMo alloys. These modular hip implants typically find application in primary THAs on patients that suffer from dysplastic hips and in hip implant revision of patients that already

encountered bone loss due to their primary THA and/or complications. As an alternative to THA the so called total hip resurfacing (THR) can be performed, where only the articulating surfaces of the joint are replaced by an implant (**Figure 4 B II**).[87] This technique is preferentially used in younger patients as it grants a high range of motion and preserves as much healthy bone as possible, which can be advantageous in case of later implant revisions. In THR, CoCrMo alloys are used exclusively for the whole implant, since they allow for large hollow femoral heads without the risk of implant fracture. Fixation of the implant is a requirement for successful function and can be facilitated by either using bone cement or by using implants that allow for bone ingrowth. Cementation is facilitated by using polymethyl-methacrylate (PMMA) that forms the bone-cement and the cement-implant interfaces, with the bone-cement interface being mainly responsible for durable fixation of the implant. Uncemented femoral or acetabular components have a roughened or porous surface that is designed to encourage bone ingrowth, thereby facilitating implant fixation and normal transmission of biomechanical forces. It is also possible to fix either the acetabular or femoral component with cement while the opposite part is designed for uncemented fixation, a technique termed hybrid fixation. Although THA is a generally successful procedure, it can be accompanied by complications such as pain, infection and aseptic implant loosening, with the latter one accounting for almost 50% of all revisions performed (**Table 2**).[83] MoM articulations suffer from an overall poor performance reflected by the highest revision rates among available bearings.[88, 89]

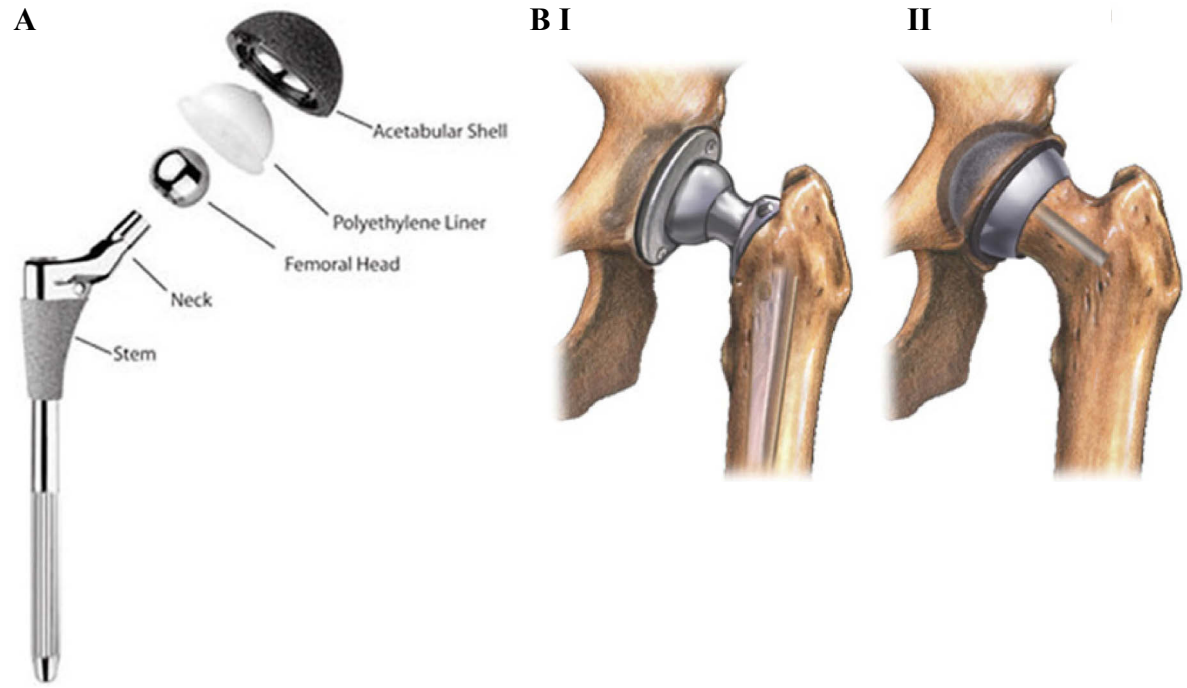

Figure 4. Hip implants in THA and THR.

(A) Shown is the general configuration of a hip implant used in THA, consisting of a stem that is fitted on the femoral head via a taper-neck connection. The femoral counterpart consists of a liner that is fitted into a metallic acetabular shell. Femoral head and liner can be made of various materials. Here, a MoP implant is depicted. (B) Shown are the differences in THA and THR regarding implant configuration and fitting. (B I) In THA the native femoral head is removed and the implants' stem is fitted into the femur, while the acetabular shell is fitted into the pelvic acetabulum. (B II) In THR the native femoral head is left intact for the most part to allow fitting of the femoral shell. ((A) was adapted from [90], (B) was adapted from [91])

Table 2. Indications for implant revision (adapted from [83]).

	Year											
	2009		2010		2011		2012		2013		5 year total	
Indication	No.	%	No.	%	No.	%	No.	%	No.	%	No.	%
All	6639		7408		8299		9449		8489		40284	
Aseptic loosening	3666	55,2	3714	50,1	3817	46,0	4146	43,9	3617	42,6	18960	47,1
Pain	2042	30,8	2010	27,1	2142	25,8	2402	25,4	1972	23,2	10568	26,2
Lysis	1000	15,1	1105	14,9	1129	13,6	1318	13,9	1128	13,3	5680	14,1
Adverse soft tissue reaction	87	1,3	411	5,5	988	11,9	1341	14,2	1309	15,4	4136	10,3
Infection	193	2,9	236	3,2	265	3,2	311	3,3	288	3,4	1293	3,2

1.3.3. Metal-on-Metal hip implants

MoM implants were introduced due to the advantageous material properties of CoCrMo alloys, such as low specific weight, corrosion-resistance, high mechanical durability and good biocompatibility of the bulk material. The widespread use of MoM bearings in THA dates back to the 1960s but their application declined in the following two decades due to disappointing initial clinical results.[92] After introduction by the orthopaedic surgeon John Charnley, hip implant designs that made use of a MoP articulation have proven to be quite successful and drew away the attention from MoM bearings in the beginning 1970s. However, a relationship between wear particles and subsequent implant loosening was discovered for MoP bearings in the late 1970s.[93, 94] Early attempts to avoid aseptic loosening aimed on the quantitative reduction of generated wear. As one solution, MoM implants with improved designs were re-introduced in late 80s.[95] The high incidence of implant failure with first generation MoM hip endoprostheses in the 1960s and 70s was mainly attributed to poor design.[96] However, some of the early MoM endoprostheses survived 20 years and more while only low amounts of wear were generated when compared to MoP implants.[97-99] Thus, MoM implants found their way back into clinical use to avoid wear related problems encountered with MoP endoprostheses. The advances made with the development of second generation MoM implants also allowed for large femoral heads that resemble the physiology of the human hip joint more closely (**Figure 5 A, B**). The use of MoM articulations solved the problem of size restrains for femoral heads to 32mm and smaller that applied for early MoP implants due to the excessive generation of polyethylene wear with larger head sizes.[99] Head sizes larger than 32mm have the advantage to increase the patients' ROM and decrease the risk for dislocation. In THR only large femoral heads are used, since the implants components have to fit in to the native anatomy of the hip joint instead of replacing them entirely. Using CoCrMo alloys in THR allows for 1) large femoral heads with a hollow design necessary to fit on its biological counterpart and 2) an acetabular component with the corresponding size without the risk of implant fracture (**Figure 5 C**). While the volumetric wear rate was remarkably reduced for new generation MoM implants, aseptic loosening and early implant failure still occurred.[88, 89, 97, 100, 101] It became evident from research that the wear particles generated from MoM implants was fundamentally different from MoP wear in terms of material composition but also, and more important, in size.[102]

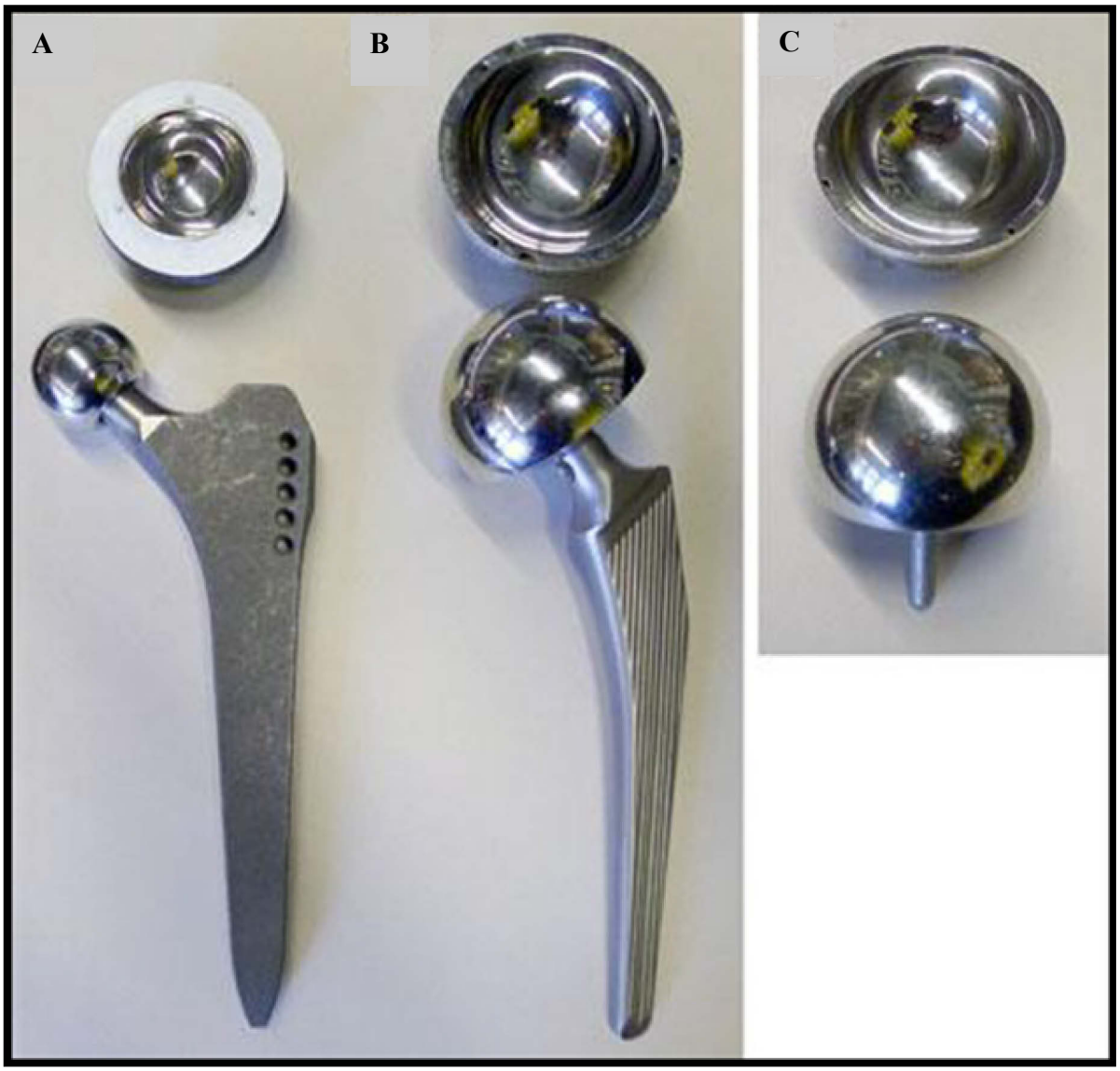

Figure 5. Different configurations for MoM implants.

Shown are examples for (A) a small head and (B) large head MoM implant used in THA and (C) the acetabular component and femoral cap used in THR.

1.4. Nanoparticles

1.4.1. The nano-scale: changing material properties without changing the material

The prefix *nano* means "dwarf" in Greek and signifies a billionth (10^{-9}) as order of magnitude. Therefore, the metric unit nanometer (nm) denotes a billionth of a meter.[103] According to the European Commission, nanomaterials are defined as "A natural, incidental or manufactured material containing particles, in an unbound state or as an aggregate or as an agglomerate and where, for 50 % or more of the particles in the number size distribution, one or more external dimensions is in the size range 1 nm - 100 nm".[104] NPs are one class of nanomaterials which exhibit unique features when compared to their bulk counterparts, making them attractive to a number of applications in industry, science and medicine.[105] NPs possess a high surface-to-volume ratio, i.e. a given quantity of nanoparticulate matter has a larger surface area than the same quantity in bulk form.[106] Thus, more atoms are represented at the surface, thereby increasing chemical reactivity (**Figure 6**). For example, a nanoparticle with a diameter of 10 nm has approximately 30 000 Atoms of which a proportion of 20% can be found on the particles surface. When reduced to a size of 5 nm, the proportion of atoms found on the surface is increased to 40% and for a nanoparticle with 1 nm in size almost all of the 30 atoms are found on its surface.[107] Surface atoms have less neighboring atoms than those embedded in the inner volume of a given material, resulting in a lower binding energy. In consequence, the transition of a bulk material into the nanoscale (e.g. as NPs) results in a decrease in melting temperature.[106] The size reduction to the nano-scale can also be associated with quantum confinement effects. These effects occur when the size dimensions of a given material are smaller than the wavelength of the electron wave function. Quantum confinement effects thus result in the deviation of electronic and optical properties of nanomaterials when compared to the properties of same material in bulk.[108] One very popular example for these effects are quantum dots (QDs) that consists of semiconductor materials with only a few nanometers in size and exhibit photoluminescence under illumination with ultraviolet (UV) light. Alternating the quantum dots size changes the wavelength of emitted light, allowing for simple and precise control of the QDs optical properties.[109] Thus, QDs are especially interesting for applications in optoelectronics, cosmetics and biomedical diagnostics.[110, 111] For magnetic materials, the transition into the nanoscale also results in a change of their specific properties. Magnetic NPs possess a single magnetic domain instead of multiple ones found in bulk magnetic materials. They can be therefore only magnetized in one direction, a property that

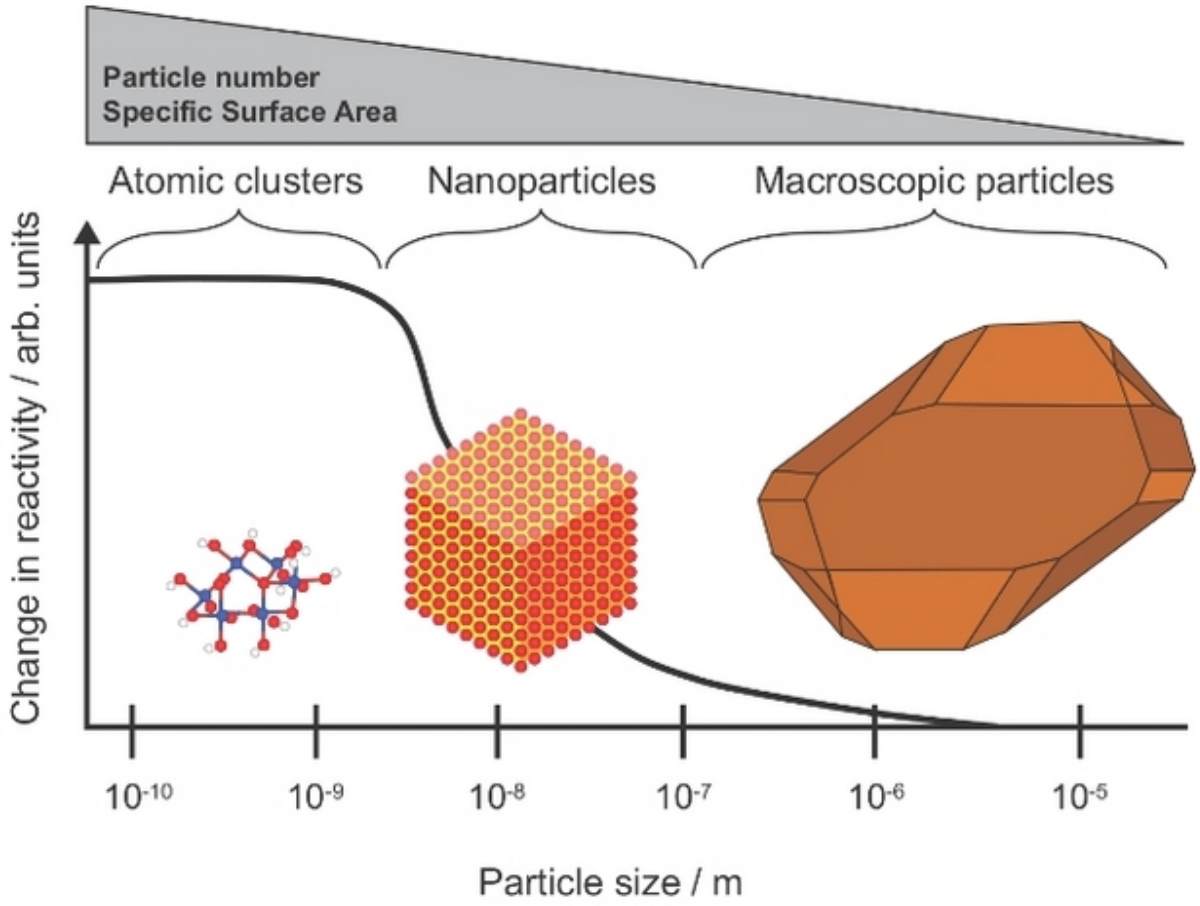

Figure 6. The surface-to-volume ratio of Nanoparticles.

The smaller a particle gets, the higher is the ratio between atoms at the surface and atoms found in the inner volume. If the mass of a given material is kept constant, the transition from the bulk material into nanoparticulate matter results in a vast increase of the surface-to-volume ratio and therefore also in reactivity.

(© 2013 Nature Education, adapted from [112])

might be useful to increase the storage capacity of magnetic data storage devices such as computer hard disks.[113] Here the number of magnetizable elements determines the storage capacity and might be vastly increased by the use of magnetic NPs.[111] NPs are however not solely a product of modern engineering technology, but can be generated through natural processes such as volcano eruptions or forest fires.[103] According to their mode of generation, NPs can be classified as either non-engineered or engineered.

1.4.2. Non-engineered Nanoparticles

Non-engineered NPs are generated by natural processes in the environment or by anthropogenic activities. One common feature of non-engineered NPs is that they are mostly heterogeneous in size and shape, since their generation is a result of random processes and not of defined physical or chemical reactions. Non-engineered NPs are abundant on earth and can also be found in extraterrestrial space.[103, 114, 115] The formation of terrestrial environmental NPs is well understood and can be accounted to various natural processes including weathering of minerals, photochemical reactions, microbial activity or the formation of crystals in super-saturated fluids.[115-117] Airborne environmental NPs are the result of dust storms, forest fires and volcanic eruptions.[118] There are also examples for the existence of extraterrestrial NPs that were found in dust collected from the moon, the mars and from interplanetary space itself.[103] Humans can also cause the unintentional generation of non-engineered NPs as a result of their undertakings such as material breakdown, combustion of fossil and non-fossil energy sources, welding and even cooking.[119-123] Most of the activities that lead to the unintended generation of non-engineered NPs can be accounted to the more recent history of men and it would be reasonable to argue that nowadays the majority of airborne NPs are anthropogenic due to the excessive use of fossil energy sources. Indeed, the primary source of airborne NPs in urban areas can be found in the exhaust from automobiles.[103] These exhaust NPs usually contain carbon and minerals and are of spherical shape.[124] However, the overall amount of aerosols that contain airborne NPs produced by humans only make up 10% of the world's total, while the remaining 90% are of natural origin.[125] Compared to anthropogenic non-engineered NPs, the non-anthropogenic ones exist in large quantities and there is increasing evidence that they play a crucial role in the terrestrial ecosystem.[112] In history, another class of NPs emerged as the result of human technological and scientific progress: engineered NPs.

1.4.3. Engineered Nanoparticles

Other than non-engineered NPs, engineered NPs are exclusively of anthropogenic origin and can be made of a broad variety of materials or material compositions. Engineered NPs are mainly characterized by their uniformity in size and shape and by a defined material composition and surface chemistry. All of these characteristics are tunable, thus allowing the creation of NPs with novel properties for specific applications.[126]

Figure 7. The Lycurgus cup in reflected and transmitted light.

The Lycurgus cup appears green in reflected light and ruby red in transmitted light, an effect that is attributed to NPs made of gold and silver that are embedded in the glass in defined quantities. This artifact thus represents an early artistic use of the unique optical effects that can occur for NPs.

(Department of Prehistory and Europe, The British Museum. Height: 16.5 cm, diameter: 13.2 cm. © The Trustees of the British Museum)

One of the earliest examples for the use of engineered NPs dates back to the 3rd century Roman Empire as demonstrated by the Lycurgus cup that is made of dichroic glass which appears green in reflected light and ruby red in transmitted light (**Figure 7**). This effect on the perceived color of the cup is attributed to NPs of about 70nm in size that were embedded in the glass and made of a gold and silver alloy.[127] Among others, this example illustrates how the unique physiochemical properties of NPs lead to their specific application in the past, even though the scientific basis for understanding these effects was founded much later in the last decades of the 20th century.[128, 129] Today, NPs are extensively investigated and already found their use in different consumer products such as textiles, food additives, cosmetics, antimicrobial agents and colorants in paint.[130] For example, one of the widespread applications of NPs encompasses the use of colloidal TiO in white paint or sunscreen.[131] Another modern day applications of engineered NPs can be found in biomedicine. Due to their controllable physiochemical properties, NPs have gained high interest for the use in targeted drug delivery, diagnostics and as cellular probes.[132-134]

While the size related features of engineered NPs open up new avenues in material science and medicine, they also enable them to interact with biological systems in a unique way that might lead to detrimental effects. The introduction of engineered NPs to a broad variety of applications is therefore accompanied by safety concerns.[103, 105, 135-138]

1.4.4. The possible risks of nanoparticles

Irrespective of their process of generation, NPs possess physiochemical properties that differ from the bulk form of a given material and might provoke toxic effects on living organisms.[139] However, the abundance of natural occurring environmental NPs suggest that biological systems were always exposed to NPs throughout evolution and might have developed mechanisms to counteract possible detrimental effects. Airborne NPs that originated from forest fires have entered the respiratory tracts of animals since they evolved lungs to breathe. Viruses themselves can be regarded as NPs consisting of biological building blocks like proteins and DNA and have challenged the immune systems of living organisms throughout their evolution, a process that is ongoing.[140-142] It is thus very likely that mechanisms that aim to degrade or excrete nano-sized foreign bodies have evolved in uni- and multicellular organisms including humans. Indeed, the efficacy of NPs in biomedical applications is often hampered by the many systems that either prevent the entry of NPs into the organism or facilitate their clearance.[143, 144] The human body has several barriers that effectively prevent NPs from entry. Healthy skin is thought to pose an effective barrier against the uptake of most NPs due to its multilayered anatomic structure and ability for continuous regeneration.[145] When ingested, the uptake of NPs through the gastrointestinal tract is blocked by several cell layer of the intestinal epithelium that effectively prevents large numbers of nano- or macromolecules from passaging into nearby blood vessels.[146, 147] In the lung, inhaled NPs are removed by mucocilliary transport when they enter the respiratory tract and by macrophages once they reached the alveoli.[148] Both mechanisms are very effective as long as they are not chronically overused. In case of severe chronic exposition of the lung, the amount of NPs that is able to reach the bloodstream only accounts to a very small fraction (< 0.05%) of the amount administered in total.[149] Once a nanoparticle enters the blood stream, it rapidly absorbs serum proteins including opsonins that mark them as foreign bodies for activation of the complement system.[150] Furthermore, opsonation induces phagocytosis by cells of the reticuendothelial system.[151] Another systemic defense

mechanism responsible for the clearance of NPs from the blood stream is the formation of neutrophil extracellular traps (NET-traps).[152, 153] Once NPs were able to enter the blood stream and circumvent systemic clearance mechanism they are, in contrast to larger micro-sized particles, able to cross biological barriers like the blood- brain barrier, the placental barrier and even cell membranes.[154, 155] A risk of nanoparticle usage is thus primarily given if biological barriers that are meant to prevent their systemic entry are circumvented or compromised. Another property of NPs that gives rise to serious concerns is their increased surface-to-volume ratio that accounts for an increase in physiochemical reactivity with components of biological system.[138] These reactions can include the rapid absorption of proteins on the NPs surface thereby promoting conformational changes that can cause inactivation or other protein modifications.[156] Furthermore, the formation of reactive oxygen species (ROS) through a Fenton-like reaction is reported for metallic NPs (MNPs). ROS can cause oxidative damage to proteins, membrane lipids and DNA and are therefore thought to be a major source for toxicity in metallic NPs.[157] The introduction of inorganic materials or material compositions in engineered NPs is also thought to pose an additional risk, since these can lead to physiochemical properties that challenge established mechanisms in multicellular organisms. For example, most QDs are restricted to be used for *in vitro* applications while their *in vivo* use is hampered by high toxicity that is mainly attributed to materials used for their synthesis such as the heavy metal cadmium.[158] In summary, factors that determine a NPs hazard potential for biological systems are diverse and include size, shape, material composition, surface chemistry and exposure scenario.[105, 159]

1.4.5. The challenge of nanotoxicology

The assessment of nanoparticle toxicity is hampered by different aspects all related to their unique features. Since the physiochemical properties of NPs determine their interaction with a given biological system, investigating and reporting these is crucial. It is well known that NPs can undergo physiochemical changes as a function of their environment and thus can acquire toxicity in the course of their application.[160, 161] When coated with polymers, NPs can change their size in response to the local pH due to osmotic swelling or shrinking. Changes in size can also be facilitated by the formation of a protein corona, a mechanisms that involves the rapid absorption of proteins as a function of its surface chemistry.[162] The protein composition of the corona also influences the NPs' surface charge which influences the rate

of internalization by cells. It is thus important to thoroughly characterize NPs not only in their solvent but also under conditions that are identical to later read-out experiments.[163] The toxicity assessment of NPs also requires the correct establishment of a dose-response relationship that needs appropriate dose metrics and a comprehensive dosimetry.[164] Usually the applied dose of NPs *in vitro* is given in volumetric units such as µg/ml, which is however not sufficient to describe the amount of NP that was actually applied. Even though a concentration is kept constant, the number of NP in solution can change with the total volume applied. Thus, units that describe the amount of NPs per area seem to be more suitable to describe the applied dose.[105] The dosimetry *in vitro* can be defined by the administered, delivered and cellular dose, which can be calculated by using mathematical models like the *In vitro* Sedimentation, Diffusion and Dosimetry model (ISDD).[165, 166] The administered dose describes the amount of NPs that is employed at the beginning of the experiment while the delivered dose gives information about the amount of NPs that reaches the cell monolayer after a given time. The cellular dose describes the amount of NP that is ultimately internalized by the cell and is therefore also termed the effective dose (**Figure 8**). Reporting the dosimetry not only allows the definition of a critical dose at which toxic effects appear it is also a prerequisite for proper reproducibility by other researchers. Another critical issue in NP toxicology is their ability to interact with colorimetric and fluorescence-based assay systems that are usually employed for the determination of cellular viability and proliferation.[167-169] These interactions can comprise absorption of assay components (e.g. chemicals, dyes or proteins) on the NPs surface and quenching or absorbance of fluorescence and transmitted light respectively.[170] It is thus important to investigate possible interferences of NPs with employed assay systems to prevent the production of false positives. When employing *in vitro* experiments it needs to be considered that the exposure of a homogenous cell monolayer to a given nanoparticle only poorly reflects the *in vivo* situation.[171] For example, nanoparticle toxicity can be mediated from one cell type to another through secreted chemokines as reported for two different co-culture models of lung alveolar cells.[172, 173] The *in vitro* toxicity assessment of NPs should thus be complemented by relevant co-culture models or *in vivo* experiments. Taking the NPs unique physiochemical properties and their implications into account by considering these aspects in the toxicity assessment of NPs is of paramount importance to prevent false results and to vastly improve the quality of the reported data. The thorough characterization of NPs characteristics and their impact on biological systems is essential in biomedical applications, where biological barriers are intentionally circumvented.

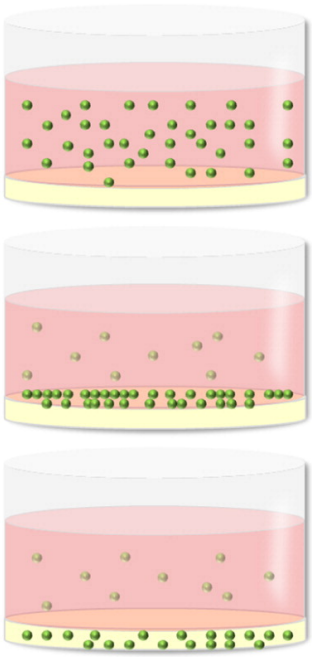

Administered Dose
Defined as the particle number, mass or surface area per volume suspension media

Delivered Dose
Defined as the particle number, mass or surface area to reach the cell monolayer (per cm^2) over the duration of an experiment

Cellular Dose
Defined as the particle number, mass or surface area to be internalized into the cell monolayer (per cm^2) over the duration of an experiment (this includes particles that are firmly associated with the cell surface)

Figure 8. Definitions for dose-metrics relevant in nanotoxicology.

(© Journal of Controlled Release [165])

1.5. Nanoparticles in diagnosis and treatment of musculoskeletal diseases

1.5.1. Superparamagnetic iron oxide nanoparticles

Superparamagnetic iron oxide NPs (SPIONs) are nanoscaled (5 - 15nm) crystals that consist of the biodegradable iron oxides magnetite (Fe_3O_4) or maghemite (γ-Fe_2O_3) or a mixture of both phases and exhibit magnetism only under the influence of an external magnetic field, a nano-size related effect termed superparamagnetism.[174] Superparamagnetism occurs when the ferromagnetic materials is reduced to a size smaller than 20 nm. Unlike larger magnets, SPIONs do not have multiple magnetic domains. Instead, they possess a single magnetic domain that acts as a single super spin with high magnetic susceptibility.[175] When an external magnetic field is applied, SPIONs provide a stronger and more rapid magnetic response compared with bulk magnets while the residual magnetization itself (remanence) and the field strength required to annul the SPIONs magnetism (coercivity) are negligible. Unlike bulk ferromagnetic materials, a SPION will therefore always return to its original magnetization spin [176, 177] In an alternating magnetic field, SPIONs absorb energy due to time-dependent magnetic viscosity (Néel relaxation) and become magnetized up to their saturation magnetization. After removal of the alternating magnetic field, heat is transferred to the surrounding environment as a result of the SPIONs energy loss. Depending on the frequency of the alternating magnetic field, this allows for the induction of hyperthermia which can be utilized for the treatment of cancer.[178] When used for biomedical applications *in vitro* or *in vivo*, the SPIONs physiochemical properties determine their colloidal stability, solubility, and biocompatibility. To improve these properties, SPIONs can be coated with either organic or inorganic substances. Coating the SPION also allows for surface functionalization (e.g. with chemicals or peptides) that vastly increases the range of diagnostic and therapeutic applications in biomedicine such as protein capture in biological fluids or targeted drug delivery.[133] Furthermore, the SPIONs superparamagnetism allows for their magnetic capturing from fluids or targeted attraction to a certain tissue or organ without the risk of later agglomeration, i.e. the SPIONs superparamagnetism allows them to remain well dispersed in solutions and do not form bigger agglomerates due to magnetic attraction that would compromise their use *in vivo* due to the blockage of blood capillaries.[175] Another method that makes use of the SPIONs' strong magnetic moments uses high frequent dynamic magnetic fields. Unlike static magnetic fields generated by large rare-earth magnets, dynamic fields grant deep tissue penetration and allow for precise control of the NPs movement.[179]

Among all the possible biomedical applications facilitated through the SPIONs' properties, their use as a contrast agent for MRI is based on the advantages of their single super spin.

1.5.2. Superparamagnetic iron oxide nanoparticles for contrast enhancement

SPIONs were introduced as an imaging agent for MRI several decades ago and have become a part of daily clinical routine use such as in imaging liver metastasis. Commercially available SPION formulations that are used as contrast agents in clinical MRI do usually consist of several iron oxide nano-crystals embedded in a polymer such as dextran and ranging in size from 20 – 100nm.[174] In MRI, strong magnetic fields are used to align the magnetization spin of hydrogen atoms (protons) in tissue bound water molecules. When switching back to their original magnetization alignment, the protons emit radio frequencies which can be detected by a receiver coil and used to generate the actual image. The contrast between different tissues is determined by the rate at which the protons return to their original magnetization state the so-called equilibrium. Each tissue returns to its equilibrium state by the independent processes of T1 (spin-lattice) and T2 (spin-spin) relaxation. When placed in an external magnetic field, SPIONs create very strong local magnetic field gradients and their superparamagnetism enhances the water proton spin dephasing, thereby shortening the T1 and T2 relaxation rates of the surrounding water.[180, 181] The SPIONs ratio of T1 to T2 relaxivity (R1/R2) determines its use as a positive or negative contrast agent. SPIONs with a diameter of more than 50nm have a low R1/R2 ratio and are used as negative contrast agents with T2 weighted imaging sequences. Smaller SPIONs with a diameter of around 20nm have a high R1/R2 ratio and can be used for both positive and negative contrast enhancement by applying T1 or T2 weighted imaging sequences. Apart from their effect on T1 and T2 relaxivities, SPIONs increase the T2* effect also termed susceptibility effect. The T2* relaxation is based on magnetization differences between different voxels in the MRI image that is caused by a non-homogenous distribution of SPIONs within the tissue. This creates local field gradients that accelerate the proton spin dephasing.[174] Therefore, SPIONs exhibit an excellent contrast enhancement on T1, T2 and T2* weighted sequences and are able to generate signal changes that are several magnitudes stronger compared to other contrast agents such as the T2 weighted Gadolinium.[182] Their ability to generate contrast enhancement in a certain organ or tissue of interest is based on their bio-distribution that varies for different SPION formulations. The SPIONs accumulation rate and retention time is a function of their physiochemical properties and can vary between different organs but also

between healthy and diseased tissue due to macrophage infiltration and vascularization. Varying the SPIONs physiochemical properties therefore allows targeting and subsequent imaging of certain organs or tissues of interest.[183] For example, 100nm sized dextran-coated SPIONs (Ferumoxides) are phagocytized by Kupffer cells and thus accumulate to large extends (~80%) in liver, allowing imaging of liver metastasis.[184] SPIONs with a smaller diameter of 35nm (Ferumoxtran) or an anionic surface charge (Ferumoxytol) are reported to have less affinity to Kupffer cells and consequently a longer blood half-life. This leads to an increased SPION accumulation in the lymph nodes or bone marrow, which can be utilized for imaging metastatic lymph nodes or non-Hodgkin lymphomas respectively.[185-187] Recent studies suggest that the accumulation of SPIONs in bone marrow could be also utilized for visualization of bone turnover and targeted drug delivery.[188-190] Due to their colloidal behavior i.e. their good dispersion in fluids and their excellent properties as a contrast agent, SPIONs were proposed to be used as probes for direct labeling of cells *in vitro* and their subsequent MRI visualization after transplantation *in vivo*.[191, 192]

1.5.3. Superparamagnetic iron oxide nanoparticles for cell labeling

The development of effective MSC based therapies requires non-invasive visualization of the cellular graft which can be achieved by using SPIONs as labeling probes.[81] Most previous studies on visualization of MSCs used commercially available dextran- or carboxydextran-coated SPIONs (Endorem/Feridex or Resovist, respectively).[193-198] However, manufacturing of both products was discontinued in 2008 and 2009, which prevents their future applications. But more importantly, these NPs were originally developed to be taken up by phagocytic cells from the reticuloendothelial system (e.g. monocytes, macrophages and osteoclasts) but not by non-phagocytic cells such as MSCs.[199] To overcome this limitation, transfection agents (TA) were used.[191] However, some TAs are reported to be toxic under certain circumstances and their influence on MSCs biology is an issue of debate.[196, 200-202] In addition, the colloidal stability of dextran- or carboxydextran-coated SPIONs is impaired in cell culture media, hampering the effectiveness of *in vitro* labeling.[203] Furthermore, the dextran-coating itself raises problems as it is susceptible to lysosomal degradation, resulting in exposure of cellular compartments and the cytosol to uncoated iron oxide NPs and ferrous ions to which observed cytotoxic effects were accounted. Uncoated SPIONs that consist of magnetite can contribute to the intracellular production of ROS, since it is not very stable and can readily undergo oxidation to form maghemite in the presence of

air, light and moisture.[203, 204] The release of high amounts of ROS as a result of Fenton-like reactions is believed to be a major contributor to the cytotoxicity of metallic nanoparticles in general.[157] In recent years, several studies focused on the development of novel SPION-coatings for MSC-labeling that meet the physiochemical need for efficient cellular uptake by MSCs *in vitro* without provoking toxicity.[204-209]

1.5.4. Amino-Polyvinyl alcohol superparamganetic iron oxide nanoparticles

Polyvinyl alcohol (PVA) is an organic polymer that can be used for the coating of SPIONs and allows for further surface functionalization.[210] The excellent biocompatibility and the clearing mechanisms of PVA are well investigated.[211] A major advantage of PVA is the fact that it is safe to use in humans as it has been in medical use for several years, such as for cartilage replacements, wound packing and contact lenses.[212] PVA cannot be enzymatically degraded within the human body but can be excreted via urine. Thus, when used as a SPION coating, PVA is more likely to effectively protect the iron oxide crystal from degradation than dextran. PVA can also be functionalized with chemical groups to manipulate the SPIONs physiochemical properties. For example, the addition of amine groups promotes internalization by non-phagocytic cells without the need for compromising TAs.[213-215] Amino-PVA-SPIONs (A-PVA-SPIONs) are already well characterized for their physiochemical and magnetic properties.[216] In contrast to dextran- or carboxydextran-SPIONs, they exhibit excellent colloidal stability and dispersion in different cell culture media *in vitro* even in the presence of fetal calf serum (FCS).[217] Engineered A-PVA-SPIONs were originally developed as a platform for diagnosis and treatment of rheumatoid diseases without exhibiting detrimental effects. For this, the A-PVA-SPIONs crystallite core is made of maghemite only. In consequence, the absence of magnetite prevents the occurrence of unwanted Fenton reactions as a result of the particles' dissolution that would eventually produce ROS. In addition, the non-degradable A-PVA coating is well suited to shield the iron oxide cores off from acidic lysosomal degradation. Due to the advantageous properties of the coating and the iron oxide crystal itself, the engineered A-PVA-SPIONs potential for exhibiting toxicity is considerably low. A-PVA-SPIONs might be used as a contrast enhancement agent and for MSC labeling. However, the feasibility of their application has yet to be explored; especially their impact on MSCs viability and function remains unknown.

1.5.5. Metallic nanoparticles from hip implants: a non-engineered clinical problem

Since early implant failure still occurred for MoM implants, closer analysis of the MoM wear revealed that the majority of the generated metal debris is in the nanoscale with $6.7x10^{12}$-$2.5x10^{14}$ particles generated per year. This means that although the total particle volume is less, up to 500 times more particles are generated from MoM implant wear when compared to MoP endoprostheses.[102] It is now widely accepted that not only the amount of wear debris but also the material composition and particle size determine the exact mechanism of the local tissue reaction.[218] Apart from ions, MoM wear contains MNPs that are irregular in size and shape, do consist of the bulk alloy's metals in various oxidation states and can be therefore categorized as non-engineered NPs.[102, 219-222] The heterogeneity of their physiochemical properties and the lack of any coating substance are very likely to cause adverse effects on a cellular level. The primary response to all wear debris in general involves the formation of a synovial-like membrane around the implant that consist of highly vascularized fibrotic and connective tissue. This periprosthetic membrane contains vast amounts of wear debris derived from the implant and is characterized by the infiltration of macrophages and dendritic cells.[223] In addition, metallic wear generated by MoM implants provokes the infiltration by T and B cells in combination with plasma cells.[218] Furthermore, metallic wear is reported to induce the formation of cystic masses termed pseudotumors and can also be the cause of local allergic reactions mediated by T-lymphocytes.[224, 225] It is reported that the phagocytosis of small wear debris and nanoscaled particles (< 10µm) by osteoclasts, macrophages and dendritic cells leads to a release of cytokines and chemokines and results in the recruitment of more immune cells thereby further aggravating the inflammatory response. Additionally, under these conditions, macrophages, dendritic cells and monocytes differentiate into osteoclasts and already existing osteoclasts are activated.[226] MoM wear thus triggers an aseptic inflammation in the periprosthetic region that leads to an increase in osteoclast number and activity, thereby increasing the rate of bone resorption. However, little is known about the effect of MoM wear on the bone forming osteoprogenitor cells such as MSCs. So far, only one published study has investigated the effect of nanoscaled cobalt-chrome (CoCr) particles on MSCs, together with three different types of wear particles relevant in orthopaedics.[227] Here, the exposure to CoCr particles resulted in a decrease in proliferation and ALP activity accompanied by an up-regulation in the expression of the inflammatory cytokines IL-1β, IL-6 and TNFα. However, an effect on the MSCs differentiation capacity especially into the osteogenic lineage was not investigated.

1.6. Project aims

Within the musculoskeletal system, the hip joint facilitates bipedal locomotion by connecting the pelvis with the lower extremities and by supporting the body's weight. Pathologies of the hip joint can lead to severe disability and immobility. Modern cell therapies try to implement the regenerative potential of MSCs for the repair of cartilage and bone in diseased joints. Successful clinical translation of such therapies is not established yet and requires precise information about the grafted MSCs' spatial and temporal distribution. Cell labeling can help to monitor the MSCs fate by the use of SPIONs. In bone pathologies, SPIONs might be useful for diagnosis and treatment which requires their accumulation in bone marrow without exhibiting detrimental effects on local cells such as MSCs. However, these applications of MSCs and/or SPIONs are still not translated into clinical routine. The most widespread treatment of hip joint pathologies is THA, where the joints articulating surfaces are replaced by implants. The outcome of THA can be compromised by implant loosening in response to wear of its articulating surfaces. In MoM implants, MNPs are generated that accumulate in the periprosthetic region thereby exposing local MSCs. The presence of MNPs within wear was described two decades ago which is relatively recent, given the use of MoM implants in THA since the 1960s. Yet, little is known about the effect of MoM wear MNPs on local MSCs. This study's aim is to evaluate the impact of engineered A-PVA-SPIONs and non-engineered MoM wear MNPs on MSCs. Regarding A-PVA-SPIONs, the particular aims are (1) to develop an efficient A-PVA-SPION-labeling procedure for MSCs based on particle internalization, (2) to analyze the influence of *in vitro* exposure with A-PVA-SPIONs on MSC viability, multilineage differentiation as well as migration and (3) to provide proof of principle for visualization of A-PVA-SPION-labeled MSCs in MRI. It is hypothesized that A-PVA-SPIONs are suitable to label MSCs without provoking cytotoxicity thus allowing for cell visualization in MRI. Additional aims are (4) to verify the accumulation of A-PVA-SPIONs in bone marrow in an animal model and to (5) investigate the influence of *in vivo* A-PVA-SPION exposure to local MSCs' viability and key functions. This study's second hypothesis is that systemically administered A-PVA-SPIONs will accumulate in bone marrow without provoking toxicity to local MSCs. The aims regarding MoM wear MNPs are (6) to verify the presence of MoM wear in the surrounding periprosthetic compartments and (7) to investigate if the *in vivo* exposure to MoM wear influences the viability and function of MSCs. The third and final hypothesis of this thesis work is that the exposure to MoM wear MNPs negatively influences the MSCs osteogenic function thereby contributing to osteolyis.

2. Materials and Methods

2.1. List of chemicals and consumables

Reagent/Consumable	Company	Experiment
AlamarBlue® Cell Viability Reagent	Life Technologies, Carlsbad, CA, United states	Assay Interference, cell viability
Alizarin Red S	Merck, Darmstadt, Germany	MSC differentiation
A-PVA (2 wt %; M12)	Erkol	SPION synthesis
Ascorbic acid	Sigma-Aldrich, St. Louis, MI, United states	MSC differentiation
Blue Alkaline Phosphatase Substrate KIT III	Vector® Labs, Burlingame, CA, US	CFU Assay
Bovine serum albumin	Sigma-Aldrich, St. Louis, MI, United states	MSC differentiation
CellTiter 96® AQueous One Solution Cell Proliferation Assay	Promega; Madison, WI, United states	Assay Interference
Cetylpyridinium chloride	Sigma-Aldrich, St. Louis, MI, United states	MSC differentiation
CyquantNF® assay kit	Life Technologies, Carlsbad, CA, United states	Assay Interference, cell viability
CytoTox-ONE™ Homogeneous Membrane Integrity Assay	Promega; Madison, WI, United states	Cell viability
Dexamethasone	Sigma-Aldrich, St. Louis, MI, United states	MSC differentiation
Dulbecco's Modified Eagle Medium; Low Glucose	Gibco, Grand Island, NY, United states	Cell culture
FeCl3	Merck, Darmstadt, Germany	Iron quantification
Foetal calf serum	Biochrom AG, Berlin, Germany	Cell culture
FluoromountG	SouthernBiotec, AL, United States	Migration rMSCs
Formaldehyde 4%	Roth, Karlsruhe, Germany	MSC differentiation, MRI phantoms
Gelatine	Sigma-Aldrich, St. Louis, MI, United states	MRI phantoms
HCl	Merck, Darmstadt, Germany	Iron quantification

Reagent/Consumable	Company	Experiment
HZB-2 gold grid	Gilder Grids, Grantham, UK	Transmission X-Ray microscopy
Indomethacin	Sigma-Aldrich, St. Louis, MI, United states	MSC differentiation
Insulin	Sigma-Aldrich, St. Louis, MI, United states	MSC differentiation
Insulin-transferrin-sodium selenite media supplement	Sigma-Aldrich, St. Louis, MI, United states	MSC differentiation
Isobutyl-methyl-xanthin	Sigma-Aldrich, St. Louis, MI, United states	MSC differentiation
Isopropanol 100%	Merck, Darmstadt, Germany	MSC differentiation
KBr	Fluka Chemika	SPION characterisation
L-alanyl-L-glutamine	Gibco, Grand Island, NY, United states	Cell culture
MACS® separation buffer	Milteny Biotec GmbH, Bergisch Gladbach, Germany	Iron load in bone marrow
Mitomycin C	Sigma-Aldrich, St. Louis, MI, United states	Migration hMSCs
Nuclear fast red	Carl Roth, Karlsruhe, Germany	CFU Assay
Oil Red	Merck, Darmstadt, Germany	MSC differentiation
Papain	Sigma-Aldrich, St. Louis, MI, United states	MoM wear particle isolation
Penicillin/Streptomycin	Biochrom AG, Berlin, Germany	Cell culture
Phosphate buffered saline	Gibco, Grand Island, NY, United states	Various
Polycarbonate transwell inserts (8 µm pore size)	Nunc, Wiesbaden, Germany	Migration rMSCs
Potassium ferrocyanide (K4[Fe(CN)6])	Merck, Darmstadt, Germany	Iron quantification
PrestoBlue® Cell Viability Reagent	Life Technologies, Carlsbad, CA, United states	Cell viability
Proline	Sigma-Aldrich, St. Louis, MI, United states	MSC differentiation
Protamine ME	MEDA, Bad Homburg, Germany	SPION internalisation

Reagent/Consumable	Company	Experiment
Proteinase K	Sigma-Aldrich, St. Louis, MI, United states	MoM wear particle isolation
Hoechst33342	Life Technologies, Carlsbad, CA, United States	Migration rMSCs
PVA-OH (10 wt%; Mowiol 3-85)	Kuraray Europe GmbH	SPION synthesis
Pyruvate	Sigma-Aldrich, St. Louis, MI, United states	MSC differentiation
recombinant human TGF-β1	Peprotech, Rocky Hill, NJ, United states	MSC differentiation
ß-glycerol phosphate	Calbiochem, San Diego, CA, United states	MSC differentiation
Culture inserts for self-insertion	IBIDI, Munich, Germany	Migration hMSCs
MACS® MS columns	Milteny Biotec GmbH, Bergisch Gladbach, Germany	Iron load in bone marrow
Histopaque 1077	Sigma-Aldrich, St. Louis, MI, United states	Cell isolation hMSCs
C-Chip improved Neubauer	Peqlab, Erlangen, Germany	Cell Culture
RNeasy® Mini Kit	Quiagen, Venlo, Netherlands	RNA expression
First Strand cDNA Synthesis Kit	Quiagen, Venlo, Netherlands	RNA expression
RT² SYBR Green qPCR Mastermix	Quiagen, Venlo, Netherlands	RNA expression
RT² Profiler PCR Array human cell motility	Quiagen, Venlo, Netherlands	RNA expression

2.2. List of technical equipment

Device	Company	Experiment
Transmission Electron Microscopy CM12	FEI Co. Philips Electron Optics, Zürich, Switzerland	SPION characterisation
Photon Correlation Spectroscopy apparatus ZetaPals	Brookhaven: Laborchemie GES.M.B.H., Vienna, Austria	SPION characterisation
Spectroscope Nicolet 6700	ThermoScientific, Waltham, MA, USA	SPION characterisation
Magnetom® Trio 3T	Siemens, Munich, Germany	Visualisation of A-PVA-SPION accumulation *in vivo*
Plunge freezer	Custom made	Transmission X-Ray microscopy
CasyTT cell counter	Schärfe Systems, Reutlingen, Germany	Cell Culture
Multimode microplate reader m200 pro	Tecan Group AG, Maennedorf, Switzerland	Cell viability, MSC Differentiation, iron quantification
Inverted microscope DMI6000B	Leica Microsystems, Wetzlar, Germany	Cell migration
1.5T MRI scanner	Siemens, Munich, Germany	Visualisation of labeled hMSCs *in vi*vo and *in vitro*
Elmasonic S 10 sonicator	Elma Schmidbauer GmbH	MoM wear particle isolation
GentleMACS Dissociater	Milteny Biotec GmbH, Bergisch Gladbach, Germany	MoM wear particle isolation
Ultracut S microtome	Leica Microsystems, Wetzlar, Germany	TEM analysis of MoM wear particles and A-PVA-SPION internalisation
Transmission electron microscope EM 906	Zeiss, Oberkochen, Germany	TEM analysis of MoM wear particles and A-PVA-SPION internalisation
Thermal Cycler iQ 5 RTPCR qPCR	BioRad Laboratories Inc., Hercules, CA, United States	RNA expression

2.3. Amino-polyvinyl alcohol superparamagnetic iron oxide nanoparticles

2.3.1. Synthesis

A-PVA-SPIONs were synthesized by Lionel Maurizi, Marie-Gabrielle Beuzellin and Heinrich Hofmann at the École polytechnique fédérale de Lausanne (EPFL) following a co-precipitation protocol.[210, 228] Briefly, 0.064 moles of iron II from $FeCl_2$ and 0.128 moles of iron III from $FeCl_3$ were solved in 1.5 L deionized (DI) water and mixed with 120 mL of an NH_4OH solution (25%). After 10 min the suspension was sedimented under a magnetic field and washed with DI water until pH 7. SPIONs were redispersed in 400 mL and oxidized with 160 mL HNO_3 (2M) and 240 mL $Fe(NO_3)_3$ (0.35M) under reflux for 1.5h to achieve maghemite (γ-Fe_2O_3). The suspension was washed again with DI water and was dialyzed (with MWCO 12-14 kDa cellulose membrane dialysis tubing) against HNO_3 (10mM) for 3 days by changing the solution every 12h. The suspension was finally centrifuged at 30000 g for 15 min and the supernatant was kept. The final suspension of SPION had a concentration of 10 mg_{Fe}/mL and a pH of approximately 2. Surface modification of the SPION with PVA was done following a protocol described previously.[210, 213, 229] PVA-OH (10 wt%; Mowiol 3-85, Kuraray Europe GmbH) and A-PVA (2 wt %; M12, Erkol.) solutions were prepared by dissolving dry PVA in ultrapure DI water and the solutions were rapidly heated for 1 hour at 90°C, cooled down, filtered at 0.45 μm with a PTFE filter syringe and stored at 4°C. 10 volumes of naked SPION were mixed with 9 volumes of PVA-OH solution (100 mg PVA OH/mL) and 1 volume of A-PVA solution (20 mg A-PVA/mL). The final A-PVA-SPION suspension (5 mg_{Fe}/mL, pH 3) was stored at least 1 week at 4°C before further use.

2.3.2. Characterization

A-PVA-SPIONs were characterized at the EPFL by Lionel Maurizi and the presented characterization data was already published.[230] Crystallite's size was measured by counting of 400 crystallites sizes on Transmission Electron Microscopy (TEM CM12; FEI Co. Philips Electron Optics, Zürich, Switzerland) pictures. Hydrodynamic diameters and Zeta potential of A-PVA-SPIONs were measured on a Photon Correlation Spectroscopy apparatus (PCS ZetaPals from Brookhaven: Laborchemie GES.M.B.H., Vienna, Austria). Fourier Transformation Infrared spectroscopy (FTIR) spectra were obtained using transmittance spectroscopy method from 400 to 4000 cm-1 at a resolution of 4 cm 1 and with acquisition of 32 scans. FTIR measurements were done on a spectroscope (Nicolet 6700, ThermoScientific, Waltham, MA, United States) using OMNIC software 8.1.11 firmware version 2.10. 2 mg of

dry samples (naked SPIONs and A-PVA-SPIONs) were mixed with 100 mg of dry Potassium Bromide (KBr from Fluka Chemika) to make a pellet under 10 tons pressure. The Transmittance (in arbitrary units: a.u.) were plotted versus the wavenumber in cm-1 with the preliminary subtraction of KBr background.

Since the physiochemical properties of polymer coated SPIONs can change in response to pH and protein concentration, the size and surface charge of A-PVA-SPIONs were characterized not only in their solvent (HNO_3 10mM, pH 2) but also in cell culture media (physiological pH 7.4) with and without fetal calf serum (FCS) supplementation. The iron oxide crystal mean diameter was 7.2 ± 2.5 nm (**Figure 9**). The SPIONs hydrodynamic diameter measures 14 ± 2 nm for the uncoated and 25 ± 3 nm for the A-PVA-coated SPION in its solvent HNO_3 (10mM, pH2). To confirm successful coating with A-PVA, uncoated SPIONs and A-PVA-SPION suspension were investigated by Fourier Transformation Infrared spectroscopy (FTIR) (**Figure 10**). Both FTIR spectra show the characteristic vibration band of γ-Fe_2O_3 (ν_{Fe2O3}) between 500 to 700 cm^{-1} proving the presence of SPIONs in the two samples.[231] On the spectrum of A-PVA-SPIONs only, the vibration of alkane groups (ν_{CH}) appears on a stretch peak around 2900 cm^{-1} close to the vibration peak of alcohol groups (ν_{OH}) between 3200 and 3500 cm^{-1} proving the presence of A-PVA on A-PVA-SPIONs.[232] Finally, the stretch vibration peak of carbonyl group at 1720-1740 cm^{-1} ($\nu_{C=O}$) was verified, proving the presence of aldehyde groups on A-PVA.[232, 233]

The Zeta potential of the uncoated SPIONs is at 26 ± 2 mV and slightly decreases to 20 ± 2 mV when the A-PVA-coating is added. When transferred into FCS-free DMEM, the A-PVA-SPIONs hydrodynamic diameter increases to 42 ± 2 nm, in the presence of FCS to 45 ± 2 nm. The addition of FCS to the cell culture media results in a negative shift in the Zeta potential of A-PVA-SPIONs from 21 ± 5 mV to -25 ± 5 mV (summarized in **Table 3**). Both, the increased hydrodynamic diameter and the negative zeta potential confirm the adsorption of serum proteins.[161] The determined size of 45 ± 2 nm will be the basis for calculating the A-PVA-SPIONs colloidal behavior that is needed for establishing an *in vitro* dosimetry (details see **Table 4**).

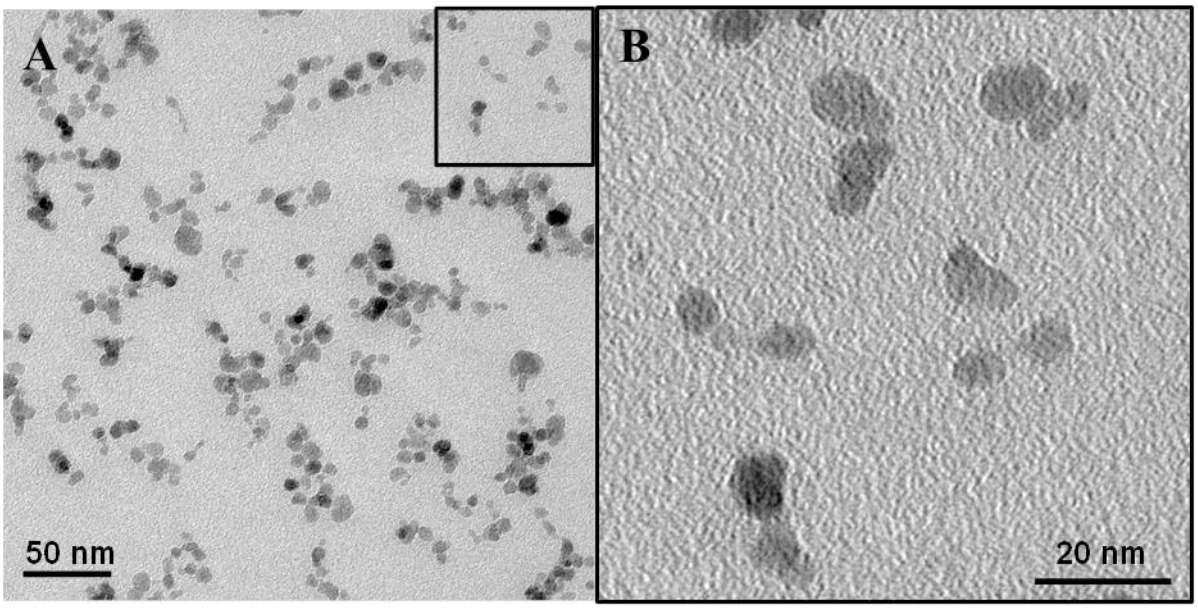

Figure 9. TEM pictures of A-PVA-SPIONs.

(A+B) TEM micrographs show iron oxide cores from A-PVA-SPIONs and were used to determine the mean average size of the ɣ Fe_2O_3 crystals. (© Small [230])

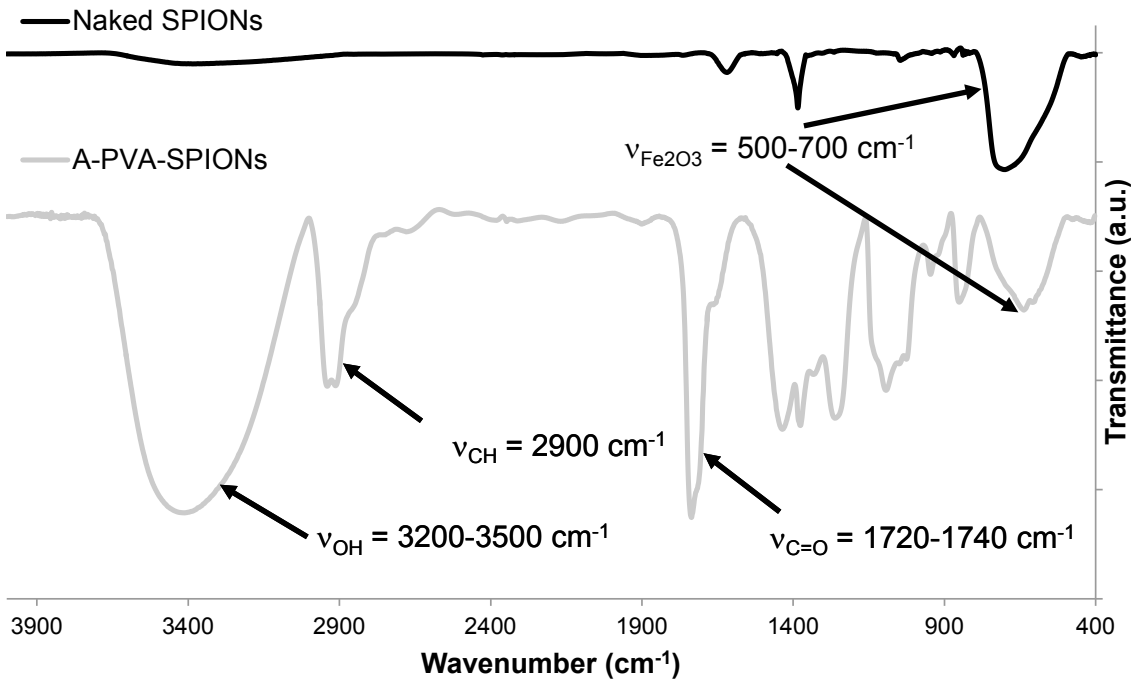

Figure 10. Fourier Transformation Infrared Spectra of uncoated and A-PVA coated SPIONs.

Naked SPIONs (black line) and A-PVA coated SPIONs (grey line). (© Small [230])

Table 3. Physiochemical properties of A-PVA-SPIONs (taken from [230]).

Particles	Medium	Concentration (mg_{Fe}/mL)	ɣ Fe_2O_3 crystal (nm)	Hydrodynamic diameter (nm)	Zeta potential (mV)	PVA/Fe ratio (mg_{PVA}/mg_{Fe})
SPION	HNO_3 10mM	10	7.2 ± 2.5	14 ± 2	+26 ± 2	0
PVA-SPION	HNO_3 10mM	5	7.2 ± 2.5	25 ± 3	+20 ± 2	9
PVA-SPION	DMEM	5	7.2 ± 2.5	42 ± 2	+21 ± 5	9
PVA-SPION	DMEM+FCS	5	7.2 ± 2.5	45 ± 2	-25 ± 5	9

2.3.3. Assay Interference

The CellTiter 96® Aqueous One Solution Cell Proliferation Assay (Promega; Madison, WI, United states; MTS based; determining mitochondrial reduction activity, i.e. viability), the CyquantNF® assay kit (Life Technologies, Carlsbad, CA, United states; determining total amount of DNA) and Alamar Blue (Life Technologies, Carlsbad, CA, United states; Resazurin based; determining mitochondrial reduction activity, i.e. viability; allowing repetitive measurements) were used according to manufacturer's protocol in the presence of different concentrations of A-PVA-SPIONs without and with confluent cells.

2.4. Metal-on-Metal wear

2.4.1. Sample acquisition

This part of the study was approved by the local ethical committee (EA1/194/13); all donors gave written informed consent. Degenerative osteoarthritis of the hip joint was the indication for primary THA in all control patients. MoM-patient samples were collected from patients with underlying indication for MoM implant revision and manifested aseptic periprosthetic osteolysis. For the isolation of control MSCs, bone marrow was harvested from patients that undergo a primary THA. MoM-patients and their respective controls were age and sex matched. Patients undergoing implant revision with indications other than aseptic periprosthetic osteolysis were excluded. Preexisting infectious diseases (e.g. HIV, hepatitis etc.) led to exclusion from this study. Bone marrow and periprosthetic tissue samples were collected during revision surgery of MoM-patients. Heparin blood plasma sampling was conducted 24 hours pre-operative for both groups. All samples were kept at 4°C and processed within 2 - 4 hours after harvest. Periprosthetic tissue samples were weighted and kept at -80°C until further processing. Bone marrow samples were used for subsequent cell isolation (for further information see section 2.5.1).

2.4.2. Particle isolation from periprosthtetic tissue

Isolation of metallic wear debris from periprosthetic tissue was performed using a two-step enzymatic digestion protocol as described previously with minor modifications in the tissue homogenization procedure.[220] In brief, 500 mg periprosthetic tissue were washed four times with 1 ml 250mM phosphate buffer (PB) supplemented 25mM ethylenediaminetetraacetic acid (EDTA, pH 7.6). For tissue homogenization, sample was transferred into a GentleMACS M-tube (Miltenyi Biotec) followed by the addition of 1.5 ml phosphate buffer. For sample homogenization, a GentleMACS Dissociater (Miltenyi Biotec) was used, running the manufacturer's program for lung tissue. The washing steps with different solutions were always performed as follows: the homogenized sample was centrifuged at 16.000x g for 10min., supernatant was discarded and washing solution was added followed by vigorously agitation of sample using a vortex. Homogenized sample was washed 1x with 1ml sodium dodecyl sulfate (SDS, 2.5%), 1x 1ml 80% acetone and 2x with 1ml PB. Supernatant in last washing step was not discarded. Sample was then vigorously agitated using a vortex and sonicated (Elmasonic S 10, Elma Schmidbauer GmbH) for 60s. Sample was then centrifuged at 16.000x g for 10min., supernatant was discarded and 1.5U

papain in 1.5ml PB were added followed by incubation at 65°C for 24h. Sample was then washed 1x with 2.5% SDS and incubated at 95°C for 10min. Sample was chilled at RT and washed 2x with 1ml 50mM Tris(hydroxymethyl)-aminomethan-HCl (Tris-HCL). Supernatant in last washing step was not discarded. Sample was then vigorously agitated using a vortex and sonicated (Elmasonic S 10, Elma Schmidbauer GmbH) for 60s. Sample was then centrifuged at 16.000x g for 10min., supernatant was discarded and 2mg ProteinaseK in 1ml 50mM Tris-HCl were added followed by incubation at 55°C for 24h. All following centrifugation steps were performed for 15min. Sample was then washed 1x with 1ml 2.5% SDS and incubated at 95°C for 10min. Sample was chilled at RT and then washed 1x with 1ml Tris-HCl (50mM), 1x with 0.5ml 80% acetone (+3% SDS) and 1x with ultrapure water (Braun Melsung AG). Sample was centrifuges at 16.000x g for 15min., supernatant was discarded and 1ml 100% ethanol was added. Isolated wear debris was kept at 4°C until further use.

2.4.3. Particle size and shape characterization

The mean particle size was determined by measuring the diameter of n=69 individual particles from three representative TEM micrographs using ImageJ Software.[234] The ratio of length to width (r) rate gave information about the particles shape. Particles were classified as round if $1 \leq r < 1.5$, oval if $1.5 \leq r < 2.5$ and needle-shaped if $r \geq 2.5$.[102]

2.5. Imaging

2.5.1. Transmission electron microscopy

For transmission electron microscopy (TEM) of A-PVA-SPION labeled MSC (labeling was performed as described in section 2.5.4), $5x10^5$ cells were trypsinized. The specimens were then post-fixed for 2 h in 2 % osmium tetroxide at room temperature, followed by dehydration in a graded series of ethanol. Fixed cells were spun down for pellet formation. Samples were immersed with propylene oxide as an intermedium, with a mixture of propylene oxide and epoxy resin, with pure epoxy resin and finally polymerized at 60 °C. Ultra-thin sections (70 nm) were prepared with an ultra-microtome (Ultracut S, Leica Microsystems, Wetzlar, Germany) and mounted on electron microscopy copper grids, 300 mesh. Sections were stained with uranyl acetate and lead citrate and investigated in the transmission electron microscope EM 906 (Zeiss, Oberkochen, Germany). The mean vesicle size was determined by measuring the diameter of n=4 vesicles from one representative TEM micrograph using ImageJ Software.[234]

For investigations on the MoM wear particles size and shape, the samples were immersed with propylene oxide as an intermedium, with a mixture of propylene oxide and epoxy resin, with pure epoxy resin and finally polymerized at 60 °C. Ultra-thin sections (70 nm) were prepared with an ultra-microtome (Ultracut S, Leica Microsystems, Wetzlar, Germany) and mounted on electron microscopy copper grids (300 mesh). Sections were investigated using a transmission electron microscope EM 906 (Zeiss, Oberkochen, Germany).

2.5.2. Transmission X-Ray microscopy

For transmission X-Ray microscopy (TXM), MSCs were cultivated for 24 h on gold grids (type HZB-2, Gilder Grids, Grantham, UK) coated with a perforated carbon film (Quantifoil Micro Tools GmbH, Jena, Germany) prior to A-PVA-SPION-labeling. Samples were then plunge frozen in liquid ethane and transferred into liquid nitrogen. Data acquisition using the Helmholtz-Zentrum Berlin (HZB) TXM at the undulator beamline U41-FSGM, electron storage ring BESSY II, Berlin, was performed as described elsewhere.[235] For imaging, a zone plate objective with 25 nm outermost zone width was used. The tilt range of the sample was from -60° to +60°. Tomographic reconstruction of the acquired Tilt series and 3D remodeling of the volumetric data were achieved by using eTomo software and CTvox (CTvox 2.6, Bruker CT, Kontich, Belgium), respectively. The mean diameter of vesicles and high contrast spheres was determined from seven representative images of the tomograms z-

stack using ImageJ Software (vesicles measured: n=9; high contrast spheres measured: n=80).[234]

2.5.3. Magnetic resonance imaging

All MRI investigations were performed by Azza Gramoun (animal handling) and Lindsey Crowe (MRI) at the University of Geneva (UniGen).[230, 236]

MRI-phantoms of A-PVA-SPION labeled hMSCs were performed by the author as followed: hMSC labeling was performed as described in section 2.5.4. A-PVA-SPION-labeled (100µg_{Fe}/ml) hMSCs were trypsinized, counted, and fixed in 4% formaldehyde (Roth, Karlsruhe, Germany). Fixed cells were spun down and ascending cell concentrations were embedded in 200µl 3% (w/v) gelatin on a 48-well plate. The cell phantoms were scanned by Lindsey Crowe at the University of Geneva (UniGen) using the same sequences as optimized for *in vivo* imaging and a 15cm surface for homogeneous signal response.[230] The experiment was carried out on 1.5T scanner. Longer scan times (10 signal averages) were needed to regain the SNR lost going to a larger coil and lower field. The MR imaging parameters for the phantoms are as followed: A 'T2-weighted' 2D acquisition with TR/TE/TI 8640/44/160ms, Flip angle 160°, Resolution 0.26 mm, FOV 200*100 mm and slice thickness 1mm. The 'T1-weighted' gradient echo is a 3D acquisition with resolution of 0.35mm and slice thickness 0.2mm,TR/TE 22/9.5ms, Flip angle 10° and FOV 160*80mm.

For *in vivo* visualization of labeled cells, the A-PVA-SPION-labeled MSCs and the non-labeled MSCs were injected intra-articularly into the right and left naïve knee joints of Lewis rats (Janvier Labs, Cedex, France) respectively. The following day, MR imaging of rat knee joints in vivo was conducted using a Siemens Magnetom® Trio 3T clinical scanner. A standard 4cm loop coil and respiratory monitoring with a pressure pad were used during the imaging session. The imaging protocol begins with a standard low-resolution localization sequence and the isotropic resolution 3D Ultra-short Echo time (UTE) double echo MR sequence fixed orthogonal and at the magnet centre. This was subsequently used to localize the correct plane for the 2D or thinner slab 3D images as well as for quantitative analysis. The protocol parameters of the sequences used were as follows: 3D T1 gradient echo was used to detect and visualize A-PVA-SPIONs by signal loss. Parameters: TR/TE 14.3/5.9ms, flip angle 12°, fat suppression, isotropic resolution 0.31mm, and FOV 100mm, acquisition time 4 minutes 54 seconds. Difference Ultra-short Echo time (dUTE) imaging was used for A-PVA-SPION positive contrast detection and quantification. Parameters: 3D isotropic matrix 448

and 80mm FOV, giving 180 μm in all three dimensions, 50000 radial projections, UTE/TE(2) 0.07ms/2.46ms (for in-phase fat/water image), TR 9.6ms (in vivo 100 segments), flip angle 10° , acquisition time 16 minutes 54 seconds.

Images were acquired on a Siemens Magnetom® Trio 3T clinical scanner with the system 4cm loop coil (Siemens Medical AG, Erlangen, Germany). Respiratory monitoring used a pressure pad (Small Animal Inc., Stonybrook, USA) during the entire scan with the animal under isoflurane anesthesia. After fast low resolution localiser images, signal loss images (where SPION appears as hypointense) were acquired with a 3D gradient echo sequence (FLASH) with the following parameters: repetition and echo time (TR/TE) 14.3/5.9ms, flip angle 12°, a high isotropic resolution of 0.31mm (in-plane and slice thickness), field of view 100mm, acquisition time 9 minutes. Coronal or sagittal planes (or in fact any oblique) can be displayed from these 3D isotropic datasets, using Osirix software, in order to reconstruct any desired plane for best visulisation of anatomy.

2.6. Animal experiments

2.6.1. Animal handling

All animal experiments except the determination of the iron load in bone marrow were carried out by Azza Gramoun at UniGen. [230, 236] Female Lewis rats were obtained from Janvier Labs (Cedex, France). The rats weighed between 150 and 175g and were 6-8 weeks old on arrival. They were housed in the animal facility at the University of Geneva under pathogen-free conditions in standard cages and were fed standard diet and water ad libitum. Animal handling was in accordance with guidelines of the Swiss Committee of Animal Experiments. The experimental protocol was approved by the Animal Care Committee at the University of Geneva (authorization no.1049/3580/3).

2.6.2. Injection of A-PVA-SPION labeled hMSCs

The local administration of A-PVA-SPION-labeled MSCs was performed by Azza Gramoun at the University of Geneva.[230] For *in vivo* visualization of labeled cells, the A-PVA-SPION-labeled and the non-labeled MSCs were injected intra-articularly into the right and left naïve knee joints of Lewis rats (Janvier Labs, Cedex, France) respectively.

2.6.3. Systemic injection of A-PVA-SPIONs

The systemic administration of A-PVA-SPIONs was performed by Azza Gramoun at the University of Geneva.[236] To assess the effect of A-PVA-SPIONs accumulation in bone marrow, $7mg_{Fe}$/animal was injected intravenously through the tail vein. For this, the pH of A-PVA-SPIONs in their solvent HNO_3 was adjusted to pH 7.3 using 1M NaOH prior injection. Control animals were injected with the same volume of normal saline. The animals were sacrificed seven days later and the long bones of the hind limbs were harvested and stored in sterile PBS + 1% pen/strep on ice prior to cell isolation.

2.6.4. Determination of iron load in bone marrow

Isolation of A-PVA-SPIONs from bone marrow was conducted by using a Magnetic Activated Cell Sorting (MACS®) device. For this, bone marrow was harvested from one control and two A-PVA-SPION injected animals (control animal: 499mg, A-PVA-SPION animal one: 422mg, A-PVA-SPION animal two: 209mg). The bone marrow of all three animals was harvested as described in section 2.8.1 with the following exception: Instead of re-suspension in expansion media, the harvested bone marrow was re-suspended in 8ml

MACS® separation buffer (Milteny Biotec GmbH, Bergisch Gladbach, Germany). For better dissolution of cell clusters and filtering of tissue debris, the re-suspended bone marrow was sequentially filtered using a 100µm and 30µm cell strainer. For separation of the magnetic (cell bound and free A-PVA-SPIONs) and the non-magnetic fraction MACS® MS columns (Milteny Biotec GmbH, Bergisch Gladbach, Germany) were used. In brief, the re-suspended bone marrow was split into equal volumes and applied on two separate MACS® MS columns to avoid column overload due to high cell concentrations. The magnetic fraction was eluted from the MACS® column by adding 1ml of MACS® separation buffer and centrifugation at 500x g for 1 min. The eluted magnetic fractions were mixed with equal volumes of 6N HCl to dissolve putatively trapped A-PVA-SPIONs for iron quantification by inductively coupled plasma optical emission spectrometry (ICP-OES). The total amount of iron was referenced to the respective mass of bone marrow.

2.7. Human mesenchymal stromal cells

2.7.1. Isolation

This study on the influence of A-PVA-SPIONs on human MSCs (hMSCs) was approved by the local ethical committee (EA2/028/12); all donors gave informed written consent. Primary human MSCs were isolated from bone marrow of human donors (8 male, mean age: 59 ± 9.1 years; 7 female, mean age: 60 ± 16.6 years) undergoing hip surgery as described elsewhere.[40] For information about ethical consent for MoM-MSCs see section 2.4.1. The "culture medium" was Dulbecco's modified Eagle's medium (DMEM; Low Glucose, Gibco, Grand Island, NY) with 10% fetal calf serum (FCS; Biochrom AG, Berlin, Germany), 5mM L-alanyl-L-glutamine (Gibco, Grand Island, NY), 100 U/mL penicillin plus 100 µg/mL streptomycin. Cells were counted by using CasyTT for standard cell culture (Schärfe Systems, Reutlingen, Germany) or a Neubauer chamber (C-Chip, Peqlab, Erlangen, Germany) when only small volumes of cells were available.

2.7.2. Viability assays

Proliferation rates were assessed by using a CyquantNF® Cell Proliferation assay kit (Life Technologies, Carlsbad, CA, United States) and cell viability was assessed using PrestoBlue® (Life Technologies, Carlsbad, CA, United States) according to the respective manufacturers' protocol. Briefly, 2000 MSCs/cm2 were seeded into 48-well plates and measured after one (d1), four (d4) and eight (d8) days of culture. CyquantNF® values from d4 and d8 were normalized to d1. PrestoBlue® values were normalized to relative cell number determined by CyquantNF®. All measurements were performed in triplicates using a multimode microplate reader (m200 pro, Tecan).

2.7.3. Functional assays

Osteogenic differentiation of 2.4 x 10^4 MSCs per 24-well was induced by supplementing culture media with 200 µM ascorbic acid, 7 mM ß-glycerol phosphate, 0.01 µM dexamethasone for 13 days. The calcified matrix was visualized by Alizarin Red S (AR) and quantified photometrical by dissolving AR in 10% cetylpyridinium chloride (readout wavelength at λ=562nm). Adipogenic differentiation was induced by supplementing culture media with 1 µM dexamethasone, 2 µM insulin, 200 µM indomethacin and 500 µM isobutyl-methyl-xanthin for 14 d. For A-PVA-SPION labeled MSCs, fatty acids were detected by OilRed O staining and quantified photometrical by dissolving in 100% isopropanol (readout wavelength at λ=500nm). For MoM-MSCs, fatty acids were detected using NileRed staining

and quantified by fluorescence emission (excitation: 485nm/emission: 540nm) normalized to relative cell number by 4′,6-Diamidin-2-phenylindol (DAPI) staining (excitation: 355nm/emission: 460nm). Each experiment was conducted in triplicate. Chondrogenesis was induced by stimulating a pellet culture (3 x 105 cells/pellet) with FCS-free culture media plus 10 ng/mL transforming-growth-factor beta 1 (TGF-β1), 10–7 M dexamethasone, 50 µg/mL ascorbic acid, 40 µg/mL proline, 100 µg/mL pyruvate, 6.25 µg/mL insulin-transferrin-selenium (ITS), 1.25 mg/mL bovine serum albumin (BSA), 5.35 mg/mL linoleic acid) for 21 d and detected by Alcian Blue staining and quantification of proteoglycan as described elsewhere with the modification for pellet cultures and optimized read out wavelength (λ= 516nm).[42]

For evaluating the influence of MoM wear on hMSCs total ALP activity *ex vivo*, 1.5 x 10^4 MoM-MSCs and Ctrl.-MSCs were seeded. Media change was conducted at day 3. Baseline total ALP activity was measured at day 0 (24 hours after seeding). Total ALP activity of stimulated and non-stimulated cells was measured at day 5. For total ALP activity measurement, all buffers and substrate were preheated to 37°C. Cells were washed using 400 µl PBS and 500 µl AP-Buffer (100 mM NaCl, 100 mM Tris, 1 mM MgCl2; pH 9.0). 250 µl AP-Buffer and an equal volume of *p*-nitrophenyl phosphate (*p*NPP, Sigma Aldrich, St. Louis, MI, United States) solution (1 mg/ml in 1 M diethanolamine (DEA, Sigma Aldrich, St. Louis, MI, United States, pH 9.8) were added. Cells were incubated for 10 min at 37 °C and reaction was stopped using 500 µl 1 M NaOH (Sigma Aldrich, St. Louis, MI, United States). Duplicates of 100 µl were transferred to a 96-well plate and absorption was measured at 405 nm at a multimode plate reader (Tecan Group AG, Maennedorf, Switzerland). After blank value subtraction, *p*NPP consumption, i.e. 4-nitrophenolate accumulation, was calculated using the corresponding molar extinction coefficient of 18,450 L x mol-1 x cm-1. Values were normalized to total cell viability determined in advance as described in 2.7.2. Each experimental condition was conducted in triplicates.

Migration rate of A-PVA-SPION labeled and MoM wear exposed hMSCs was analyzed in culture inserts for self-insertion (IBIDI, Munich, Germany) and performed in duplicates as according to the manufacturers'' instructions. 8x10³ cells were allowed to attach for 5h in each cavity of the insert prior to insert removal and addition of culture media with 5µg/ml Mitomycin C (Sigma-Aldrich, St. Louis, USA). Migration into the defined cell free gap (500 µm) was observed for 24h under an inverted microscope (DMI6000B, Leica, Germany) with a

live cell imaging system, taking images every 20min. Assay analysis (area covered by cells) was performed with Tscratch.[237]

2.7.4. Labeling and dosimetry

Prior use, A-PVA-SPIONs underwent sonication for 1 min and pH-adjustment to neutral range (7.2 - 7.6) using 1M NaOH. Adherent MSCs (80-90% confluence) were washed with PBS and incubated with A-PVA-SPION containing FCS-free culture media for 4h (n=4) with fixed media height (1.3 mm) throughout different culture vessels to prevent variations in the administered dose. Protamine was used at a final concentration of 5 µg/ml (n=2). If MSCs were labeled for 24h (n=2), 10% FCS was added after 4h for sufficient cell nutrition. Finally, A-PVA-labeled MSCs were washed 6x with PBS prior further use. For dosimetry calculations, a simplified model based on the ISDD developed by Hinterliter et al. was provided by Prof. Heinrich Hofmann that takes additive transport by diffusion and sedimentation into account.[166, 230] The error compared to the ISDD model is reasonably small compared to all the uncertainty arising from the *in vitro* agglomeration and formation of the protein corona, both influencing the diameter and density of the particles. The characteristic properties of the particles used for the calculation of the dose delivered to the cell surface are summarized in **Table 4**.

Table 4. Parameters for dosimetry calculations.

Property	Unit	Value
Density of SPION	g/cm^3	4.8
Atomic weight of Fe	g/mol	55.845
Atomic weight of Oxygen	g/mol	15.999
Molecular masse of Fe2O3	g/mol	159.66
Molecular mass of Fe3O4	g/mol	231.495
Density of solvent	g/cm^3	1
PVA layer density	g/cm^3	1.025
PVA-SPION diameter at pH7	nm	45
Molecular weight of Protein	g/mol	70000
Specific volume of protein	cm^3/g	0.733
Density of a random loose packed agglomerate		0.54
PVA/SPION weight ratio		9
Number of SPION / PVA-bead		3
Diameter of PVA/SPION	nm	45
Diameter of SPION	nm	7.5
Density of PVA_SPION suspension	g/cm^3	1.0009
Viscosity	Pa s	0.001
Cell size (projected area)	cm^2	4.00E-06
Temperature	°C	37
Suspension height in the well	mm	1.3

2.7.5. Determination of cell bound iron

After centrifugation at 400xg, the cell pellet was dried overnight at 50°C, re-suspended in 125µl 6N HCL followed by a second overnight incubation step at 50°C. 25µl sample was then mixed with 25µl 6N HCL followed by adding 50µl of 5% K4[Fe(CN)6] (Merck, Darmstadt, Germany). After 20min, absorbance was read at 690nm (m200 pro, Tecan, Männedorf, Switzerland) against a standard curve using $FeCl_3$. Each measurement was carried out in quadruplicate. To obtain cell bound iron, iron (pgFe/cell) was normalized to total cell number (average of 2 x 10^6 cells).

2.7.6. RNA expression analysis

MSCs from n=3 different donors were expanded in cell culture and labeled with A-PVA-SPIONs as described in section 2.7.4. For the control group, unlabeled cells from the same donors where used. Labeled and unlabeled MSCs where then seeded in cell culture inserts for migration experiments in quadruplicates and wound scratch assay was performed as described in section 2.7.3. After 24h of migration, the cells where washed 1x with PBS and their RNA was extracted using the RNeasy® Mini Kit (Quiagen, Venlo, Netherlands). The extracted RNA was then used as template for cDNA synthesis using the First Strand cDNA Synthesis Kit (Quiagen, Venlo, Netherlands). Gene expression analysis was performed using the RT² SYBR Green qPCR Mastermix (Quiagen, Venlo, Netherlands) and the RT² Profiler PCR Array for human cell motility (Quiagen, Venlo, Netherlands). All Kits where used according to the manufacturer's protocol. The qPCR was run on a Thermal Cycler with Multicolor Real-Time PCR Detection System (iQ 5 RTPCR qPCR, BioRad Laboratories Inc., Hercules, CA, United States). Raw data was analyzed using the iQ5 Software (BioRad Laboratories Inc., Hercules, CA, United States) for obtaining C_T values. The fold change in gene expression was calculated using a template provided with the RT² Profiler PCR Array for human cell motility based on the $2^{-\Delta\Delta C}{}_T$ method.[238] Among the expression data of all 91 genes tested, the data for 7 genes depicted in Figure 17 D was chosen according to the following criteria: the minimum fold change must be ≥ 0.1 AND the standard deviation of fold changes from the cells of the n=3 different donors must be ≤ 10%.

2.8. Human Osteoblast

2.8.1. Cell isolation

For Information about sample harvest and ethical consent see section 2.4.1. Spongiosa was washed with PBS until hematopoietic (red) cells were washed off completely and the remaining tissue appeared in bright white. The cleaned Spongiosa was cut into small pieces using a sterile scalpel. OBs where isolated from the small pieces of washed spongiosa by adherence to plastic in cell culture flasks. Cells were expanded under standard cell culture conditions (37°C, 5% CO2) in DMEM (Gibco, NY, United States) supplemented with 10 % FCS (Biochrom AG, Berlin, Germany), 5mM L-alanyl-L-glutamine (Gibco, Grand Island, NY, United States), 100 U/mL penicillin and 100 µg/mL streptomycin. Cells were counted using a CASY Model TT – Cell Counter and Analyzer (Schärfe Systems, Reutlingen, Germany).

2.8.2. Cell viability and proliferation

Proliferation rates were assessed by using a CyquantNF® Cell Proliferation assay kit (Life Technologies, Carlsbad, CA, United States) and cell viability was assessed using PrestoBlue® (Life Technologies, Carlsbad, CA, United States) according to the respective manufacturers' protocol. Briefly, 2000 OBs/cm^2 were seeded into 48-well plates and the respective assays were applied after one (d1) and four (d4) days of culture. CyquantNF® values from d4 and d1 where used to calculate population doublings. PrestoBlue® values were normalized to relative cell number determined by CyquantNF®. All measurements were performed in triplicates using a multimode microplate reader (m200 pro, Tecan).

2.8.3. Matrix mineralization

For matrix mineralization, 2.4 x 10^4 OBs were seeded out per 24-well. Matrix mineralization was induced by supplementing a 1:1 mixture of cell culture media (see section 2.8.1.) and HAMs F12 media (Gibco, NY, United States) with 200 µM ascorbic acid, 7 mM ß-glycerol phosphate, 0.01 µM dexamethasone for 28 days. The calcified matrix was visualized by Alizarin Red S (AR) and quantified photometrical by dissolving AR in 10% cetylpyridinium chloride (readout wavelength at λ=562nm).

2.9. Rat mesenchymal stromal cells

2.9.1. Isolation from bone marrow

Bone marrow was harvested from femur and tibia of both lower limbs from each animal as described.[239] Prior further use, the total amount of extracted bone marrow was weighted and used for either CFU assay and subsequent rat MSC (rMSC) isolation, or determination of iron load. rMSCs were isolated and selected by plastic adherence.[239] Cells were expanded under standard cell culture conditions (37°C, 5% CO2) in DMEM (Gibco, NY, USA) supplemented with 10 % FCS (Biochrom AG, Berlin, Germany), 5mM L-alanyl-L-glutamine (Gibco, Grand Island, NY), 100 U/mL penicillin and 100 µg/mL streptomycin. The harvested bone marrow was re-suspended in 33ml of expansion media and split into 30 ml and 3 ml, for plastic adherence selection and colony forming unit (CFU) assay, respectively. Cells were counted using a CASY Model TT – Cell Counter and Analyzer (Schärfe Systems, Reutlingen, Germany).

2.9.2. Viability and proliferation assays

The assays concerning proliferation, mitochondrial activity and membrane activity of rMSCs were performed at passage one. Relative cell number was assessed by determination of total DNA content using a the fluometric cyanine dye-based CyquantNF® Cell Proliferation assay kit (Life Technologies, Carlsbad, CA, United States). Mitochondrial activity was assessed using the fluometric resazurin-based assay reagent AlamarBlue® (Life Technologies, Carlsbad, CA, United States). Membrane integrity was assessed using the CytoTox-ONE™ Homogeneous Membrane Integrity Assay (Promega Corporation, WI United states). All assays were performed according to the manufacturer's protocol. Briefly, 2000 rMSCs/cm2 were seeded into 96-well plates and expanded under standard cell culture for four days. The assays were then performed at day four (d4) and day seven (d7). CyquantNF® values from d4 and d7 were used to calculate population doublings within three days according to the following formula:

$$population\ doubling = log10(\frac{d7}{d4})/log10(2)$$

AlamarBlue® and CytotoxOne™ values for d7 were normalized to the relative cell number acquired by the corresponding CyquantNF® values. All measurements were performed in triplicates using a multimode microplate reader (m200 pro, Tecan, Switzerland).The CFU

assay was performed in duplicates for each animal. 33 ml of cell suspension was prepared according to material and methods section for bone marrow harvest and isolation of rMSCs from rats. For later normalization, the total amount of extracted bone marrow was weighted prior suspension in cell culture media. 30 ml of the cell suspension were used for rMSC isolation by plastic adherence selection while the remaining 3 ml were further used for the CFU assay. For this, 2 x 1ml of cell suspension were mixed with an equal volume of expansion media and transferred into the cavity of a 6well plate, followed by seven day cultivation under standard cell culture conditions. Prior determination of CFU number, the cells were fixed in 4% formaldehyde for 10 min at RT.

2.9.3. Functional assays

The rMSCs ALP expression was investigated histochemically by using the Blue Alkaline Phosphatase Substrate KIT III (Vector® Labs, Burlingame, CA, US) according to the manufacturer's protocol. Cell Nuclei were counterstained with nuclear fast red for 10min at RT. The number of CFUs was determined by considering more than 30 adjacent cells as a colony. A colony was considered ALP positive when more than 50% of the rMSCs showed ALP expression. The number of colonies was referenced to the total amount of harvested bone marrow to obtain the number of CFUs per mg bone marrow.

Random migration of rMSCs was assessed at passage one using a modified Boyden chamber assay. For this, polycarbonate transwell inserts (8 μm pore size; Nunc, Wiesbaden, Germany) were placed in a cavity of a 24 well plate in duplicates. $3x10^4$ rMSCs were seeded on top of the insert and kept under standard cell culture conditions for 4h and 30h. After incubation time passed, cells were washed 1x with PBS and kept in FA for 10min. at RT for fixation. Non-migrated cells were scraped off the upper side of the filter using a cotton stick and remaining migrated cells were incubated with 10 μg/mL Hoechst33342 (Life Technologies, Carlsbad, CA, United States) in PBS for 10min. at RT for staining the cells nuclei. The filter membranes were cut out from the transwell inserts using a scalpel and mounted on glass slides using FluoromountG (SouthernBiotec, AL, United States) and a cover glass. For quantification of migrated cells, nine different fields of views per filter were imaged using an inverted fluorescence microscope (AF 6000, Leica microsystems, Wetzlar, Germany). Determining the number of migrated cells was performed using ImageJ and an in-house developed cell counting macro. The number of migrated cells after 4h was then normalized to the number of migrated cells after 30h.

2.10. Statistics

2.10.1. A-PVA-SPIONs for cell labeling *in vitro*

All statistical analyses were performed using SPSS Statistics 22 (IBM, NY, United States). When performing multiple pair-wise comparisons, one-way or two-way analysis of variance (ANOVA) were performed, and p-values were adjusted using Bonferroni's p-value adjustment multiple comparison procedure. Results are presented as mean ± standard deviation (SD). P-values < 0.05 were considered statistically significant. Gene expression data was tested for statistical significance by Student's t-test (independent samples, two-tailed, $p < 0.05$ was considered as statistical significant)

2.10.2. A-PVA-SPIONs for contrast enhancement in bone marrow

All statistical analyses were performed using SPSS Statistics 22 (IBM, NY, United States). All data sets from individual experiments were tested for normal distribution by Shapiro-Wilks test prior testing for statistical significance. All data was tested for statistical significance by Student's T-test (independent samples, two-tailed, $p < 0.05$ was considered as statistical significant). In Figure 28, MRI data is presented as mean ± standard deviation. In Figure 19 to Figure 21 the individual data points for each animal are represented by the same symbols in each graph to fully visualize their inter-individual spreading instead of presenting the corresponding standard deviation only. Here, the black bars represent the mean.

2.10.3. The influence of *in vivo* exposure with MoM wear

All statistical analyses were performed using SPSS Statistics 22 (IBM, NY, United States). All data sets from individual experiments were tested for normal distribution by Shapiro-Wilks test prior testing for statistical significance. All data was tested for statistical significance by Student's t-test (independent samples, two-tailed, $p < 0.05$ was considered as statistical significant).

3. Results

3.1. **Engineered A-PVA-SPIONs for hMSC labeling**

3.1.1. A-PVA-SPION interference with viability and proliferation assays

Prior to analyzing the impact of A-PVA-SPIONs on MSC viability and proliferation, the interference of A-PVA-SPIONs with colorimetric and fluorescence-based proliferation and viability assays was investigated, which could produce false results, as already reported for other nanomaterials.[168] It was thus investigated if A-PVA-SPIONs change experimental read outs by direct interaction with *in vitro* assays. For investigation of the cells metabolic activity a colorimetric MTS and a flourimetric Resazurin-based assay where chosen. For determination of proliferation a flourimetric Cyanine-dye based assay was chosen. The obtained results revealed a dose-dependent signal increase for the colorimetric MTS-based assay and signal quenching for the fluorescent Cyanine dye- and Resazurin-based assay in the presence of 1 to 1000 μg_{Fe}/ml A-PVA-SPIONs (**Figure 11**). Interestingly, for the colorimetric MTS assay this effect seems even more pronounced in a cell-free system as opposed to the fluorescence Cyanine dye assay. In summary, assay interference was not observed for an A-PVA-SPION concentration of about 1 µgFe/ml (0.1 µg total iron). Concentrations above this threshold should thus be avoided in later *in vitro* experiments using the respective colorimetric or flourimetric assays.

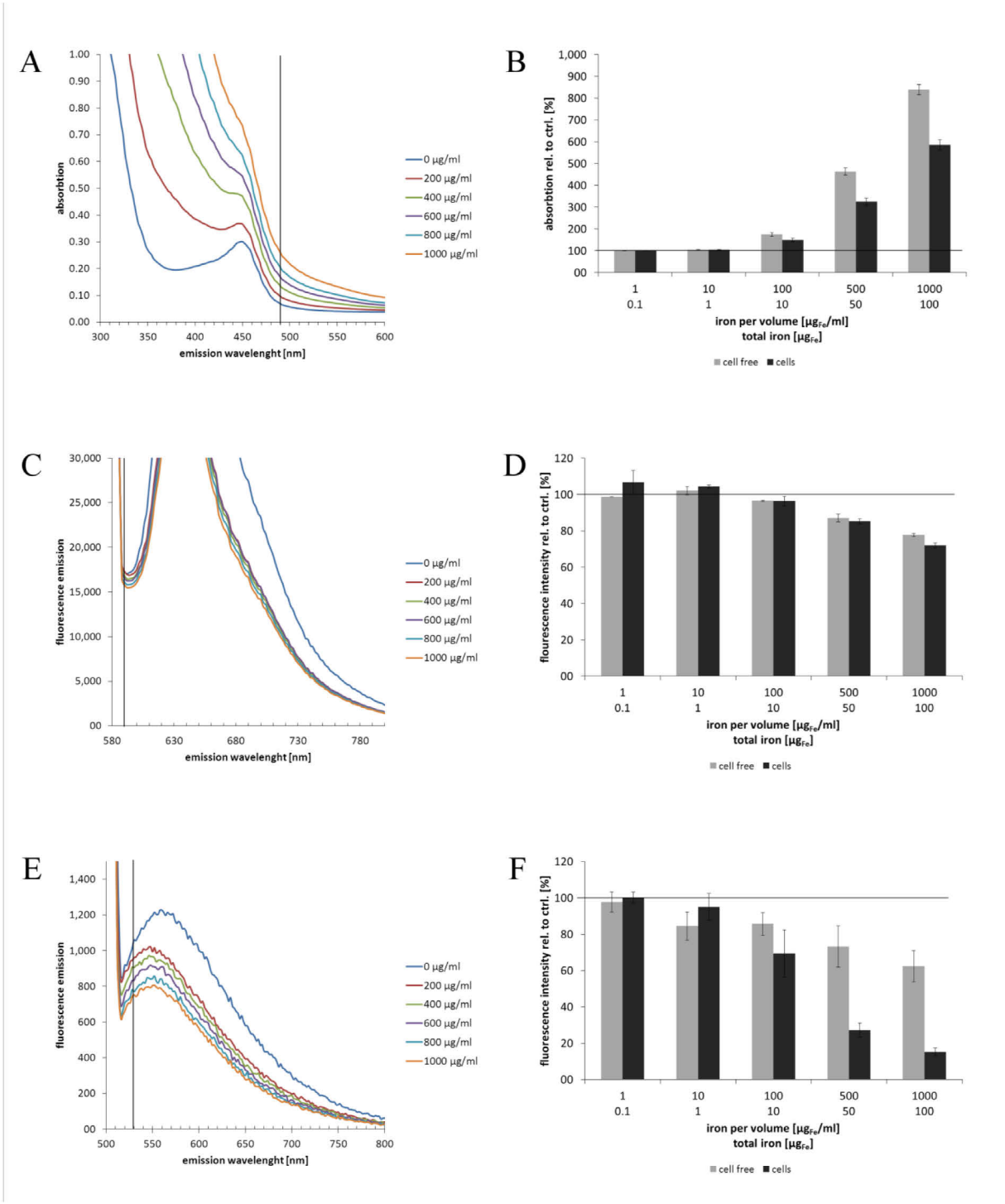

Figure 11. A-PVA-SPIONs interfere with viability and proliferation assays at high concentrations.

Shown are the absorption- or emission-spectra - with a special focus on the corresponding readout wavelengths - of (A, B) MTS-, (C, D) Resazurin-, and (E, F) Cyanine dye-based viability assays in the presence of increasing A-PVA-SPION concentrations with and without MSCs. (A, C, E) Black line indicates the corresponding read out wavelength.

3.1.2. *In vitro* exposure of hMSCs to A-PVA-SPIONs for cell labeling

For the development of an efficient labeling procedure, it was initially investigated whether A-PVA-SPIONs are internalized by hMSCs *in vitro* without any external support such as transfection agents or magnetic fields. To confirm cellular internalization, we used methods beyond Prussian Blue staining that allow resolution in the nanoscale: TEM and transmission TXM. For this purpose, hMSCs were incubated for four hours with A-PVA-SPIONs ($100 \mu g_{Fe}$/ml) under serum-deprived conditions, which is known to be beneficial for efficient internalization.[217] The qualitative assessment of A-PVA-SPION internalization was facilitated by TEM and TXM. TEM revealed that A-PVA-SPIONs are internalized by MSCs and stored in intracellular vesicles (mean vesicle diameter: 357 ± 68.4 nm) (**Figure 12**). TXM supported these findings (mean vesicle diameter: 387 ±48.4 nm) and provided additional information that A-PVA-SPIONs are also found in smaller high contrast spheres (mean sphere diameter: 52 ± 9.2 nm), clusters of irregular shape, and a micron-sized cluster (length: 2000 nm; width: 291 nm) in the cytoplasm (**Figure 13**).

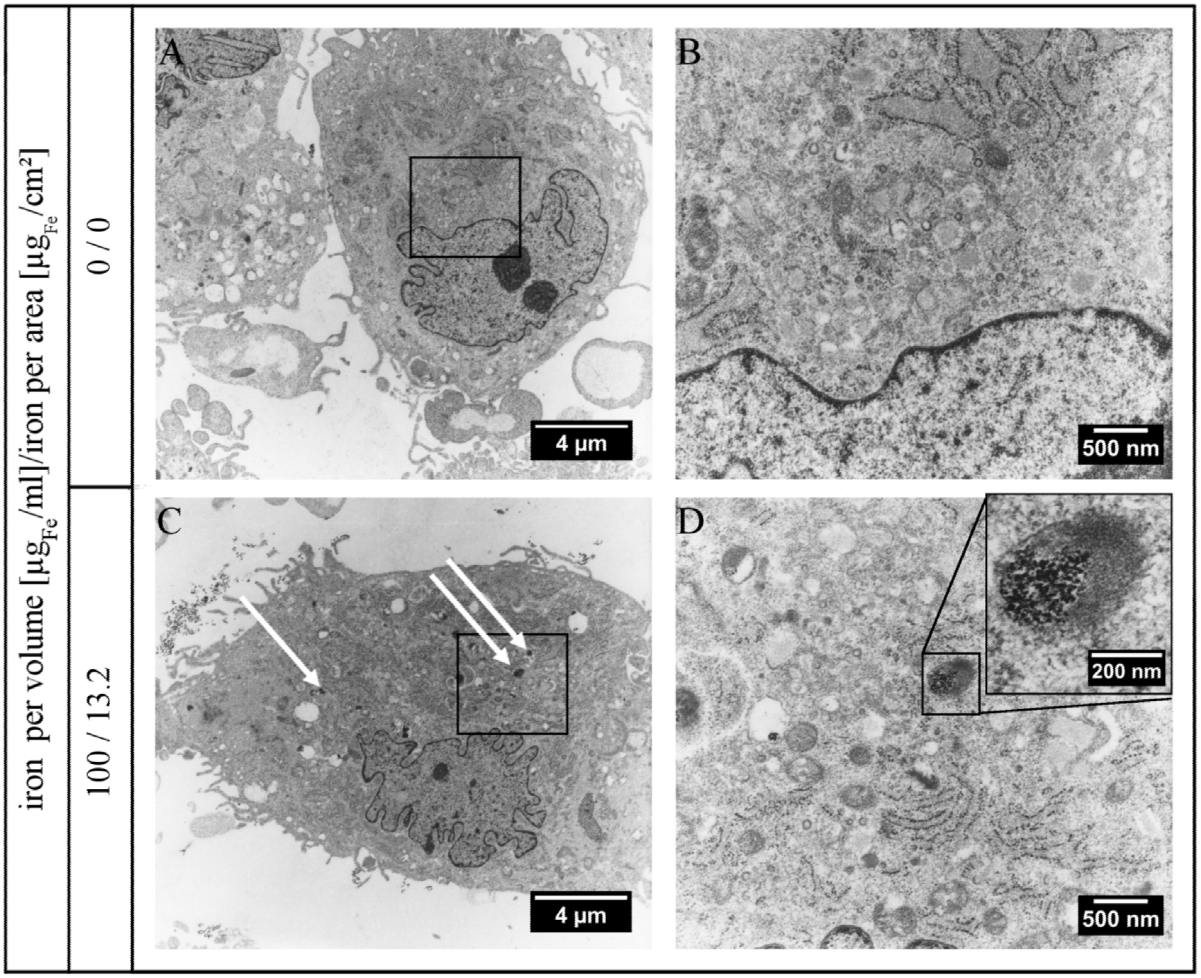

Figure 12. A-PVA-SPIONs are internalized by MSCs that store them in intracellular vesicles.

Shown are two representative pictures of (A, B) non-labeled and (C, D) A-PVA-labeled MSCs at different magnification detection by TEM. A-PVA-SPIONs are visible as intra-vesicular colloids (white arrows) in labeled MSCs that are absent in unlabeled control cells.

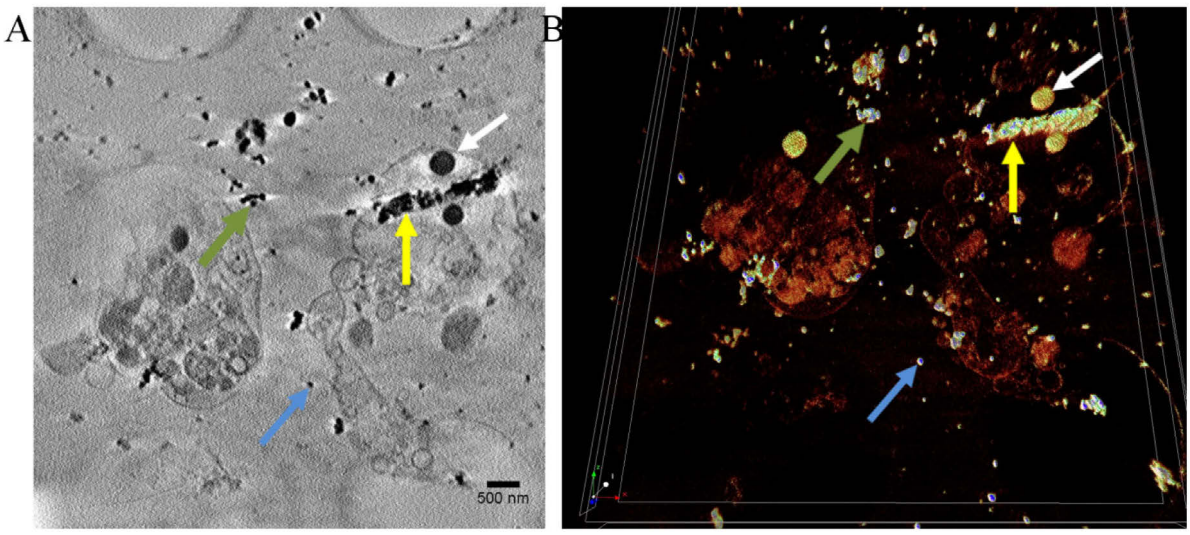

Figure 13. Internalized A-PVA-SPIONs are differently distributed in cytoplasm.

The acquired tilt series of A-PVA-SPION-labeled MSCs by TXM allowed tomographic reconstruction. Shown are (A) one slice from z-stack and (B) subsequent 3D modeling. A-PVA-SPIONs are visible not only as intravesicular colloids (white arrows), but also as smaller high contrast spheres (blue arrows), clusters of irregular shape (green arrows), and as a micron-sized cluster (yellow arrow) in the cytoplasm.

After having proven that A-PVA-SPIONs are internalized by hMSCs, we sought experimental conditions to optimize their cellular dose and define the corresponding dosimetry. Reporting a comprehensive dosimetry that consists of the administered, delivered and cellular dose is crucial for the establishment of a correct dose-response relationship.[164] The administered dose itself only describes the amount of NPs that was employed at the beginning of the experiment. A more relevant metric is described by the delivered dose that also takes the particles colloidal behavior and the exposure time into account and gives thus information about the amount of particles that reaches the cell monolayer.[165] Finally the cellular dose can be determined experimentally and describes the amount of A-PVA-SPIONs internalized by the cells. For this, hMSCs were incubated with varying concentrations of A-PVA-SPIONs (administered dose) and the corresponding cell-bound iron (cellular dose) was determined. After four hours, the value for cell-bound iron reaches 5.9 ± 2.5 pg/cell at the lowest administered dose (50µg Fe/ml), which does not further increase significantly at higher administered doses. The TA Protamine had no beneficial effect (ANOVA, p=0.126) on this pattern (**Figure 14 A**). However, when incubation time was extended to 24 hours, an increase of cell-bound iron was observed (ANOVA, p=0.014).

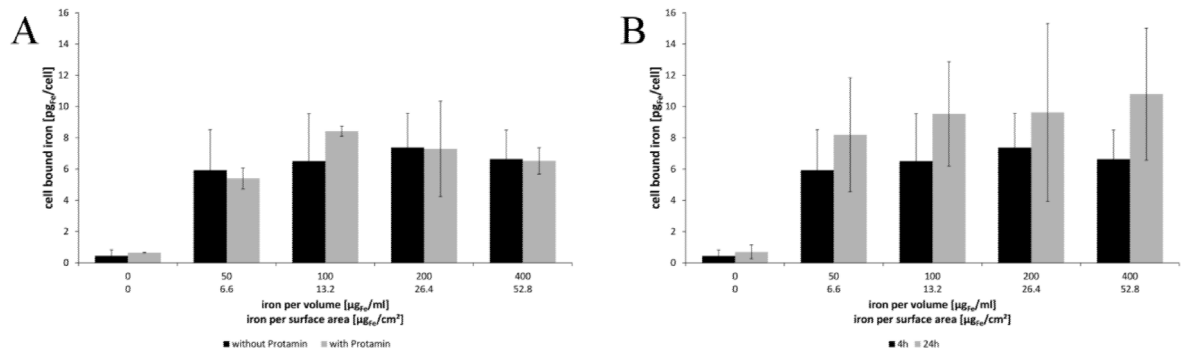

Figure 14. Efficient labeling of MSCs with A-PVA-SPIONs can be achieved at low administered doses and does not require Protamine.

MSCs were incubated with A-PVA-SPIONs (A) for 4h with and without Protamine under serum-free conditions and (B) for 24h in the absence of Protamine.

Table 5. Dosimetry of A-PVA-SPIONs *in vitro.*

dose	unit	time point					
administered	[µg/ml]	0h	0	50	100	200	400
	[µg/cm²]	0h	0	6.6	13.2	26.4	52.8
delivered	[µg/cm²]	4h	0	1.6	3.2	6.4	12.9
		24h	0	3.9	7.9	15.9	31.7
	[pg/cell]	4h	0	3	6	12	24
		24h	0	7.5	15	30	60
Cellular	[pg/cell]	4h	0.4 ± 0.3	5.9 ± 2.5	6.5 ± 3.0	7.4 ± 2.2	6.6 ± 1.9
		24h	0.7 ± 0.5	8.2 ± 3.6	9.5 ± 3.3	9.6 ± 5.7	10.8 ± 4.2

After 24 hours, the cell-bound iron increases to 8.2 ± 3.6 pg/cell at the lowest administered dose (50µg$_{Fe}$/ml), this is again not affected by increasing the administered dose (**Figure 14 B**). For accurate interpretation of the results and comparability with other studies, a summary of the particle dosimetry results is given in **Table 5**. In summary, we found that an optimized cellular dose in MSCs is reached at A-PVA-SPION-labeling for 4h under serum-deprived conditions followed by 20h under standard MSC culture conditions without the need of additional Protamine as TA.

3.1.3. Internalized A-PVA-SPIONs stimulate the migration rate of hMSCs

When using A-PVA-SPIONs for MSC-labeling in cell-based therapy approaches, compromising effects on MSC survival and function have to be avoided. It was thus investigated if viability, multilineage differentiation and migration of MSCs change after A-PVA-SPION-labeling with four different administered doses ranging from 0 to 100µg$_{Fe}$/ml. Based on the previously determined cellular doses, the expected amount of cell bound iron in proliferation and metabolic activity assays (48-well format) was calculated. It was found that the amount of cell bound iron does not exceed 1µg/ml, the critical threshold for assay interference (cell bound iron: 8.3 pg/cell; cells/well: 1800; total iron/well: 15 ng; iron concentration/well: 75 ng/ml). Thus, the expected interferences on these assays are negligible. Viability and proliferation of A-PVA-SPION-labeled MSCs was assessed after four and eight days and found to be unaffected compared to unlabeled MSCs (**Figure 15**). Differentiation of A-PVA-SPION-labeled MSCs towards the adipogenic, osteogenic, and chondrogenic phenotype was achieved without differences to their respective controls (**Figure 16**). Migration was analyzed in a modified wound scratch assay. A-PVA-SPION-labeled MSCs exhibit an increase in migration rate compared to unlabeled controls (**Figure 17 A, B**). Quantitative analysis revealed that this effect reaches statistical significance at the highest analyzed A-PVA-SPION concentration (50µg$_{Fe}$/ml *vs.* control: p=0.069; 100µg$_{Fe}$/ml *vs.* control: p=0.001). To evaluate if this effect on migration is either mediated by the A-PVA-SPIONs materials or by the NP itself, unlabeled MSCs where exposed to ferrous ions (Fe^{3+}) and PVA (polymer in solution) for 24h at concentrations equal to what MSCs encounter after labeling with A-PVA-SPIONs. The migration rates were then compared to those of untreated control MSCs and, in contrast to A-PVA-SPION labeled MSCs, found unchanged (**Figure 17 C**). To analyze if the observed changes in migration upon A-PVA-SPION labeling are reflected on the mRNA expression level, an array of genes involved in migration was investigated by qPCR. Among the 94 genes tested for their mRNA expression, seven were found to be altered. Four out of seven genes were altered significantly upon A-PVA-SPION labeling, namely endothelial growth factor (EGF), vascular endothelial growth factor-A (VEGF-A), protein tyrosine kinase 2 (PTK2) and rho-associated, coiled-coil-containing protein kinase 1 (ROCK1) (normalized mRNA expression relative to unlabeled control: E_{EGF}=1.61, E_{VEGF-A}=0.73, E_{PTK2}=0.86, E_{ROCK1}=0.9) (**Figure 17 D**). In summary, these results show that A-PVA-SPION-labeling does not affect differentiation, a key function of MSCs as defined by ISCT, but rather stimulates their migratory behavior.[36]

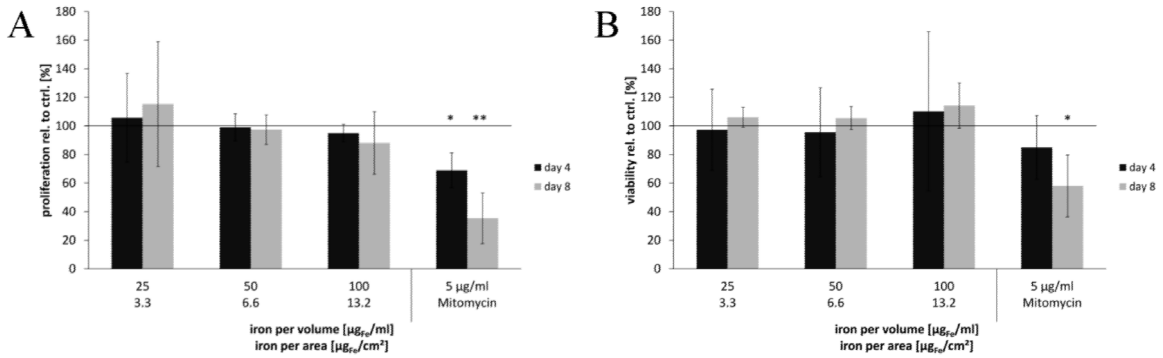

Figure 15. Proliferation and viability of MSCs are not affected by A-PVA-SPION-labeling.

(A) Proliferation and (B) viability of A-PVA-SPION-labeled MSCs was assessed after four and eight days.

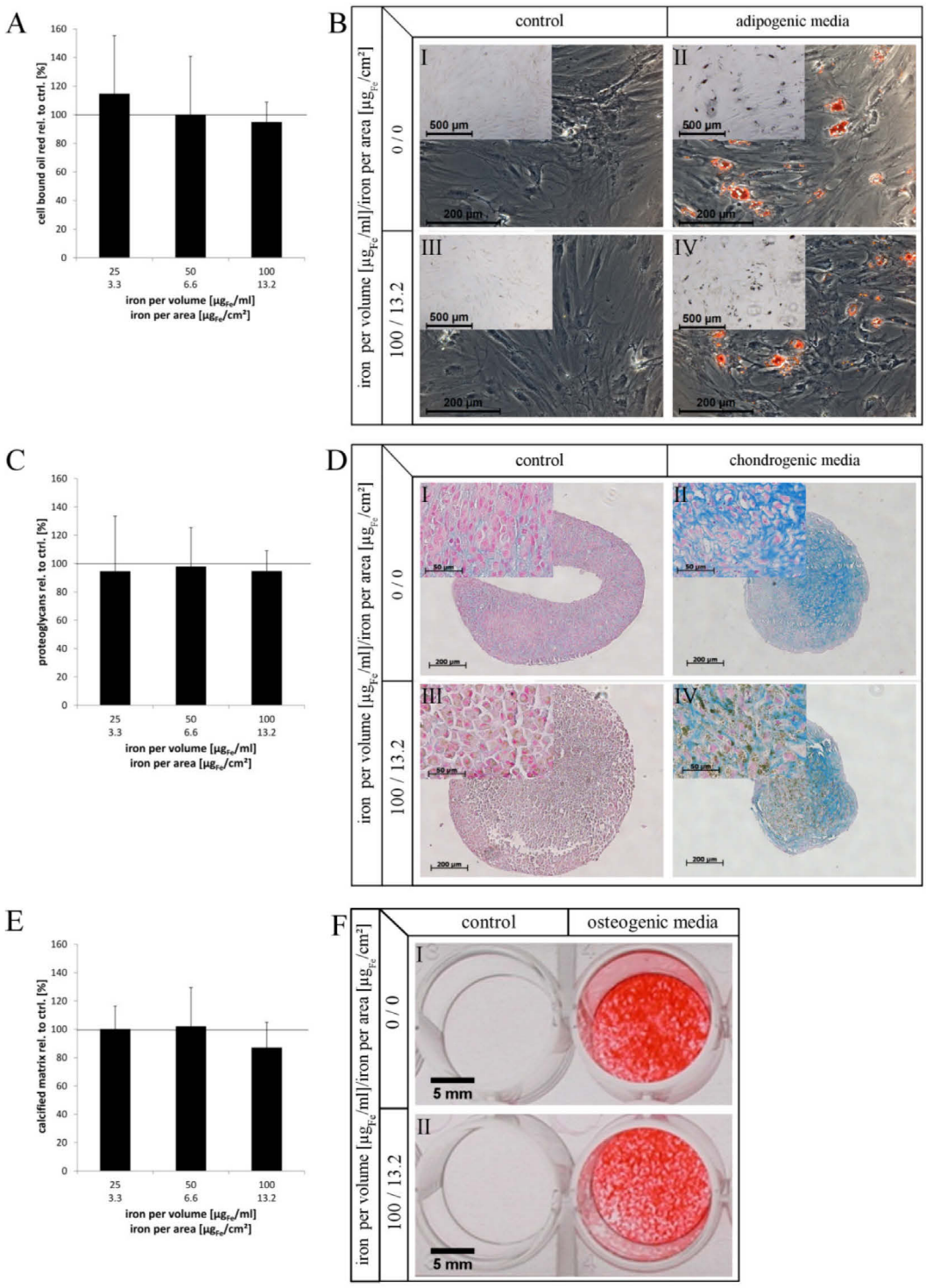

Figure 16. Differentiation capacity of MSCs is not influenced by A-PVA-SPIONs.

A-PVA-SPION–labeled MSCs were (A+C+E) quantitatively and (B+D+F) qualitatively investigated towards (A+B) adipogenic differentiation by Oil red staining(C+D) chondrogenic differentiation by proteoglycan assay and Alcian blue staining, and (E+F) osteogenic differentiation by Alizarin red staining.

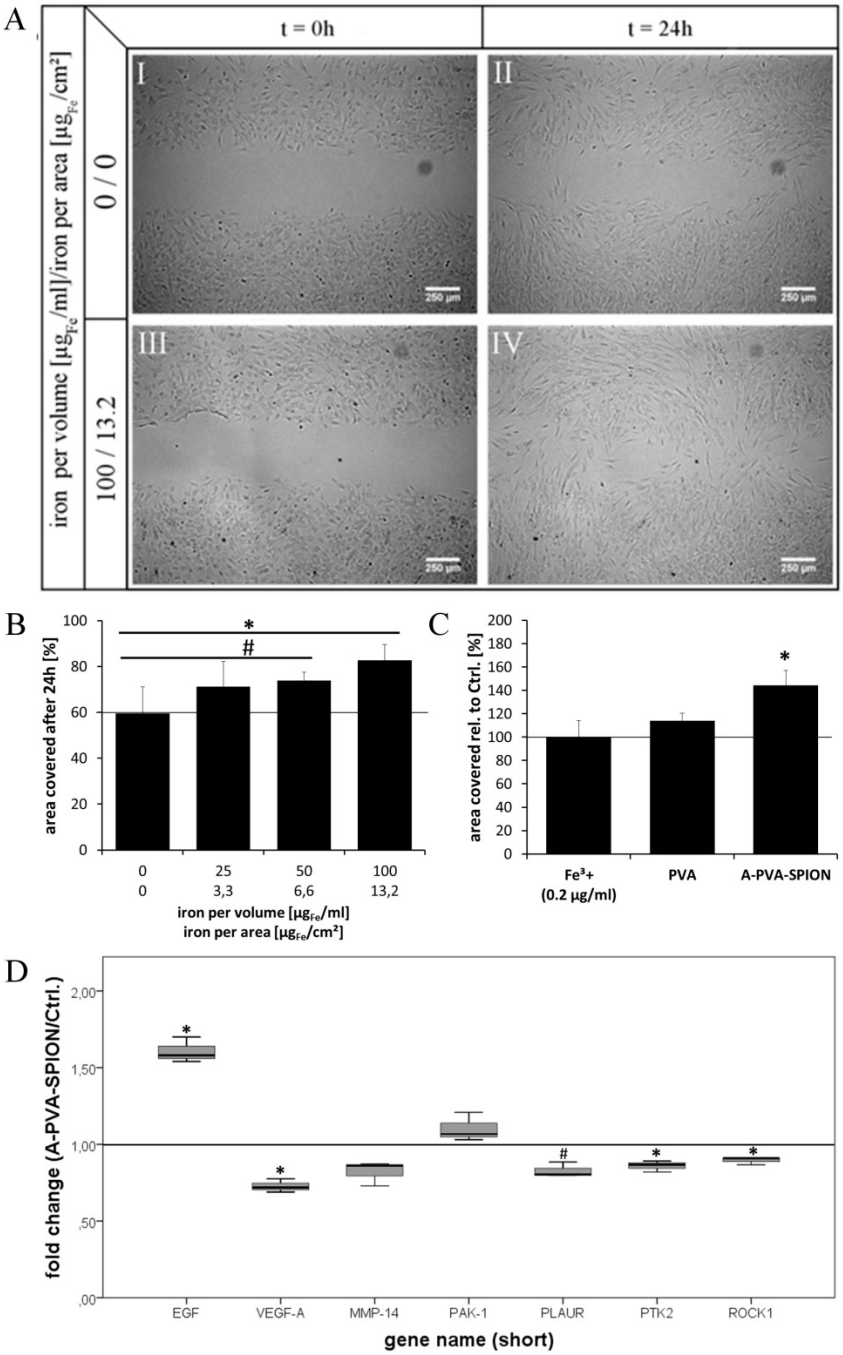

Figure 17. Migration of MSCs is stimulated by A-PVA-SPION-labeling.

(A) Representative images of the wound healing gap from one donor are shown. (B) Migration of A-PVA-SPION-labeled MSCs was quantified and analyzed in a wound healing assay for 24h (n=5; ANOVA, Post Hoc Bonferoni; *, p = 0.001; #, p = 0.069). (C) Migration of unlabeled MSCs (exposed to Fe^{3+} and PVA at concentrations equivalent to the cellular dose after labeling with 100 µg/ml A-PVA-SPIONs) and labeled MSCs (exposed to 100 µg/ml A-PVA-SPIONs) (n=3; Student's t-test; paired, two-sided, *, p ≤ 0.05). (D) Shown are changes in the expression of genes relevant for migration after labeling MSCs with 100 µg/ml A-PVA-SPIONs (n=3; Student's t-test, paired, two-sided; *, p ≤ 0.05; #, p = 0.053).

3.1.4. hMSCs labeled with A-PVA-SPION *in vitro* can be visualized in MRI

It was found that labeling of hMSCs with A-PVA-SPIONs had no negative effects on their viability or regenerative and it was therefore investigated whether the amount of cell-bound iron was sufficient for visualization of A-PVA-SPION labeled hMSCs using MRI *in vitro* and *in vivo*. To this end, cell phantoms with different numbers of A-PVA-SPION-labeled MSCs were prepared and scanned by MRI using T2 STIR and T1 VIBE sequences. A small effect could be seen using both sequences where a signal loss due to the A-PVA-SPION labeled hMSCs was detected only at the highest cell concentration on the transverse plane of the MR images (**Figure 18**). Acquisition of the orthogonal plane showed that the cells were concentrated at the bottom of the wells (data not shown). However, due to the small depth of the gel, which was lower than the minimum slice thickness available, the meniscal 'partial volume' effect precluded any quantification. Cell distribution was not homogenous enough to determine a precise effect of cell number on T1 and T2 star relaxation times. Nonetheless, the phantom results showed a trend in effect on T2 and indicated that MSC labeling was efficient for MRI visualization with the sequences used.

A I

Labelled cells [*10⁴]	A-PVA-SPION [µg$_{Fe}$/ml]
75	10
50	7.5
25	5
10	2.25
7.5	1
5	0.5
2.5	0.25
0	0

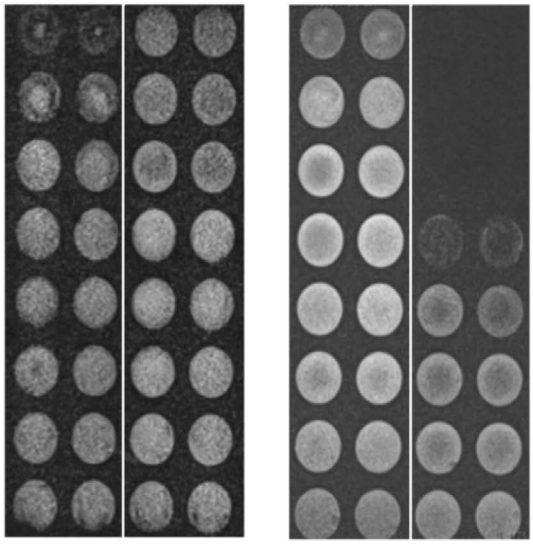

Figure 18. Visualization of A-PVA-labeled MSCs in MRI *in vitro.*

A diagrammatic representation showing the layout and (I) the different concentrations of A-PVA-SPION labeled MSCs and SPION alone used in the 24-well plate gel phantom study. (II) T1 weighted gradient echo MR images of the gel phantom and (III) T2 weighted (STIR) MR images of the same gel phantom.

3.2. Engineered A-PVA-SPIONs for contrast enhancement in bone marrow

3.2.1. A-PVA-SPIONs accumulate in bone marrow after systemic administration

Prior analysis of bone marrow rMSCs, their exposure to A-PVA-SPIONs due to accumulation in bone marrow after systemic administration was investigated. For this, MRI and magnetic sorting of bone marrow for later analysis through inductively coupled plasma optical emission spectrometry (ICP-OES) were employed. Both methods make use of the A-PVA-SPIONs magnetic properties and will thus only detect intact iron oxide crystals but not ferrous ions. In MRI, the presence of A-PVA-SPIONs in bone marrow was demonstrated by a clear negative contrast enhancement in the tibia of the lower limbs 24 hours and 7 days after injection. Such negative contrast was absent prior to injection (**Figure 28 A and B**). Furthermore, semi-quantitative analysis of the MRI data revealed a statistical significant change of the normalized signal after 24h ($p < 0.001$) and seven days ($p < 0.001$) post-injection for the A-PVA-SPION injected animals only (**Figure 28 C**). There was a significant ($p < 0.01$) but small decrease in the MRI signal intensity of 8.6% between 24h and 7 days for the A-PVA-SPION injected group. For quantification of the local exposure of rMSCs with A-PVA-

SPIONs after injection, bone marrow from three animals (two A-PVA-SPION injected and one control animal) was harvested after seven days and subjected to magnetic separation procedure under equal conditions. After centrifugation, accumulations of iron oxide crystals were macroscopically visible as brownish pellets in the magnetic fractions from A-PVA-SPION injected animals only (**Figure 28 D**). The eluted magnetic fractions from the three animals were then analyzed for their iron content by ICP-OES (**Table 6**). The iron concentration was found to be 10.36 and 11.07 $\mu g_{Fe}/mg_{BM}$ for the two A-PVA-SPION-injected animals compared to 0.86 $\mu g_{Fe}/mg_{BM}$ for the control animal (**Table 6**). The iron load in the bone marrow of A-PVA-SPION-injected animals corresponds to 3.62 and 3.89 $*10^{12}$ particles/mg_{BM}. The accumulation of A-PVA-SPIONs in bone marrow was further confirmed by histologic staining that detects both: iron oxide crystals and ferrous ions. Histology revealed Prussian blue positive deposits within the bone marrow of A-PVA-SPION injected animals that are absent in the respective controls (**Figure 28 E**). Accumulation of A-PVA-SPIONs in the bone marrow and subsequent 7 day exposure of local rMSCs were thus confirmed.

Table 6. Iron load of bone marrow in animals after A-PVA-SPION injection.

		animal		
		control	A-PVA-SPION	A-PVA-SPION
total Fe	[µg]	0.43	4.67	2.16
total bone marrow	[mg]	0.50	0.42	0.21
Fe/bone marrow	[µg/mg]	0.86	11.07	10.36

3.2.2. *In vivo* exposure with A-PVA-SPIONs alters rMSCs' viability and function

The following data was obtained by a master student working in this project under the authors supervision which included experimental design and evaluation of data.[240] The data presentation and respective statistics shown in this thesis were executed by the author himself. After *in vivo* exposure to A-PVA-SPIONs was confirmed, the rMSCs viability and function were investigated and found to be altered. Initially, the rMSCs' proliferation was assessed by fibroblast colony forming unit (CFU-F) assay and by determination of population doublings. The number of CFU-Fs per mg bone marrow was determined as a measure for the initial number of clonogenic rMSCs *in vivo*. There was no significant change ($p = 0.826$) in CFU-F number for cells that were exposed to A-PVA-SPIONs *in vivo* when compared to the control group (**Figure 19 A**). To validate the observation that proliferative capacities are not altered upon A-PVA-SPION exposure, rMSCs were expanded in cell culture until passage one and investigated for their population doublings as a measure of the cells proliferation rate *in vitro*. No significant differences ($p = 0.539$) were observed between A-PVA-SPION-exposed rMSCs and their controls regarding their population doublings (**Figure 19 B**).

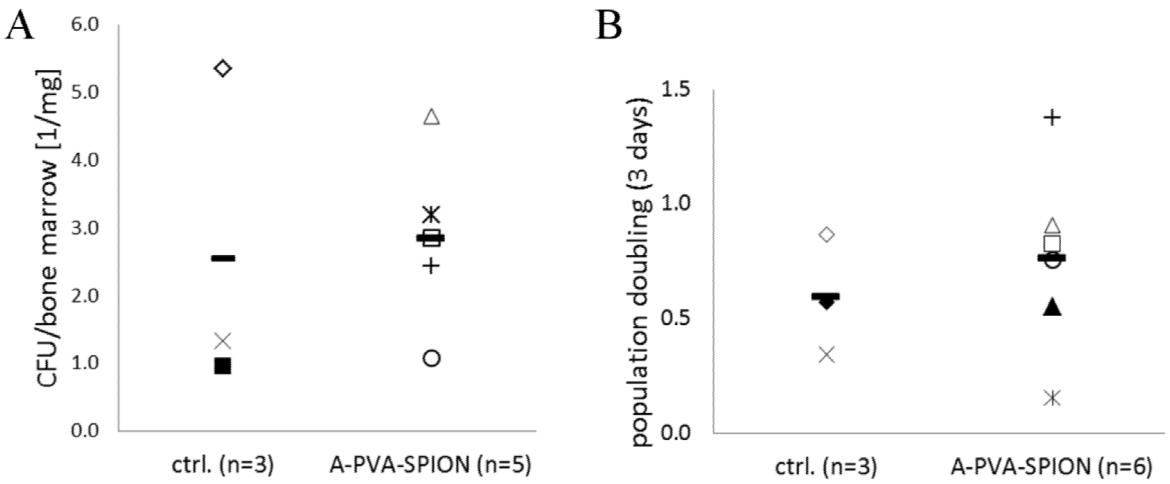

Figure 19. Proliferation of rMSCs is not affected by seven day exposure to A-PVA-SPION *in vivo.*

The *in vivo* presence of A-PVA-SPIONs in the bone marrow has no effect on (A) the number of clonogenic rMSCs *in vivo* and (B) the proliferation rate of rMSCs *in vitro*. Black bar represents mean, symbols represent the same individual animal in each graph.

The rMSCs' viability was assessed by determination of their cell membrane integrity and metabolic activity and the latter was changed for A-PVA-SPION exposed cells. Compromised membrane integrity or reduced metabolic activity would indicate cytotoxic effects in response to *in vivo* exposure with A-PVA-SPIONs. The membrane integrity of A-PVA-SPION-exposed rMSCs was not significantly ($p = 0.288$) affected compared to their respective controls (**Figure 20 A**). However, the rMSCs' metabolic activity was significantly ($p = 0.021$) increased upon *in vivo* exposure to A-PVA-SPIONs (**Figure 20 B**). Although this effect does not reflect an impaired viability as a reduced metabolic activity would, it indicates a cellular reaction of rMSCs on the A-PVA-SPIONs *in vivo*.

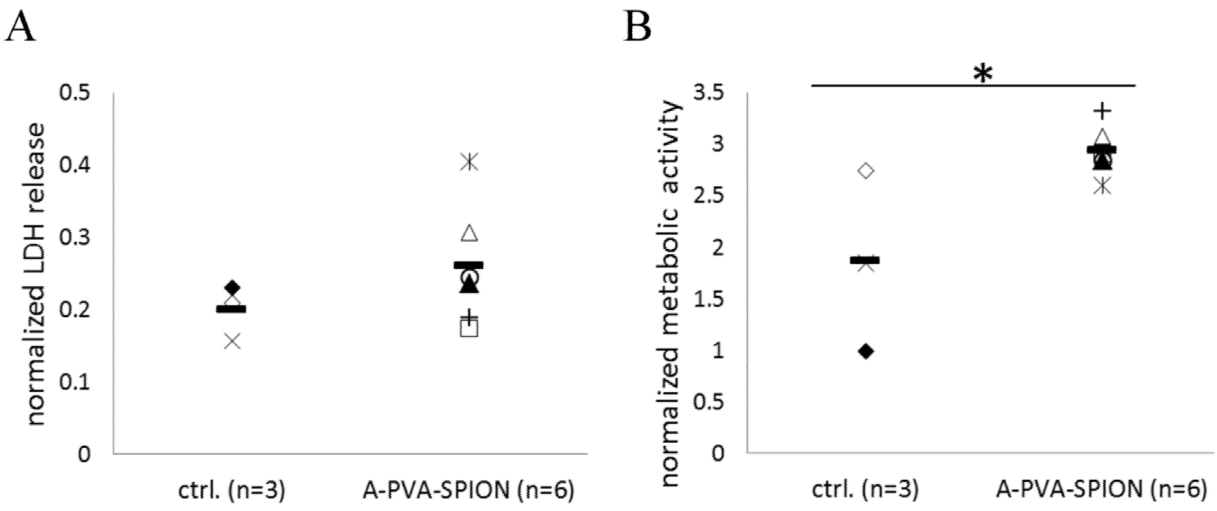

Figure 20. rMSCs metabolic activity but not membrane integrity is increased.

The rMSCs' viability is not diminished for A-PVA-SPION-injected animals, since (A) membrane integrity and (B) metabolic activity are not reduced. The significant increase in metabolic activity does however indicate a cellular reaction to the seven day exposure to A-PVA-SPION's *in vivo*. Black bar represents mean, symbols represent the same individual animal in each graph. (Student's ttest, two-sided, paired, * indicates $p < 0.05$)

Lastly, the rMSCs' function was assessed by determination of their Alkaline Phosphatase expression as a measure for osteogenic potential.[241] In addition, their migration rate was assessed. Both these functional aspects are vital for tissue regeneration in bone (e.g. fracture healing) and should not be impaired by the presence of A-PVA-SPIONs. To determine the amount of clonogenic rMSCs with osteogenic differentiation potential, Alkaline Phosphatase expression was investigated by histochemistry ($CFU\text{-}ALP^+$) at passage zero and found to be unchanged ($p = 0.610$) for cells from A-PVA-SPION-injected animals when compared to their controls (**Figure 21 A**). However, the migration rates of A-PVA-SPION-exposed rMSCs were significantly ($p = 0.037$) increased when compared to their controls (**Figure 21 B**). While an increase in cell migration is not detrimental regarding the rMSCs' function, it hints at an effect on the cellular level due to the seven day *in vivo* exposure to A-PVA-SPION, similar to the increased metabolic activity.

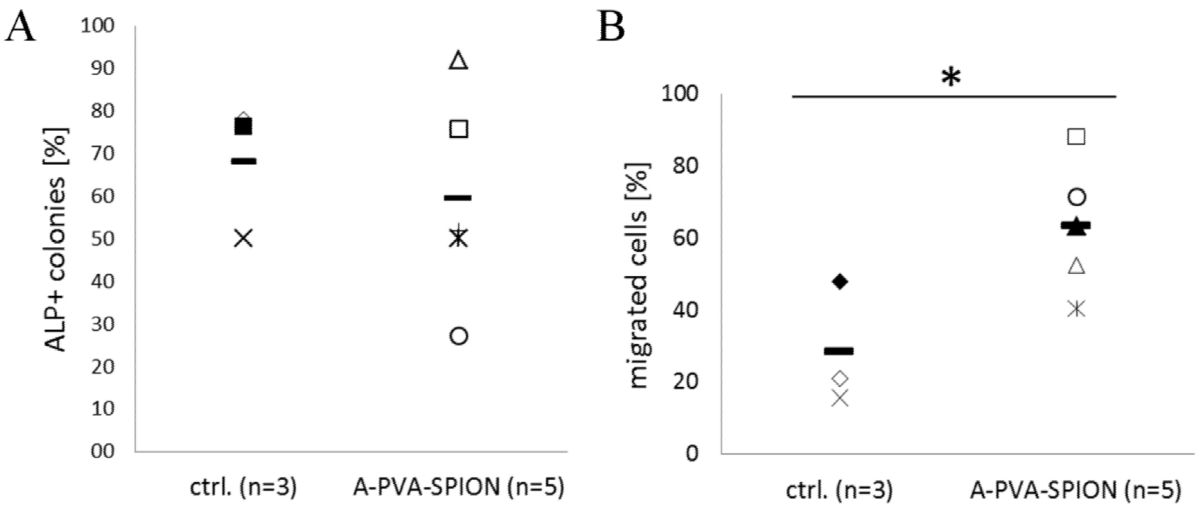

Figure 21 Function of A-PVA-SPION exposed rMSCs.

(A) The rMSCs osteogenic potential remains unaffected in response to *in vivo* exposure with A-PVA-SPION. (B) Although not detrimental, a significant increase in rMSC's migratory capacity was observed upon seven day *in vivo* exposure to A-PVA-SPIONs. Black bar represents mean, symbols represent the same individual animal in each graph. (Student's ttest, two-sided, paired, * indicates $p < 0.05$)

3.3. Non-engineered *in situ* generated NPs: a result of MoM implant wear

3.3.1. Nanoscaled MoM wear accumulates in the periprosthetic region

To confirm the exposure of local hMSCs with MNPs from MoM wear, periprosthetic tissue was harvested and wear debris was isolated. The periprosthetic tissue from MoM patients showed signs of metallosis as indicated by dark color toned regions and macroscopic wear debris (**Figure 22 A**). Metallic wear debris was isolated from tissue samples of every MoM patient in different quantities (**Figure 22 B**). The isolated MoM wear particles from MoM patient #4 were then visualized using TEM (**Figure 22 C**). The wear particles were indeed nanoscaled and heterogeneous in size and shape with a mean diameter of 34.7 ± 16.2 nm and 84% of round-, 11% oval- and 5% needle-shaped particles (n=64). Micron- and millimetre sized debris was also observed but could not be analysed with this technique (TEM). The presence of nanoscaled MoM wear and therefore the *in vivo* exposure of MoM-MSCs were thus confirmed.

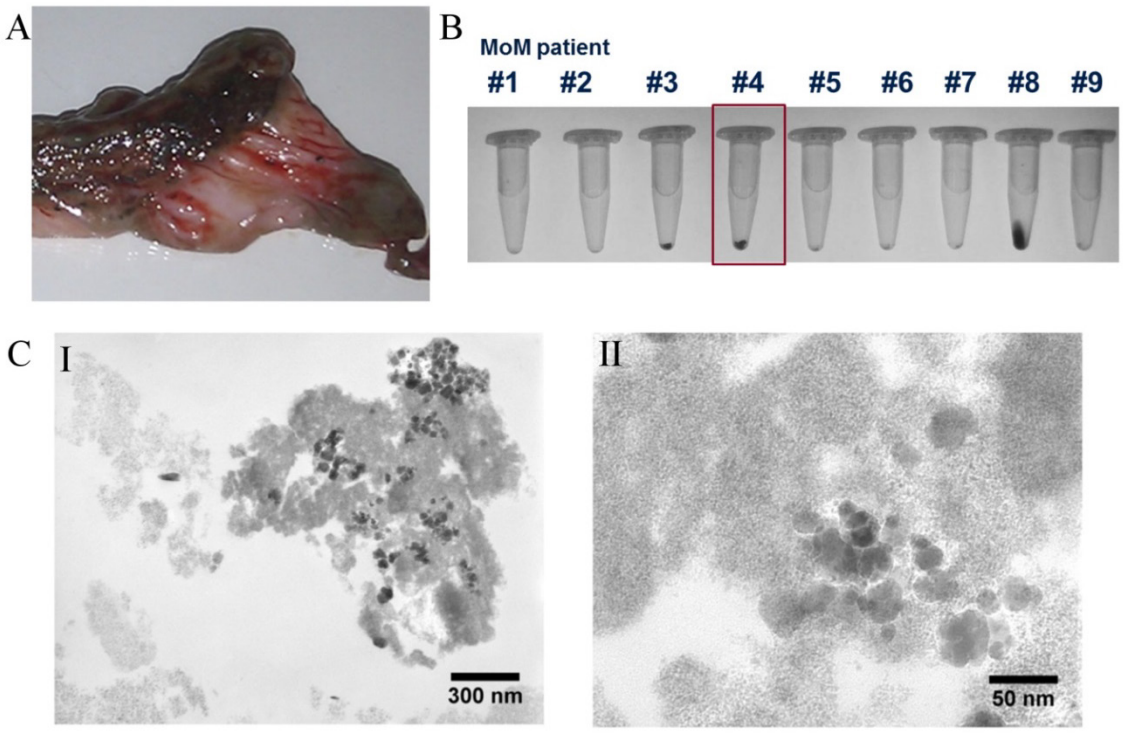

Figure 22. Periprosthtetic tissue contains nanoscaled wear debris.

(A) Shown is periprostetic tissue that exhibits signs of metallosis. (B) Metallic wear debris was isolated from n=9 patients in different quantities. (C) TEM micrographs show metallic wear particles that were isolated from periprosthetic tissue of MoM-patient #4.

3.3.2. hMSCs but not hOBs osteogenic function is altered by exposure to MNPs

After the exposure with nanoscaled MoM wear *in vivo* was confirmed, the viability, proliferation and regenerative functions of MoM-OBs and MoM-MSCs were assessed *in vitro*. Proliferation, viability and their ability to generate mineralized matrix were not altered significantly for MoM-OBs when compared to their respective controls (**Figure 23**). MoM-MSCs showed no significant differences in metabolic activity or proliferation when compared to their respective controls (**Figure 24**). Following this, the MoM-MSCs and their respective controls were characterized for their regenerative key features: migration and their potential to differentiate into the adipogenic, chondrogenic and osteogenic lineage. In contrast to the MoM-OBs, all MoM-MSCs failed to acquire the osteogenic phenotype and subsequently generate mineralized matrix (**Figure 25 D**). Interestingly, the MoM-MSCs migration, adipogenesis and chondrogenesis remained unaffected *in vitro* (**Figure 25**). Osteogenic differentiation, i.e. the process whereby an undifferentiated MSC acquires the features of an osteoblast, was quantified by the amount of mineralized matrix generated. Since the enzyme ALP is crucial for the process of matrix mineralization, the ALP activity of MoM-MSCs and their respective controls before and after subjecting the cells to osteogenic differentiation media was assessed. The MoM-MSCs ALP baseline activity was significantly reduced when compared to their respective controls (**Figure 26 A**). When incubated with osteogenic media for five days, the MoM-MSCs ALP activity significantly reduced when compared to the control-MSCs' ALP activity (**Figure 26 B**).

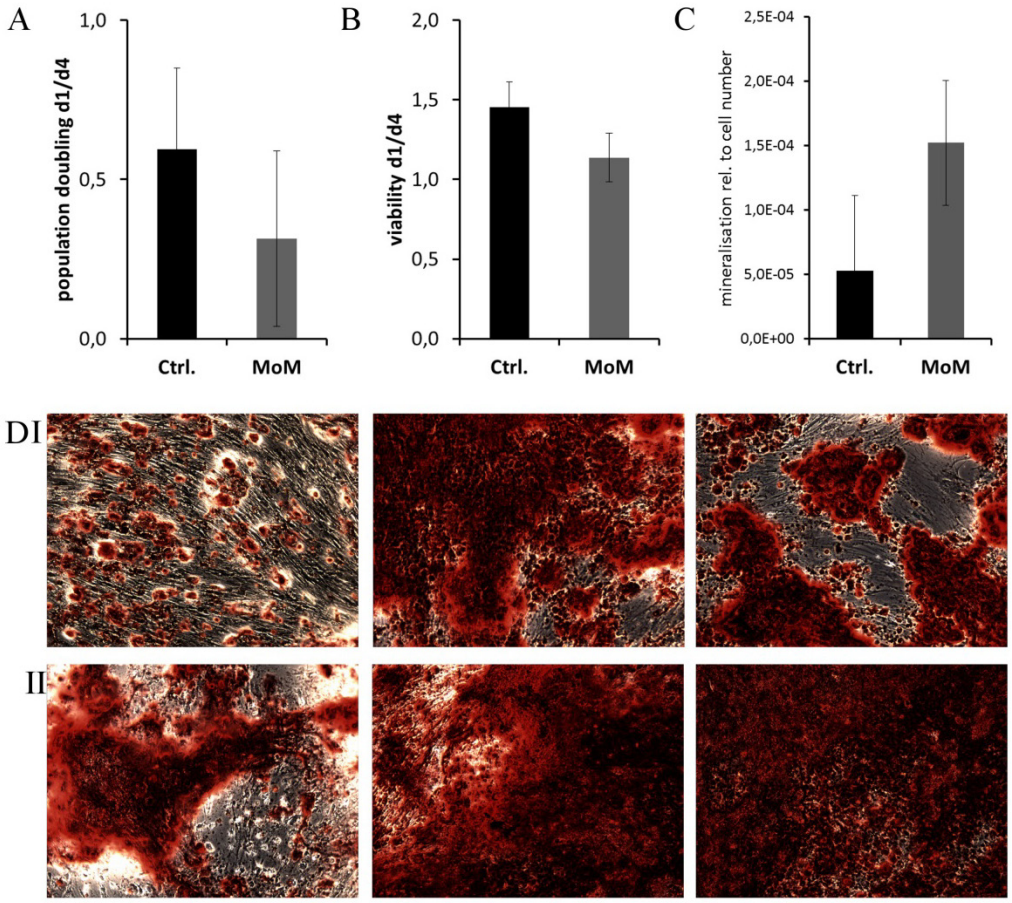

Figure 23. Viability and matrix mineralization of MoM-OBs.

(A, B) Proliferation and viability were determined at day 1 and day 4. (C+D) Matrix mineralization was assessed quantitatively and qualitatively by Alizarin Red staining. For (D I) control-OBs and (D II) MoM-OBs. (mean ± SD, n=3, unpaired Student's t-test)

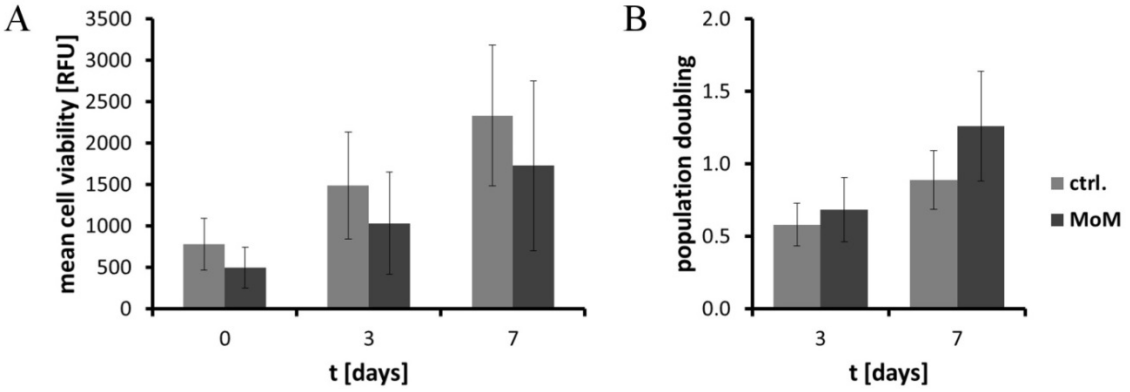

Figure 24. Viability and proliferation of MoM-MSCs *in vitro*.

(A, B) Metabolic activity and proliferation were determined at day 0, 3 and 7 without significant differences between the MoM-MSCs and their respective controls. (mean ± SD, n=5, unpaired Student's t-test)

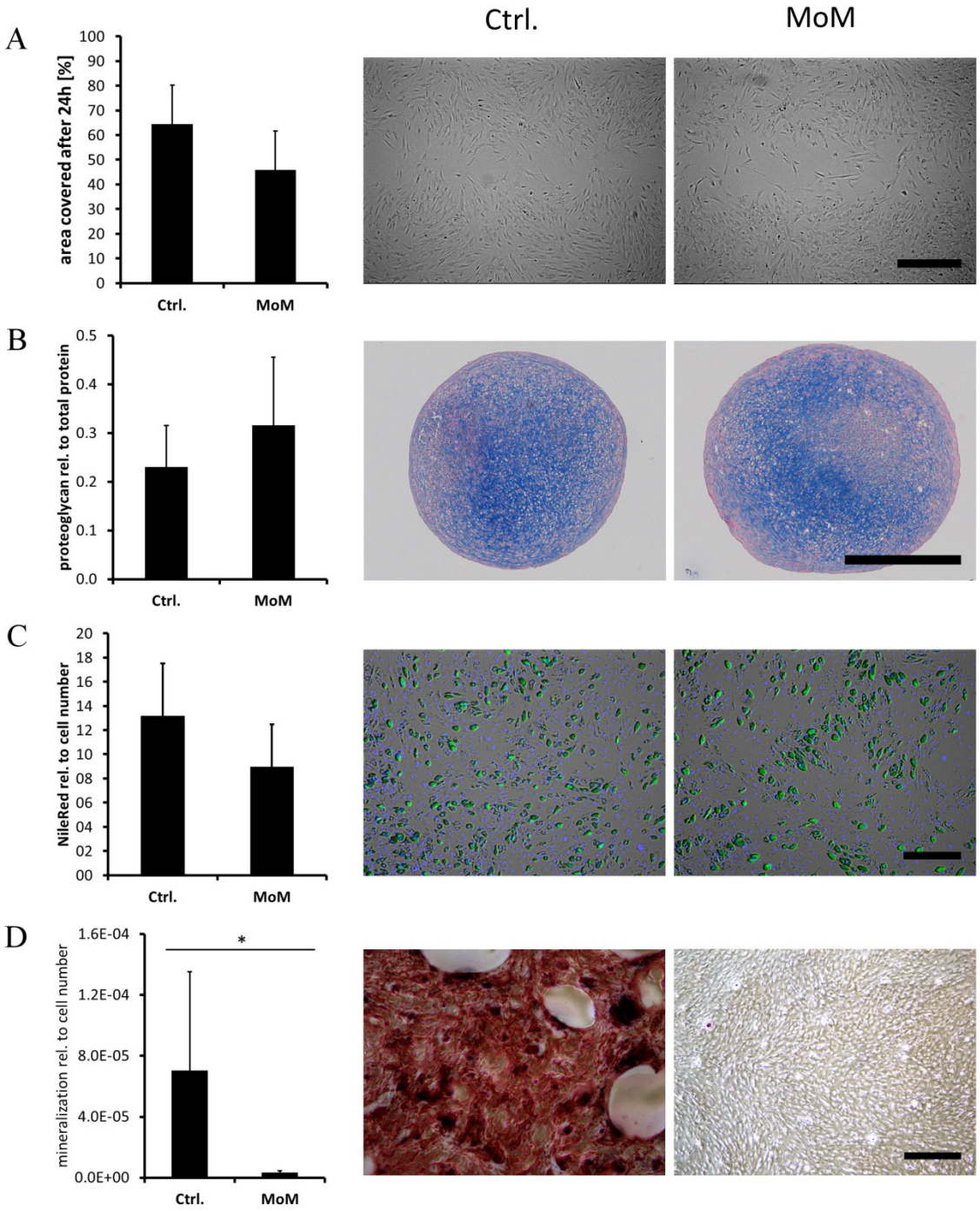

Figure 25. MoM-MSC regenerative key functions *in vitro.*

MoM-MSCs and their respective controls were investigated for their regenerative functions (A) migration was assessed quantitatively by 24h scratch assay , (B) chondrogenic differentiation was assessed qualitatively by alcian blue staining and quantitatively by colorimetric proteoglycan assay, (C) adipogenic differentiation was assessed quantitatively by Nile Red and DAPI staining and (D) osteogenic differentiation was assessed quantitatively by Alizarin Red staining. Among those cellular functions, osteogenic differentiation was found to be significantly impaired for MoM-MSCs. (mean ± SD, n=5, unpaired Student's t-test, * indicates $p \leq 0.05$)

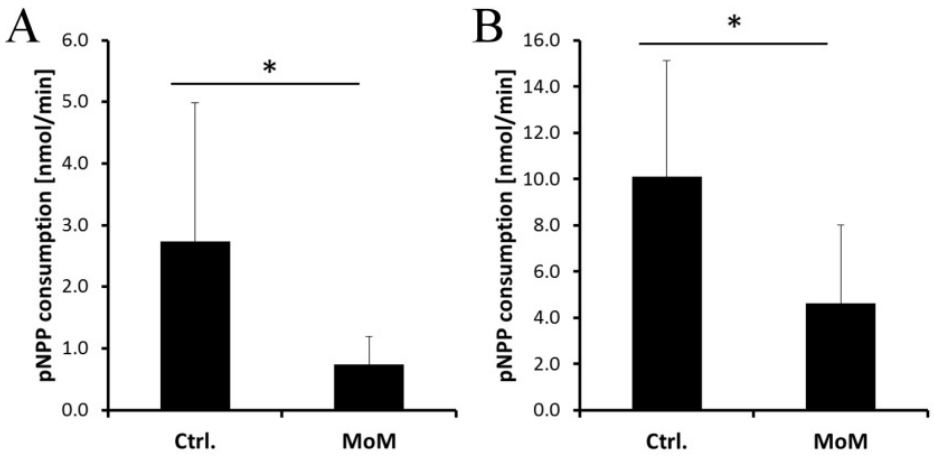

Figure 26. ALP activity *in vitro* and *in vivo*.

MoM-MSCs and their respective controls were investigated for their ALP activity (A) before and (B) after being subjected to osteogenic differentiation media *in vitro*. (A, B) ALP activity was significantly impaired for MoM-MSCs *in vitro.* (n=8, mean ± SD, unpaired T-test, * indicates $p < 0.05$)

4. Discussion

4.1. A-PVA-SPIONs: a nanoscaled tool for diagnosis and therapy in bone

The overall goal of this part is to draw a well-funded conclusion about the effect of A-PVA-SPIONs on MSCs thereby allowing a risk assessment of the A-PVA-SPIONs use for cell labeling and MRI contrast enhancement in bone marrow. One aim of this study was to develop an efficient labeling procedure for hMSCs with A-PVA-SPIONs and avoid detrimental secondary effects on the cells viability and functions. After establishing a labeling procedure that meets these requirements, the feasibility of visualizing A-PVA-SPION-labeled MSCs in MRI was verified. Another aim was to evaluate A-PVA-SPIONs for their suitability to facilitate MRI contrast enhancement in bone marrow and the consequences of their accumulation for local stromal cells including MSCs. Both applications make use of the A-PVA-SPIONs magnetic properties for visualization in MRI; they do however fundamentally differ in terms of the exposure scenario needed to facilitate the corresponding approach. For labeling MSCs, direct exposure to A-PVA-SPIONs and their subsequent internalization *in vitro* is a prerequisite for later visualization *in vivo*. Using A-PVA-SPIONs for contrast enhancement requires their accumulation in the tissue of interest but not necessarily their internalization by non-phagozytotic local cells such as MSCs. Thus, two different exposure scenarios were investigated according to the needs of the respective application.

4.1.1. A-PVA-SPIONs for hMSC labeling

When using A-PVA-SPIONs as a cell labeling probe, their internalization is of paramount importance. Evidence of the internalization of A-PVA-SPIONs by hMSCs and their subcellular location *in vitro* was provided by both TEM and TXM approaches that allow for resolution in the nanometer scale. The advantages of the TXM approach over methods used in other studies are artifact-free sample preparation of the MSCs, visualization in the nanometer range and 3D spatial information, i.e. conclusive evidence of cellular internalization. The TEM approach showed A-PVA-SPIONs as high contrast particles that accumulate in intracellular vesicles. The TXM data confirmed this result, but also demonstrated that smaller high contrast spheres and irregular shaped clusters can be found. The size of these small high contrast spheres analyzed by TXM is similar to the size of A-PVA-SPIONs in DMEM + FCS determined by PCS (TXM: 52.9 ±9 nm vs. PCS: 45 ± 2nm). It can be thus assumed that single

A-PVA-SPIONs are either internalized individually or are a result of endosomal escapes. So far, it cannot be distinguished whether the single A-PVA-SPIONs are either vesicle-bound or freely dispersed in the cytosol. Vesicle-bound single particles would indicate that A-PVA-SPIONs enter via a typical endocytosis-exocytosis route by being internalized as individual NPs and further sorted into bigger vesicles like lyso- or exosomes.[242] Freely intracellular dispersed A-PVA-SPIONs could directly interact with constituents of the cytosol, i.e. proteins, mRNA, and cellular organelles, which may be other avenues of A-PVA-SPION-induced functional changes. However, further research is needed to provide conclusive evidence for one of those assumptions. The data from *in vitro* exposure experiments shows clearly that with administered dose of 50 µgFe/ml iron and 24h incubation a near saturation of the cells with NPs was achieved. A similar saturation pattern was observed for an incubation time of 4h, although the cellular doses achieved were lower. Interestingly, this saturation pattern cannot be compensated by a higher administered dose if the threshold value of 50 µgFe/ml is exceeded. These observations indicate that an active uptake mechanism (i.e. endocytosis) is responsible for the internalization of A-PVA-SPIONs in hMSC. Similar results that support an active uptake mechanism were already observed for the internalization of PVA-SPIONs by non-phagocytic cell lines.[213, 217, 243]

After labeling, the cells were subjected to the different *in vitro* assays to examine of A-PVA-SPION internalization on the hMSCs biology. For MRI based tracking approaches *in vivo*, it is important that those A-PVA-SPIONs are not only non-toxic, but also do not interfere with the cells' regenerative functions. Therefore, proliferation and multi-lineage differentiation were investigated as they are both key functions of MSCs as defined by The International Society for Cellular Therapy (ISCT).[46] There were no signs of A-PVA-SPION-induced toxicity observed for labeled hMSCs, as proliferation and mitochondrial activity remained unchanged similar to results observed for other cells.[214, 217] Next, the MSCs' ability to differentiate into the adipogenic, osteogenic and chondrogenic lineage was investigated and was found to be unchanged. These positive results are noteworthy since a number of studies reported impaired chondrogenesis after SPION-application.[195, 196, 201, 243] Only two of these publications report the corresponding cellular doses that were higher than the one determined in our study; 25.7 ± 0.96 pg_{Fe}/cell and 13 – 16 pg_{Fe}/cell.[196, 201] The impairment of chondrogenesis in these studies might thus be caused by a high intracellular iron load as already hypothesized.[195, 201] Hence, it can be assumed that the cellular dose of 8.2 ± 3.6 pg/cell as determined in this work is below a critical threshold that leads to impaired chondrogenesis. A number of *in vivo* studies provide evidence that exogenously

delivered MSCs migrate and target specific tissues via an active mechanism. For example, when injected into femurs MSCs were later detected in the contralateral bone or MSCs implanted into the tibial bone marrow cavity were detected in the callus of the ulnar fracture site after three weeks.[244, 245] Three days after injection into the tail-vein MSCs were detected at the fracture site.[61] Interestingly, migration of hMSCs is increased after labeling with A-PVA-SPIONs. A subsequent migration experiment revealed that this increase in migration seems not to be mediated by the A-PVA-SPIONs components (ferrous ions and PVA) but rather by the intact NP. Quantitative analysis of mRNA in labeled and non-labeled hMSCs after migration showed that the expression was up-regulated for EGF and down-regulated for VEGF-A in A-PVA-SPION labeled cells. Both growth factors have been shown to stimulate migration in MSCs.[246, 247] In addition, it is known that the endothelial growth factor receptor (EGFR) is internalized through clathrin-mediated endocytosis upon binding to its ligand EGF. This mechanism is believed to regulate EGFR mediated signaling.[248] The expression of EGF might be a sign of self-stimulatory up-regulation of NP endocytosis by increasing the number of clathrin coated pits that were formed in response to the EGR-EGFR complex. The dosimetry data obtained in this work supports an active mechanism for the A-PVA-SPIONs internalization. Since active endocytosis mechanisms require reorganization of the cytoskeletons actin-fibers, an up-regulation in energy dependent endocytosis would also have an effect on cell motility. In that regard, the down-regulation of VEGF-A and the downstream targets in cell migration PTK2 and ROCK1 might reflect the cells counteraction to the increase in migration caused by the EGF dependent up-regulation in endocytosis activity. The hypothesis that the increase in migration is a by-product of an up regulated endocytosis would however need further experimental proof by investigating if clathrin mediated endocytosis is indeed the main uptake mechanism for A-PVA-SPIONs. Additionally, the mRNA expression data would need conformation through expression analysis on the protein level. This effect on migration could be advantageous in the context of cell-based therapies as exogenously delivered MSCs might migrate better *in vivo*. On the other hand, this effect could also be disadvantageous as it indicates cellular changes induced by A-PVA-SPIONs internalization that could influence so-far unknown parameters beyond migration. Future work would be required to determine if the change in migration upon A-PVA-SPION-labeling has consequences for the outcome of regenerative MSC-based therapies.

The use of MRI phantoms demonstrated that visualization of A-PVA-SPION labeled hMSCs *in vitro* is feasible. Collaborative work with colleagues from the University of Geneva revealed that visualization of labeled cells can also be achieved *in vivo* after local injection of A-PVA-SPION labeled hMSCs in the knee joint of rats.[230] Here, A-PVA-SPION labeled and non-labeled hMSCs (control) were locally injected into the right naïve knee joint of Lewis rats. After 24 hours, A-PVA-SPION induced signal loss was detectable on T1 weighted (VIBE) MR images as a black region superior and anterior to the lower section of the femur (**Figure 27 A I, III**). No signal could be seen at the region on VIBE MR images of the left knee joint where non-labeled MSCs were injected (**Figure 27 B I and III**). In the corresponding dUTE MR images the A-PVA-SPION-labeled MSCs generated positive MR enhancement and can be seen as a white region at the same position while no contrast was seen in non-labeled controls (**Figure 27 A II, IV and 21 B II, IV**). In addition to these MRI findings, post mortem histology of the animal's knee joints confirmed the presence of A-PVA-SPION labeled MSCs (**Figure 27 C**). In conclusion, A-PVA-SPIONs can be used as probes for direct hMSC labeling, while their influence on the hMSCs migration needs to be considered when this function is crucial for the outcome of respective regenerative approaches.

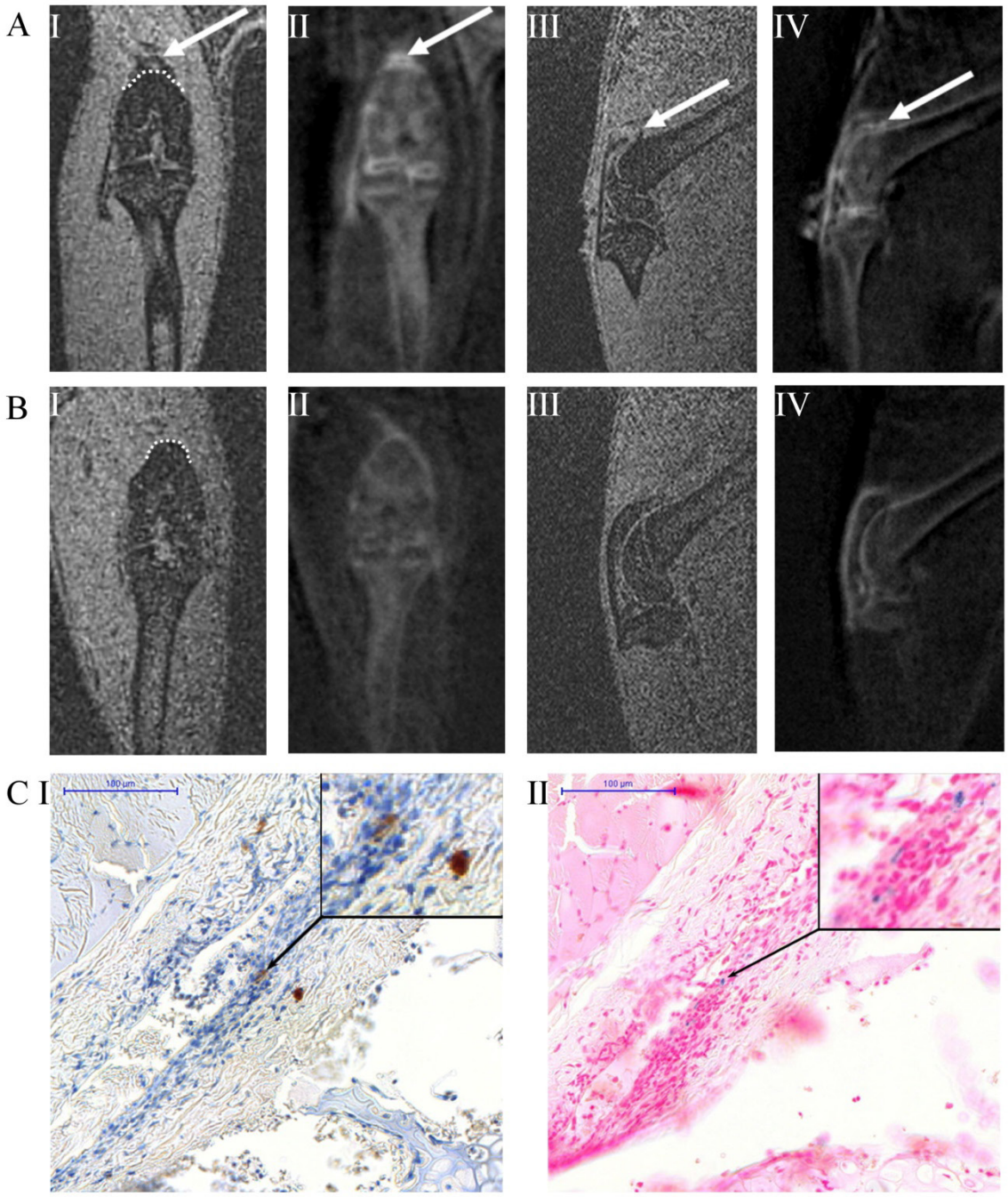

Figure 27. MRI and histology on rat knees injected with A-PVA-SPION labeled hMSCs.

(A) Coronal (I, II) and sagittal (III, IV) views of rat knee joint injected with A-PVA-SPION labeled hMSCs and scanned *in vivo*. (C) Coronal (I, II) and sagittal (III, IV) views of rat knee joint injected with non-labeled hMSCs and scanned *in vivo*. White arrow: A-PVA-SPION labeled hMSCs (dotted white line indicates contour of the femoral diaphysis). (B) Shown are micrographs of (I) a paraffin section immunostained using anti human-CD44 antibody as a marker for hMSCs and (II) a consecutive paraffin section stained using Prussian blue to detect A-PVA-SPION clusters. (adapted from [230])

4.1.2. A-PVA-SPIONs for contrast enhancement in bone marrow

In this part of the thesis work, the systemic administration of A-PVA-SPIONs leads to their accumulation in the bone marrow as demonstrated by the increase of iron levels in the bone marrow of A-PVA-SPION injected animals. The accumulation of A-PVA-SPIONs was confirmed by additional work from collaborative researchers from the University of Geneva.[236] Here, the presence of A-PVA-SPIONs in bone marrow was demonstrated by a clear negative contrast enhancement in MRI of the tibia of the lower limbs 24 hours and 7 days after injection. Such negative contrast was absent prior to injection (**Figure 28 A and B**). Furthermore, semi-quantitative analysis of the MRI data revealed a statistical significant change of the normalized signal after 24h ($p < 0.001$) and seven days ($p < 0.001$) post-injection for the A-PVA-SPION injected animals only (**Figure 28 C**). There was a significant ($p < 0.01$) but small decrease in the MRI signal intensity of 8.6% between 24h and 7 days for the A-PVA-SPION injected group. The accumulation of A-PVA-SPIONs in bone marrow was further confirmed by histology which revealed Prussian blue positive deposits within the bone marrow of A-PVA-SPION injected animals that are absent in the respective controls (**Figure 28 E**). Accumulation of A-PVA-SPIONs in the bone marrow and subsequent 7 day exposure of local BMSCs was thus confirmed through qualitative and quantitative methods.

The data thus confirms the hypothesis that A-PVA-SPIONs accumulate in bone marrow, while the events that lead to this accumulation remain unknown. It is reported, that the A-PVA-SPIONs' physiochemical properties such as size and surface charge change in response to physiological pH and the presence of proteins.[230] Future studies that aim to draw conclusions on the A-PVA-SPIONs accumulation in bone marrow should thus consider characterizing them not only in their solvent but also after they have been introduced to animal blood. The observed signal decay of 8.6% within 6 days indicates a rather slow elimination of A-PVA-SPIONs from the bone marrow. This could prove advantageous for theranostic applications such as long-term drug delivery or monitoring of bone turnover over time. However, to gain a better understanding on the level of exposure beyond a seven day period, future investigations should determine how long the A-PVA-SPIONs reside in bone marrow before they are eliminated completely.

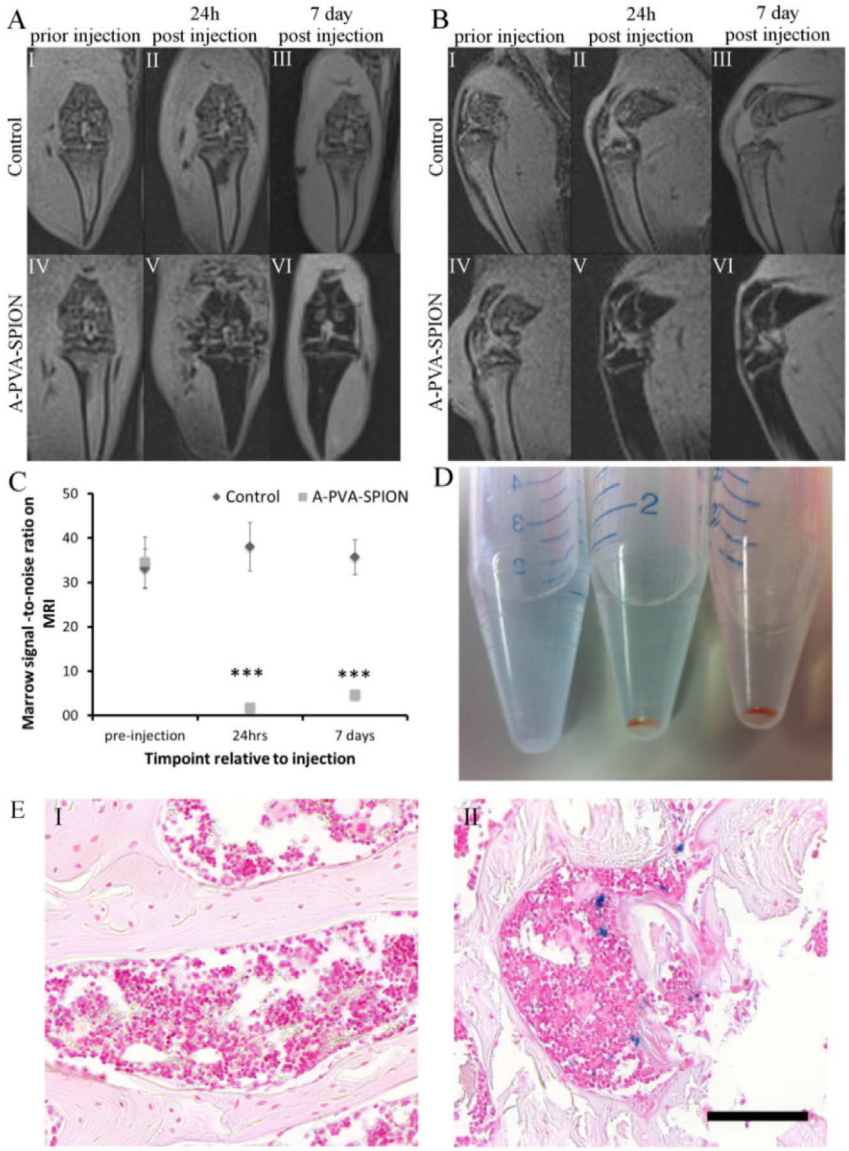

Figure 28. Systemic injected A-PVA-SPIONs accumulate in bone marrow.

(A) Coronal and (B) sagittal sections of rat knee joints are shown (I + IV) prior to injection of A-PVA-SPIONs, (II + V) 24h and (III + VI) 7 days after injection. A clear hypointense signal is observed in the marrow of the tibia in the A-PVA-SPION injected animals on MRI at 24 hours and after 7 days (A + B, V + VI) that is absent in the corresponding controls without A-PVA-SPION injection (A + B, II + III). (C) Analysis of the MRI signal intensity over time for the normalized MRI signal (n=4, mean ± SD, the presented significance levels refer to 24h and 7 days relative to pre-injection, *** indicates $p < 0.001$). (D) Shown are the magnetic fractions after magnetic separation of bone marrow; left: control; middle and right: A-PVA-SPION-injected. (C) The presence of A-PVA-SPIONs was confirmed by histological Prussian blue staining and representative images are shown for (D I) control and (D II) A-PVA-SPION injected animals. Scale bar = 100µm. (© Futuremedicine (Lond) [236])

The next aim was to investigate the consequences of *in vivo* exposure with A-PVA-SPION to the rMSCs biology. In this part of the thesis, the A-PVA-SPIONs suitability for contrast enhancement in bone marrow was investigated which does not necessarily rely on cellular internalization by rMSCs. Thus, only the A-PVA-SPIONs accumulation in bone marrow but not their potential for cellular internalization *in vivo* was investigated. The presence of A-PVA-SPIONs in the animal's bone marrow is not treated as an indicator for cellular internalization but rather as a proof for *in vivo* exposure of local rMSCs. It was found that the presence of A-PVA-SPIONs did not impair the rMSCs proliferation, viability and cellular function. However, *in vivo* exposure of rMSCs with A-PVA-SPIONs was accompanied by a significant increase of the cells metabolic activity. A fluometric resazurin-based assay was used for determining the cells metabolic activity as a measure for their viability.[249] The intracellular reduction of resazurin to resofurin is facilitated by mitochondrial, microsomal and cytosolic oxidoreductases.[250] Thus, an increase in oxidoreductase activity in A-PVA-SPION exposed BMSCs can be assumed, while the underlying mechanism for this alteration has not been investigated. Oxidoreductases are not only involved in the cellular energy metabolism but have also been implicated in other intracellular processes such as detoxification or regulation of the cellular redox potential.[251, 252] The interpretation of the increased oxidoreductase levels as solely an increase in cell viability would be therefore misleading. On a functional level, the rMSCs' migration rate is significantly increased for cells exposed to A-PVA-SPIONs when compared to their controls. Similar to the increase in metabolic activity, the increase of an important regenerative function does not necessarily reflect a positive enhancement. The alterations in the cells energy metabolism and migration rate should rather be regarded as clear indicators of a cellular response to the presence of A-PVA-SPIONs that could comprise unknown parameters beyond those investigated. Future work should therefore address the increase in oxidoreductase activity and migration and try to identify possible crosstalk in the underlying mechanisms. For a better risk assessment, it would not only be necessary to investigate how long the A-PVA-SPIONs reside in bone marrow, but also if the observed effects are transient or persistent.

There are numerous examples in literature where the effect of SPIONs on MSCs was investigated *in vitro*. To date, this study is the first one using an *ex vivo* approach to address this question. *In vitro* assays are considered to be cost and time effective and are therefore used in the majority of studies when nanoparticle toxicity is assessed. [253] However, several problems arise when the outcome of *in vitro* studies are meant to have relevance to the actual *in vivo* situation. This holds especially true for the dosage, as applied doses *in vitro* might not

necessarily reflect actual *in vivo* exposure.[254] Therefore, it was recently proposed to determine cellular doses *in vivo* for proper comparison with *in vitro* experiments.[255] For a comprehensive description of the *in vitro* dosimetry, it was proposed to report the administered, delivered and cellular dose.[164, 165] The administered dose defines the amount of nanoparticles that is employed at the beginning of the experiment while the delivered dose gives information about the amount of nanoparticles that reaches the cell monolayer after a given time. The effective or target cell dose describes the amount of internalized nanoparticles per cell. In analogy to this *in vitro* dosimetry, the dosage in this study can be described by the administered dose of 0.035 mg_{Fe}/g (7 mg_{Fe} total) intravenous injected A-PVA-SPIONs and a delivered dose of 10.4 and 11.1 $\mu g_{Fe}/mg_{BM}$ at day seven determined by ICP-OES of the magnetic sorted fractions. It should be noted that the A-PVA-SPIONs could be partly degraded after seven days and that the magnetic sorting procedure does only capture intact A-PVA-SPIONs that behave superparamagnetic. However, the rather small MRI signal decay observed within six days, indicates that the A-PVA-SPIONs are slowly degraded and/or excreted. Assuming that the A-PVA-SPIONs are equally distributed within the bone marrow, the estimated cellular dose can be calculated using the delivered dose and the number of cells in the bone marrow. According to literature the bone marrow of two month old rats contains $2.8x10^5$ cells/mg_{BM}.[256] Thus, the estimated cellular doses in the A-PVA-SPION injected animals are 4.0 and 3.7 pg_{Fe}/cell. These values are however strictly theoretical as they I) assume an even distribution of the A-PVA-SPIONs within the bone marrow and II) indicate cellular uptake. Since we did not provided experimental evidence for the A-PVA-SPIONs distribution pattern and cellular uptake the discussed cellular dose can only serve as an estimate rather than an existing value. Nevertheless, these estimated cellular doses are in the same order of magnitudes that are usually reported for cellular doses in SPION toxicity studies on MSCs *in vitro,* including those determined for A-PVA-SPION labeled hMSCs in this work.[208, 209, 230, 257] Although the *in vivo* cellular dose is strictly theoretical as it assumes an even distribution of A-PVA-SPIONs in the bone marrow, it shows that the gap concerning dosage between the current *ex vivo* work and previous *in vitro* studies is minimal.

Nanoparticles might acquire toxicity as they undergo changes as a function of their environment.[160, 162] Furthermore, nanoparticle toxicity could occur due to secreted chemokines as reported in two different co-culture models of lung alveolar cells.[172, 173] The approach of *in vivo* exposure followed by *in vitro* experiments addresses these aspects in

a way similar to a black box were only the input (amount of injected A-PVA-SPIONs, animal survival time) and the output (A-PVA-SPION exposure of bone marrow, viability and function of rMSCs *in vitro*) are known whereas the internal workings *in vivo* (physiochemical changes, mechanisms of bio-distribution, cellular uptake, cell mediated effects) remain unknown. This allows the establishment of transfer characteristics (dose-response relationship) between input and output of the black box system without precise knowledge of the internal workings. The approach described in this study thus represents an elegant model when the complex *in vivo* effect of distinct nanoparticles on a certain cell type needs to be determined. However, the high inter-individual variety of obtained data in the current work might cover small biological effects that do not reach significance at the sample number employed. It is therefore suggested, that future studies which use a similar approach would need to be performed in larger cohorts. In conclusion, A-PVA-SPIONs have the potential to accumulate in bone marrow and can facilitate MRI contrast enhancement while an effect on the local rMSCs biology was observed that indicates the necessity for further research.

4.2. MoM implant wear: a nanoscaled clinical problem

In this part of the presented thesis work, the influence of MoM wear on the biology of local hMSCs was investigated. The exposure of local cells to CoCrMo alloy wear from MoM implants was confirmed through the isolation of metallic wear debris from periprosthetic tissue. The wear particles were analyzed for their size in shape by TEM and found to be nanoscaled. Metallic wear debris was isolated from every sample in different quantities indicating that the cells from all donors were exposed to MoM-MNPs in varying amounts. This exposure had no significant effects on the MoM-OBs biology, while the potential to differentiate towards the osteogenic lineage was clearly impaired for MoM-MSCs *in vitro*, indicating long-term effects on the MoM-MSCs but not MoM-OBs. Given that MSCs account for only 0.01% of the total cell population in bone marrow, the effect on the number of functional OBs generated by these osteoprogenitor cells might be much more severe than an effect on matured OBs alone.[45] It was thus decided to focus further investigations on the MSCs rather than on their progeny the OBs. In addition to the MoM-MSCs osteogenic differentiation potential, their ALP expression found impaired when compared to their controls. The data from ALP activity in context with the inhibited osteogenic differentiation indicate that the effect of MoM wear on MSCs seems to be specific for their bone forming function but not their other regenerative functions such as adipogenic and chondrogenic differentiation or migration. This work therefore represents an important piece in the puzzle of the genesis of periprosthetic osteolysis: the exposure to MoM-wear is accompanied by increases in osteoclast generation and activity, while the bone forming function of MSCs is impaired. In summary, wear from MoM endoprostheses seems to generate a worst case scenario in which the tissue homeostasis of bone is heavily shifted towards bone resorption.

In this context, it is also noteworthy that the inhibition of MoM-MSCs' osteogenic differentiation and ALP activity *in vitro* were examined after the cells had been isolated from bone marrow and kept in cell culture for six to eight weeks. Although the toxin under suspicion, MoM-implant wear, had been withdrawn for weeks, the effects of exposure were still detectable. This indicates that the exposure with MoM-wear leads to long-term effects that are persistent under standard cell culture conditions within the time frame of at least eight weeks. Thus, additional *in vivo* animal experiments would be of value to determine if the loss of osteogenic potential is either a persistent or transient effect. This is of clinical relevance as it would guide the surgeon's decision on whether implant revision and resection of periprosthetic tissue are sufficient to restore tissue homeostasis in bone or if additional

procedures are required. These could encompass medication that aim to reduce the amount of soluble Co and Cr such as the administration of chelating agents similar to the treatment of severe heavy metal intoxications.

Although the effects of MoM-wear exposure where clearly manifested in terms of a strongly reduced osteogenic differentiation potential in MoM-MSCs, it is unclear if this effect is mediated by the MoM-wear MNPs themselves or by their dissolution products. It is widely accepted that wear particles in general accumulate in the periprosthetic tissue.[223] In a recent study, it was shown that MoM-wear MNPs are phagocytized by local macrophages and further degraded into dissociated Co and Cr.[221] In addition, several studies report extensive amounts of Co and Cr in their dissociated state in either periprosthetic tissue or synovial fluid while the exposure of bone marrow was, to the authors knowledge, investigated only once.[221, 258-263]

It was thus decided to investigate the exposure with particulate and dissociated Co and Cr, which was carried out in a master thesis related to the current work. Here, the author acted as second supervisor. The key findings of this master thesis will be briefly summarized as they contribute to the understanding how MoM-wear influences local hMSCs. In this master thesis, the exposure to Co and Cr of different compartments in the periprosthetic region was investigated: periprosthetic tissue, synovial fluid and bone marrow. This data gave a comprehensive overview concerning the local exposure with Co and Cr in the periprosthetic region and also discriminated between total and dissociated Co and Cr. It was reported that the highest amounts of total and dissociated Co and Cr within the periprosthetic compartments were found in the periprosthetic tissue.[264] This is an important observation, as it clearly shows that vast amounts of accumulated particulate wear from endoprostheses are degraded. Thereby the amount of soluble metal species that have a high mobility is increased. In terms of osteogenic differentiation of MSCs *in vitro*, similar observations were made in the course of the associated master thesis. Here, hMSCs from control donors were exposed to Co^{2+} and Cr^{3+} ions in cell culture with concentrations that were in the same range as those determined for the periprosthetic compartments of MoM-patients. The exposure to Co^{2+}, Cr^{3+} or both lead to an impaired osteogenic differentiation of hMSCs accompanied by a reduction in the cells' ALP activity indicating that both metal ions are responsible for the observed effects.[264] The data from the master thesis work resembles my own observations regarding the diminished osteogenic differentiation of hMSCs. Furthermore, this data emphasizes that dissociated Co

and Cr rather than MoM wear MNPs might be responsible for this functional change in MSCs.

Co is known to directly bind to the 1α and 2α subunit of hypoxia inducible factor (HIF) with a high affinity and stabilizes this transcription factor, thus mimicking hypoxia by activation of the HIF pathway. It was shown that both the incubation under hypoxic conditions and the addition of Co^{2+} specifically affect proteins needed for osteogenic differentiation in MSCs.[265, 266] In these studies a decreased ALP mRNA expression, a decreased ALP activity, and a subsequent reduced deposition of osteogenic matrix were observed. An inhibition of ALP activity by Co^{2+} was also shown for other cell types including osteoblast cell lines. [267] Cr^{3+} has been shown to bind macromolecules with high affinity.[268] Since Cr^{3+} is not membrane permeable, an interaction of Cr^{3+} with components of the extracellular matrix is likely. Another explanation for the inhibition of matrix mineralization might be that Cr^{3+} can form complexes with negatively charged phosphate groups, resulting in the formation of chrome-orthophosphate ($CrPO_4$) which is also often found in periprosthetic tissue and fluid.[221] The abundance of Cr^{3+} from implant wear and corrosion might reduce the amounts of unbound phosphates needed for matrix mineralization within the periprosthetic region. In summary, wear from MoM endoprostheses contains MNPs and dissociated Co and Cr. It seems that not the MNPs themselves but their degradation products disturb tissue homeostasis of bone towards bone resorption by impairing the osteogenic potential of local MSCs.

4.3. Experiences with toxicity of engineered and non-engineered nanoparticles

Given the properties of nanomaterials especially NPs it is reasonable to expect an effect on biological systems such as cells. For example a high surface to volume ratio and quantum confinement effects might lead to unexpected consequences for a cells viability or function. However, the question remains of what nature changes in the cells biology would be and if an intrinsic toxicity exist that all NPs or at least those from the same classification such as metallic NPs, would share. In this study, two different types of MNPs were examined towards their effect on MSCs: engineered A-PVA-SPIONs and non-engineered MoM wear MNPs.

As expected, both NPs do provoke biological reactions by MSCs although the nature of these effects is very different. Here, one very important observation is that the exposure with the two NPs did not result in diminished proliferation or viability but always changed a functional aspect of the MSCs. In this regard, the definition of NP toxicity needs reconsideration since classic approaches to determine toxicity aim for the cells ability to proliferate and its viability while function is often not considered.[105] The functional changes induced by A-PVA-SPIONs, although relevant, did not qualify for toxicity as they do not impair the MSCs function in the respective context and might be very likely a byproduct of their cellular processing. In contrast, the functional changes observed for MoM-wear MNPs can be indeed considered as toxic, since the impaired osteogenic differentiation potential has catastrophic consequences for the MSCs function in the context of bone formation and therefore also bone remodeling. The presence of MoM wear MNPs thus directly contributes to the generation of periprosthetic osteolysis and poses and unacceptable risk for the patients' well-being, an effect that very well qualifies for being described as toxic.

The differences in the observed effects on the MSCs' function are most likely caused by the differences in the material compositions and the pre- or absence of a coating. The A-PVA-SPIONs magnetite cores and their polymeric coating are both engineered towards minimizing the NPs toxicity since both of these features are meant to prevent degradation. In contrast, the non-engineered MoM wear MNPs do not possess such properties. Quite contrary, they seem to be rapidly degraded as data from literature indicate. The resulting release of free Co^{2+} and Cr^{3+} can negatively affect cells and tissues as already discussed. It should thus be considered to include the tendency for dissolution to the various physiochemical properties that define a NP's toxicity. As mentioned in the introduction, a similar pattern was observed for QDs.[269] In analogy to the differences that occur for the transition from the bulk to the nano-form, the transition from the nano-form into the dissociated state can be a source for toxicity.

4.4. Concluding remarks

For A-PVA-SPIONs, two different MRI-based applications were proposed in this study: the labeling of hMSCs and the use as a contrast agent, both requiring a specific exposure scenario. SPION-labeling in combination with MRI is still the most promising approach for *in vivo* visualization of exogenously delivered cells and has gained high interest in cell-based therapies using MSCs. In the current study, the physiochemical properties of A-PVA-SPIONs were characterized, their interference with viability assays and their internalization by hMSCs was investigated, a correct dosimetry was formulated, no impact on MSC viability and differentiation but enhanced migration was found, and finally the proof of principle for MRI visualization of A-PVA-SPION-labeled MSCs *in vitro* and *in vivo* was provided. The current study thus provides comprehensive information about the impact of A-PVA-SPIONs on MSCs and the feasibility of MRI visualization. In summary, the A-PVA/PVA copolymer has proven to be a suitable SPION-coating for MSC labeling, i.e. the current data is in favor for the benefit of using A-PVA-SPIONs for hMSC labeling, yet some important parameters remain unknown. These parameters encompass the particles' long-term fate with respect to MRI visualization of A-PVA-SPION labeled MSCs. For example, the accuracy of MRI data *in vivo* is compromised by the inability to distinguish signals (1) from viable and dead cells, (2) from internalized and excreted SPIONs and (3) from SPIONs and MSCs engulfed by macrophages. Another concern is the A-PVA-SPIONs metabolism within the body that is determined by its stability *in vivo*. In regard of the problems that might arise with the NPs' dissolution, information about the A-PVA-SPIONs long term fate is crucial as toxicity might emerge much later as a result pf the NPs' degradation. Future work should therefore focus on research addressing 1) the A-PVA-SPIONs' retention time in the cell and elucidation of the involved endo- and exocytosis mechanisms and 2) whether the A-PVA-coating separates from the iron core resulting in renal excretion of A-PVA and integration of the SPION's iron in the body's iron metabolism. Taken together, these data help to develop A-PVA-SPION-based MRI-tracking of MSCs towards a reliable research tool where non-invasiveness, deep penetration, and high spatial resolution are needed. Thereby, it might be possible to gain further insight into the spatial and temporal distribution of transplanted MSCs in tissue repair and thus to optimize cell-based therapies. When used as a contrast enhancement agent in bone marrow, A-PVA-SPIONs should not exhibit negative influences on resident cells. In this work, it was clearly demonstrated that A-PVA-SPIONs accumulate in the bone marrow of animals following systemic administration and have thus high potential for contrast enhancement in bone marrow. However, it should be considered that the current data also

shows that A-PVA-SPIONs alter cellular reactions of rMSCs, specifically metabolic and migratory capacities. This data clearly shows that the mere presence of the A-PVA-SPIONs can alter the biology of local cells. This observation has direct implications for the application of A-PVA-SPIONs and other SPION formulations in bone marrow since their use should not have detrimental effects on local cells, this holds especially true for regenerative capacities of MSCs. Although not detrimental, the effects of *in vivo* exposure with A-PVA-SPIONs hint on cellular reactions that might encompass more parameters than investigated. The current set of data is thus not in favor nor against a benefit and indicates the need for additional work before conclusions about the actual risk benefit ratio can be drawn. Furthermore, the different result for *in vivo* and *in vitro* exposure with A-PVA-SPIONs indicate the need for a more thorough risk assessment of nanomaterials such as SPIONs that goes beyond classic *in vitro* approaches to rule out any risk possibly associated with their clinical use. The *in situ* generation and retention of nanoscaled MoM-wear particles was accompanied by an impaired osteogenic differentiation potential of local hMSCs. It is known from literature that Co and Cr are increases osteoclast generation and activity, while this study's data the shows that the bone forming functions of MSCs are impaired. In summary, wear from MoM endoprostheses seems to shift tissue homeostasis towards bone resorption. Consequently, this data add weight to the notion that the risks of MoM pairings exceed their benefits, especially for young patients. It can be further concluded that the broad use of CoCrMo in orthopedic implants, particularly in those with articulating surfaces, needs reconsideration since the generation of MoM wear NPs leads to an unacceptable risk that is a loss-of-function in local MSCs. In conclusion, identification of possible supplements for these alloys is urgently needed.

In this work the exposure to NPs, engineered and non-engineered, always had a detectable effect on MSCs. The exposure scenario can influence the nature of these effects as exemplified by the differences in cellular reaction between *in vitro* and *in vivo* exposure to A-PVA-SPIONs. Hence the exposure to NPs, may it be intentional for diagnostic purposes or unintentional through *in situ* generation, is always connected with a biological reaction and therefore also with possible risks to a person's health. For a risk assessment, it is thus of paramount importance to thoroughly characterize the effect of a given nanoparticle on the function of specific cells or tissues including the exact exposure scenario and possible dissolution of the NP. This information enables the establishment of a risk benefit ratio that is needed when the exposure to NPs needs to be justified. Furthermore, knowledge about the mechanisms behind the observed biological reactions will help to design and engineer NPs that do not provoke adverse effects on cells and tissues, thus minimizing the risk of their use.

5. Acknowledgements

I want to thank Prof. Georg N. Duda for giving me the possibility to work as a PhD student in the Julius Wolff Institute at the Charité Universitätsmedizin Berlin. I especially want to thank for the many unique opportunities that were given to me by Prof. Duda. Here, I especially want to mention: the collaborative work in the NanoDiaRa framework, the work on the BESSY II synchrotron, the close collaboration with the clinicians of the Charité that was the foundation for my work on MoM wear MNPs and the many travels to conferences and collaboration partners. Finally, I want to thank for the non-bureaucratic replacement of my beloved handbike after it was stolen during one of my official travels abroad.

I want to thank Prof. Roland Lauster for giving me professional and personal guidance throughout my studies: from the undergraduate to the PhD student, you always gave valuable advice and kept me reaching my goals.

I want Prof. Petra Knaus for being my mentor in the first two years of my PhD work and for valuable discussions on the project.

I want to thank Dr. Andrea Ode for having the courage of being my supervisor. I would need to lie if I would say I have learned nothing or just a bit. The opposite is the case and I am thankful that you focused on the things I needed to learn instead of teaching me what I already know. I also need to mention that I was impressed by the fairness and integrity on how my occasional bursts of criticism were treated.

I want to thank Dr. Sven Geissler, Dr. Anke Dienelt, Dr. Simon Reinke for supporting me in terms of fruitful scientific and non-scientific discussion. I especially want to thank Dr. Anke Dienelt for additional supervision during the maternal leave of Dr. Andrea Ode.

I want to thank Dr. Paul Zaslansky for the help with my work at the BESSYII synchrotron TXM and the acquired tomographic data.

I especially and gratefully want to thank my two master students: Tugba Akcan and Janosch Schoon. You both provided major contributions to this work and helped me to achieve the goals that I set for my thesis.

I want to thank Andrea Sass, Martin Textor, Julian Braun, Kristin Strohschein, Taimoor Qazi and again Janosch Schoon for being the best colleagues ever, for the uncountable times we drowned our frustration in beer, for the even more uncountable times we shared our coffee break, for insightful conversations and for many more things that would exceed these pages capacity to describe.

I want to thank Antje Blankenstein, Dorit Jacobi, Lilliya Schumann, Mario Thiele and Gabriela Korus for excellent technical assistance at our labs.

I want to thank all members of the NanoDiaRa project. I especially want to thank Prof. Heinrich Hofmann for fruitful discussions, endless support and the introduction to dynamic magnetic fields. I want to thank Dr. Lionel Maurizi and Marie-Gabrielle Beuzellin for

insightful conversations on nanoparticles and for having a lot of fun together. I want to thank Prof. Jean Paul Vallee, Dr. Azza Gramoun and Dr. Lindsey for fruitful collaborative work.

I want to thank Prof. Peter Guttmann, Dr. Katja Henzler and Dr. Stephan Werner from the HZG TXM beamline at the BESSYII for the opportunity to use this amazing machine. Here, I especially want to thank Dr. Katja Henzler and Dr. Stephan Werner for the massive support in carrying out my experiments and for the interesting and insightful discussion during hour long data acquisition.

I want to thank Petra Schrade for her work on the TEM images and for having enough faith to let me operate the TEM myself. That was fun.

I want to thank all the clinicians that contributed to the work on MoM wear MNPs. Here, I especially want to thank Prof. Carsten Perka for initiating the project and Anastasia Rakow for her enthusiastic help on carrying out the project. And of course, I want to thank all the clinicians that helped gathering the precious and invaluable samples: M.D. M. Müller, M.D. G.Wassilew, M.D. M. Reinke, and M.D. M. Fritschken.

I want to thank my family and my friends for being there for me during my many hard times as a PhD student. It would be tedious to name all of you and your contributions. Just know: this tree wouldn't have been able to grow without a solid foundation, without roots.

At last, I want to thank my son Gustav for deflecting me from my work and constantly reminding me that there is more in life than nanoparticles and cells.

6. References

1. Grabowski P: Physiology of bone. *Endocrine development* 16, 32-48 (2009).
2. Datta HK, Ng WF, Walker JA, Tuck SP, Varanasi SS: The cell biology of bone metabolism. *Journal of clinical pathology* 61(5), 577-587 (2008).
3. Boskey AL: Current Concepts of the Physiology and Biochemistry of Calcification. *Clinical orthopaedics and related research* (157), 225-257 (1981).
4. Buckwalter JA, Glimcher MJ, Cooper RR, Recker R: Bone biology. I: Structure, blood supply, cells, matrix, and mineralization. *Instructional course lectures* 45, 371-386 (1996).
5. Glimcher MJ: The nature of the mineral component of bone and the mechanism of calcification. *Instructional course lectures* 36, 49-69 (1987).
6. U.S. National Cancer Institute's Surveillance EaER: Bone Physiology (http://training.seer.cancer.gov/anatomy/skeletal/tissue.html).
7. Wolff J: Das Gesetz der Transformation der Knochen. Hirschberg, Berlin. (1892).
8. Frost HM: Bone's mechanostat: a 2003 update. *The anatomical record. Part A, Discoveries in molecular, cellular, and evolutionary biology* 275(2), 1081-1101 (2003).
9. Piney A: The Anatomy Of The Bone Marrow: With Special Reference To The Distribution Of The Red Marrow. *The British Medical Journal* 2(3226), 792-795 (1922).
10. Dunnill MS, Anderson JA, Whitehea.R: Quantitative Histological Studies on Age Changes in Bone. *J Pathol Bacteriol* 94(2), 275-& (1967).
11. Park D, Spencer JA, Koh BI *et al.*: Endogenous bone marrow MSCs are dynamic, fate-restricted participants in bone maintenance and regeneration. *Cell stem cell* 10(3), 259-272 (2012).
12. Knothe Tate ML, Adamson JR, Tami AE, Bauer TW: The osteocyte. *The international journal of biochemistry & cell biology* 36(1), 1-8 (2004).
13. Marks SC, Jr., Popoff SN: Bone cell biology: the regulation of development, structure, and function in the skeleton. *The American journal of anatomy* 183(1), 1-44 (1988).
14. Kahn AJ, Simmons DJ: Investigation of cell lineage in bone using a chimaera of chick and quail embryonic tissue. *Nature* 258(5533), 325-327 (1975).
15. Jotereau FV, Le Douarin NM: The developmental relationship between osteocytes and osteoclasts: A study using the quail-chick nuclear marker in endochondral ossification. *Developmental biology* 63(2), 253-265 (1978).
16. Wada T, Nakashima T, Hiroshi N, Penninger JM: RANKL-RANK signaling in osteoclastogenesis and bone disease. *Trends Mol Med* 12(1), 17-25 (2006).
17. Yoshida H, Hayashi S, Kunisada T *et al.*: The murine mutation osteopetrosis is in the coding region of the macrophage colony stimulating factor gene. *Nature* 345(6274), 442-444 (1990).
18. Proff P, Romer P: The molecular mechanism behind bone remodelling: a review. *Clin Oral Invest* 13(4), 355-362 (2009).
19. Vaananen HK, Laitala-Leinonen T: Osteoclast lineage and function. *Arch Biochem Biophys* 473(2), 132-138 (2008).
20. Saftig P, Hunziker E, Everts V *et al.*: Functions of cathepsin K in bone resorption - Lessons from cathepsin K deficient mice. *Cellular Peptidases in Immune Functions and Diseases 2* 477, 293-303 (2000).
21. Delaisse JM, Engsig MT, Everts V *et al.*: Proteinases in bone resorption: obvious and less obvious roles. *Clinica Chimica Acta* 291(2), 223-234 (2000).
22. Lee MH, Kim YJ, Kim HJ *et al.*: BMP-2-induced Runx2 expression is mediated by Dlx5, and TGF-beta 1 opposes the BMP-2-induced osteoblast differentiation by suppression of Dlx5 expression. *Journal of Biological Chemistry* 278(36), 34387-34394 (2003).
23. Lee MH, Kwon TG, Park HS, Wozney JM, Ryoo HM: BMP-2-induced Osterix expression is mediated by Dlx5 but is independent of Runx2. *Biochemical and biophysical research communications* 309(3), 689-694 (2003).

24. Matsuo K, Irie N: Osteoclast-osteoblast communication. *Arch Biochem Biophys* 473(2), 201-209 (2008).
25. Hill PA: Bone remodelling. *British journal of orthodontics* 25(2), 101-107 (1998).
26. Franz-Odendaal TA, Hall BK, Witten PE: Buried alive: how osteoblasts become osteocytes. *Developmental dynamics : an official publication of the American Association of Anatomists* 235(1), 176-190 (2006).
27. John J. Callaghan AGR, Harry E. Rubash The Adult Hip. (2006).
28. Pabinger C, Geissler A: Utilization rates of hip arthroplasty in OECD countries. *Osteoarthritis and cartilage / OARS, Osteoarthritis Research Society* 22(6), 734-741 (2014).
29. Bennell KL, Creaby MW, Wrigley TV *et al.*: Bone marrow lesions are related to dynamic knee loading in medial knee osteoarthritis. *Ann Rheum Dis* 69(6), 1151-1154 (2010).
30. Kerin A, Patwari P, Kuettner K, Cole A, Grodzinsky A: Molecular basis of osteoarthritis: biomechanical aspects. *Cellular and molecular life sciences : CMLS* 59(1), 27-35 (2002).
31. Heinegard D, Saxne T: The role of the cartilage matrix in osteoarthritis. *Nat Rev Rheumatol* 7(1), 50-56 (2011).
32. Lotz MK, Kraus VB: New developments in osteoarthritis. Posttraumatic osteoarthritis: pathogenesis and pharmacological treatment options. *Arthritis research & therapy* 12(3), 211 (2010).
33. Barton A, Worthington J: Genetic susceptibility to rheumatoid arthritis: an emerging picture. *Arthritis and rheumatism* 61(10), 1441-1446 (2009).
34. Scott DL, Wolfe F, Huizinga TW: Rheumatoid arthritis. *Lancet* 376(9746), 1094-1108 (2010).
35. Feldmann M, Brennan FM, Maini RN: Rheumatoid arthritis. *Cell* 85(3), 307-310 (1996).
36. Fournier C: Where do T cells stand in rheumatoid arthritis? *Joint, bone, spine : revue du rhumatisme* 72(6), 527-532 (2005).
37. Mor A, Abramson SB, Pillinger MH: The fibroblast-like synovial cell in rheumatoid arthritis: a key player in inflammation and joint destruction. *Clin Immunol* 115(2), 118-128 (2005).
38. Cardozo JB, Andrade DM, Santiago MB: The use of bisphosphonate in the treatment of avascular necrosis: a systematic review. *Clinical rheumatology* 27(6), 685-688 (2008).
39. Sampson S, Botto-Van Bemden A, Aufiero D: Stem Cell Therapies for Treatment of Cartilage and Bone Disorders: Osteoarthritis, Avascular Necrosis, and Non-union Fractures. *PM & R : the journal of injury, function, and rehabilitation* 7(4 Suppl), S26-32 (2015).
40. Lieberman JR, Engstrom SM, Meneghini RM, Soohoo NF: Which factors influence preservation of the osteonecrotic femoral head? *Clinical orthopaedics and related research* 470(2), 525-534 (2012).
41. Aldridge JM, 3rd, Urbaniak JR: Avascular necrosis of the femoral head: etiology, pathophysiology, classification, and current treatment guidelines. *American journal of orthopedics* 33(7), 327-332 (2004).
42. Houdek MT, Wyles CC, Martin JR, Sierra RJ: Stem cell treatment for avascular necrosis of the femoral head: current perspectives. *Stem cells and cloning : advances and applications* 7, 65-70 (2014).
43. Openstax: Synovial Joints (http://cnx.org/contents/6c5b58ca-6c6d-4ab3-8b41-60c8733a3144@4/Synovial_Joints). (Acessed: 05.06.2015).
44. Colter DC, Class R, Digirolamo CM, Prockop DJ: Rapid expansion of recycling stem cells in cultures of plastic-adherent cells from human bone marrow. *Proceedings of the National Academy of Sciences of the United States of America* 97(7), 3213-3218 (2000).
45. Pittenger MF, Mackay AM, Beck SC *et al.*: Multilineage potential of adult human mesenchymal stem cells. *Science* 284(5411), 143-147 (1999).
46. Dominici M, Le Blanc K, Mueller I *et al.*: Minimal criteria for defining multipotent mesenchymal stromal cells. The International Society for Cellular Therapy position statement. *Cytotherapy* 8(4), 315-317 (2006).
47. Son BR, Marquez-Curtis LA, Kucia M *et al.*: Migration of bone marrow and cord blood mesenchymal stem cells in vitro is regulated by stromal-derived factor-1-CXCR4 and

hepatocyte growth factor-c-met axes and involves matrix metalloproteinases. *Stem Cells* 24(5), 1254-1264 (2006).
48. Wynn RF, Hart CA, Corradi-Perini C *et al.*: A small proportion of mesenchymal stem cells strongly expresses functionally active CXCR4 receptor capable of promoting migration to bone marrow. 104, (2004).
49. Prockop DJ, Kota DJ, Bazhanov N, Reger RL: Evolving paradigms for repair of tissues by adult stem/progenitor cells (MSCs). *Journal of cellular and molecular medicine* 14(9), 2190-2199 (2010).
50. Ode A, Kopf J, Kurtz A *et al.*: CD73 and CD29 concurrently mediate the mechanically induced decrease of migratory capacity of mesenchymal stromal cells. *European cells & materials* 22, 26-42 (2011).
51. Jones E, Yang X: Mesenchymal stem cells and bone regeneration: current status. *Injury* 42(6), 562-568 (2011).
52. Oshita K, Yamaoka K, Udagawa N *et al.*: Human mesenchymal stem cells inhibit osteoclastogenesis through osteoprotegerin production. *Arthritis & Rheumatism* 63(6), 1658-1667 (2011).
53. Takayanagi H: Osteoimmunology: shared mechanisms and crosstalk between the immune and bone systems. *Nature reviews. Immunology* 7(4), 292-304 (2007).
54. Di Nicola M, Carlo-Stella C, Magni M *et al.*: Human bone marrow stromal cells suppress T-lymphocyte proliferation induced by cellular or nonspecific mitogenic stimuli. *Blood* 99(10), 3838-3843 (2002).
55. Jiang XX, Zhang Y, Liu B *et al.*: Human mesenchymal stem cells inhibit differentiation and function of monocyte-derived dendritic cells. *Blood* 105(10), 4120-4126 (2005).
56. Nauta AJ, Fibbe WE: Immunomodulatory properties of mesenchymal stromal cells. *Blood* 110(10), 3499-3506 (2007).
57. Spaggiari GM, Capobianco A, Becchetti S, Mingari MC, Moretta L: Mesenchymal stem cell-natural killer cell interactions: evidence that activated NK cells are capable of killing MSCs, whereas MSCs can inhibit IL-2-induced NK-cell proliferation. *Blood* 107(4), 1484-1490 (2006).
58. Liu Y, Wang L, Kikuiri T *et al.*: Mesenchymal stem cell-based tissue regeneration is governed by recipient T lymphocytes via IFN-gamma and TNF-alpha. *Nat Med* 17(12), 1594-1601 (2011).
59. Reinke S, Geissler S, Taylor WR *et al.*: Terminally differentiated CD8(+) T cells negatively affect bone regeneration in humans. *Science translational medicine* 5(177), 177ra136 (2013).
60. Mendez-Ferrer S, Michurina TV, Ferraro F *et al.*: Mesenchymal and haematopoietic stem cells form a unique bone marrow niche. *Nature* 466(7308), 829-834 (2010).
61. Granero-Molto F, Weis JA, Miga MI *et al.*: Regenerative effects of transplanted mesenchymal stem cells in fracture healing. *Stem Cells* 27(8), 1887-1898 (2009).
62. Chen FH, Tuan RS: Mesenchymal stem cells in arthritic diseases. *Arthritis research & therapy* 10(5), 223 (2008).
63. Murphy MB, Moncivais K, Caplan AI: Mesenchymal stem cells: environmentally responsive therapeutics for regenerative medicine. *Experimental & molecular medicine* 45, e54 (2013).
64. Griffin MD, Ryan AE, Alagesan S, Lohan P, Treacy O, Ritter T: Anti-donor immune responses elicited by allogeneic mesenchymal stem cells: what have we learned so far? *Immunol Cell Biol* 91(1), 40-51 (2013).
65. Ryan AE, Lohan P, O/'Flynn L *et al.*: Chondrogenic Differentiation Increases Antidonor Immune Response to Allogeneic Mesenchymal Stem Cell Transplantation. *Molecular therapy : the journal of the American Society of Gene Therapy* 22(3), 655-667 (2014).
66. Noth U, Steinert AF, Tuan RS: Technology insight: adult mesenchymal stem cells for osteoarthritis therapy. *Nature clinical practice. Rheumatology* 4(7), 371-380 (2008).
67. Murphy JM, Fink DJ, Hunziker EB, Barry FP: Stem cell therapy in a caprine model of osteoarthritis. *Arthritis and rheumatism* 48(12), 3464-3474 (2003).

68. Augello A, Tasso R, Negrini SM, Cancedda R, Pennesi G: Cell therapy using allogeneic bone marrow mesenchymal stem cells prevents tissue damage in collagen-induced arthritis. *Arthritis & Rheumatism* 56(4), 1175-1186 (2007).
69. Wakitani S, Mitsuoka T, Nakamura N, Toritsuka Y, Nakamura Y, Horibe S: Autologous bone marrow stromal cell transplantation for repair of full-thickness articular cartilage defects in human patellae: two case reports. *Cell transplantation* 13(5), 595-600 (2004).
70. Kuroda R, Ishida K, Matsumoto T *et al.*: Treatment of a full-thickness articular cartilage defect in the femoral condyle of an athlete with autologous bone-marrow stromal cells. *Osteoarthritis and cartilage / OARS, Osteoarthritis Research Society* 15(2), 226-231 (2007).
71. Zhao D, Cui D, Wang B *et al.*: Treatment of early stage osteonecrosis of the femoral head with autologous implantation of bone marrow-derived and cultured mesenchymal stem cells. *Bone* 50(1), 325-330 (2012).
72. Sen RK, Tripathy SK, Aggarwal S, Marwaha N, Sharma RR, Khandelwal N: Early results of core decompression and autologous bone marrow mononuclear cells instillation in femoral head osteonecrosis: a randomized control study. *The Journal of arthroplasty* 27(5), 679-686 (2012).
73. Lim YW, Kim YS, Lee JW, Kwon SY: Stem cell implantation for osteonecrosis of the femoral head. *Experimental & molecular medicine* 45, e61 (2013).
74. Ponomarev V: Nuclear imaging of cancer cell therapies. *Journal of nuclear medicine : official publication, Society of Nuclear Medicine* 50(7), 1013-1016 (2009).
75. Bhirde A, Xie J, Swierczewska M, Chen X: Nanoparticles for cell labeling. *Nanoscale* 3(1), 142-153 (2011).
76. Cohen B, Ziv K, Plaks V, Harmelin A, Neeman M: Ferritin nanoparticles as magnetic resonance reporter gene. *Wiley interdisciplinary reviews. Nanomedicine and nanobiotechnology* 1(2), 181-188 (2009).
77. Xie J, Chen K, Chen X: Production, Modification and Bio-Applications of Magnetic Nanoparticles Gestated by Magnetotactic Bacteria. *Nano research* 2(4), 261-278 (2009).
78. Gould SJ, Subramani S: Firefly luciferase as a tool in molecular and cell biology. *Analytical biochemistry* 175(1), 5-13 (1988).
79. Tang F, Barbacioru C, Bao S *et al.*: Tracing the derivation of embryonic stem cells from the inner cell mass by single-cell RNA-Seq analysis. *Cell stem cell* 6(5), 468-478 (2010).
80. Gambhir SS, Herschman HR, Cherry SR *et al.*: Imaging transgene expression with radionuclide imaging technologies. *Neoplasia* 2(1-2), 118-138 (2000).
81. Schafer R: Labeling and Imaging of Stem Cells - Promises and Concerns. *Transfusion medicine and hemotherapy : offizielles Organ der Deutschen Gesellschaft fur Transfusionsmedizin und Immunhamatologie* 37(2), 85-89 (2010).
82. Learmonth ID, Young C, Rorabeck C: The operation of the century: total hip replacement. *Lancet* 370(9597), 1508-1519 (2007).
83. Wales NJRFEA: 11th annual report. (2014).
84. Brown TS, Banerjee S, Russell RD, Mont MA, Huo MH: What's New in Total Hip Arthroplasty. 96, (2014).
85. Jeffers JR, Walter WL: Ceramic-on-ceramic bearings in hip arthroplasty: state of the art and the future. *The Journal of bone and joint surgery. British volume* 94(6), 735-745 (2012).
86. Krishnan H, Krishnan SP, Blunn G, Skinner JA, Hart AJ: Modular neck femoral stems. *The bone & joint journal* 95-B(8), 1011-1021 (2013).
87. Shimmin A, Beaule PE, Campbell P: Metal-on-metal hip resurfacing arthroplasty. *The Journal of bone and joint surgery. American volume* 90(3), 637-654 (2008).
88. Smith AJ, Dieppe P, Vernon K *et al.*: Failure rates of stemmed metal-on-metal hip replacements: analysis of data from the National Joint Registry of England and Wales. *Lancet* 379(9822), 1199-1204 (2012).
89. Smith AJ, Dieppe P, Howard PW, Blom AW, Wales NJRE: Failure rates of metal-on-metal hip resurfacings: analysis of data from the National Joint Registry for England and Wales. *Lancet* 380(9855), 1759-1766 (2012).

90. Healthbase.Com: Hip Implant in Total Hip Arthroplasty (http://www.healthbase.com/resources/orthopedics/total-hip-replacement-surgery-implants/frequently-asked-questions-faqs-total-hip-replacement-surgery-implants-india-mexico-price-cost.html). (Acessed: 05.06.2015).
91. Administration USFaD: Metal-on-Metal implant systems (http://www.fda.gov/MedicalDevices/ProductsandMedicalProcedures/ImplantsandProstheticsMetalonMetalHipImplants/). (Acessed: 05.06.2015).
92. Dobbs HS: Survivorship of total hip replacements. *The Journal of bone and joint surgery. British volume* 62-B(2), 168-173 (1980).
93. Willert HG, Semlitsch M: Reactions of the articular capsule to wear products of artificial joint prostheses. *Journal of biomedical materials research* 11(2), 157-164 (1977).
94. Harris WH, Schiller AL, Scholler JM, Freiberg RA, Scott R: Extensive localized bone resorption in the femur following total hip replacement. *The Journal of bone and joint surgery. American volume* 58(5), 612-618 (1976).
95. Ingham E, Fisher J: Biological reactions to wear debris in total joint replacement. *Proceedings of the Institution of Mechanical Engineers. Part H, Journal of engineering in medicine* 214(1), 21-37 (2000).
96. Walker PS, Gold BL: The tribology (friction, lubrication and wear) of all-metal artificial hip joints. 1971. *Clinical orthopaedics and related research* (329 Suppl), S4-10 (1996).
97. Anissian HL, Stark A, Gustafson A, Good V, Clarke IC: Metal-on-metal bearing in hip prosthesis generates 100-fold less wear debris than metal-on-polyethylene. *Acta orthopaedica Scandinavica* 70(6), 578-582 (1999).
98. Goldsmith AA, Dowson D, Isaac GH, Lancaster JG: A comparative joint simulator study of the wear of metal-on-metal and alternative material combinations in hip replacements. *Proceedings of the Institution of Mechanical Engineers. Part H, Journal of engineering in medicine* 214(1), 39-47 (2000).
99. Muller ME: The benefits of metal-on-metal total hip replacements. *Clinical orthopaedics and related research* (311), 54-59 (1995).
100. Park Y-S, Moon Y-W, Lim S-J, Yang J-M, Ahn G, Choi Y-L: Early Osteolysis Following Second-Generation Metal-on-Metal Hip Replacement. 87, (2005).
101. Union TE: Scientific Committee on Emerging and Newly Identified Health Risks: The safety of Metal-on-Metal joint replacements with a particular focus on hip implants (2014).
102. Doorn PF, Campbell PA, Worrall J, Benya PD, Mckellop HA, Amstutz HC: Metal wear particle characterization from metal on metal total hip replacements: transmission electron microscopy study of periprosthetic tissues and isolated particles. *Journal of biomedical materials research* 42(1), 103-111 (1998).
103. Buzea C, Pacheco II, Robbie K: Nanomaterials and nanoparticles: Sources and toxicity. *Biointerphases* 2(4), Mr17-Mr71 (2007).
104. Comission TE: Comission recommendation of 18 October 2011 on the definition of nanomaterial (2011/696/EU). (2011).
105. Krug HF, Wick P: Nanotoxicology: an interdisciplinary challenge. *Angew Chem Int Ed Engl* 50(6), 1260-1278 (2011).
106. Roduner E: Size matters: why nanomaterials are different. *Chemical Society reviews* 35(7), 583-592 (2006).
107. Rössler A, Skillas, G. And Pratsinis, S. E.: Nanopartikel — Materialien der Zukunft: Maßgeschneiderte Werkstoffe. *Chemie in unserer Zeit* 35(1), 32-41 (2001).
108. Roduner E: Nanoscopic Materials: Size-Dependent Phenomena. (2006).
109. Brus LE: Electron–electron and electron-hole interactions in small semiconductor crystallites: The size dependence of the lowest excited electronic state. *The Journal of chemical physics* 80(9), 4403-4409 (1984).
110. Wegner KD, Hildebrandt N: Quantum dots: bright and versatile in vitro and in vivo fluorescence imaging biosensors. *Chemical Society reviews*, (2015).

111. Raab CS, M.; Gazsó, A.; Fiedeler, U.; Nentwich, M. : What are synthetic nanoparticles? *NanoTrust Dossier* 02, (2011).
112. Wigginton NS, Haus KL, Hochella MF: Aquatic environmental nanoparticles. *J Environ Monitor* 9(12), 1306-1316 (2007).
113. Akbarzadeh A, Samiei M, Davaran S: Magnetic nanoparticles: preparation, physical properties, and applications in biomedicine. *Nanoscale research letters* 7(1), 144 (2012).
114. Brantley SW, T.S.; White, A.F.; Sparks, D.; Richter, D.; Pregitzer, K.; Derry, L.; Chorover, J.; Chadwick, O.; April, R.; Anderson, S.; Amundson, R.: Frontiers in Exploration of the Critical Zone: Report of a workshop sponsored by the National Science Foundation (NSF), October 24-26, 2005. (2006).
115. Hochella MF, Jr., Lower SK, Maurice PA *et al.*: Nanominerals, mineral nanoparticles, and Earth systems. *Science* 319(5870), 1631-1635 (2008).
116. Nowack B, Bucheli TD: Occurrence, behavior and effects of nanoparticles in the environment. *Environmental Pollution* 150(1), 5-22 (2007).
117. Sadowski Z: Biosynthesis and application of silver and gold nanoparticles. (2010).
118. Giere R, Querol X: Solid Particulate Matter in the Atmosphere. *Elements* 6(4), 215-222 (2010).
119. Afshari A, Matson U, Ekberg LE: Characterization of indoor sources of fine and ultrafine particles: a study conducted in a full-scale chamber. *Indoor Air* 15(2), 141-150 (2005).
120. Kocbach A, Li Y, Yttri KE, Cassee FR, Schwarze PE, Namork E: Physicochemical characterisation of combustion particles from vehicle exhaust and residential wood smoke. *Particle and fibre toxicology* 3, 1 (2006).
121. Donaldson K, Tran L, Jimenez LA *et al.*: Combustion-derived nanoparticles: a review of their toxicology following inhalation exposure. *Particle and fibre toxicology* 2, 10 (2005).
122. Leonard SS, Chen BT, Stone SG *et al.*: Comparison of stainless and mild steel welding fumes in generation of reactive oxygen species. *Particle and fibre toxicology* 7, 32 (2010).
123. Stefani D, Wardman D, Lambert T: The implosion of the Calgary General Hospital: ambient air quality issues. *Journal of the Air & Waste Management Association* 55(1), 52-59 (2005).
124. Sioutas C, Delfino RJ, Singh M: Exposure assessment for atmospheric ultrafine particles (UFPs) and implications in epidemiologic research. *Environmental health perspectives* 113(8), 947-955 (2005).
125. Taylor DA: Dust in the wind. *Environmental health perspectives* 110(2), A80-87 (2002).
126. Horikoshi S, Serpone N: *Introduction to Nanoparticles*. In: *Microwaves in Nanoparticle Synthesis*, (Ed.^(Eds). Wiley-VCH Verlag GmbH & Co. KGaA, 1-24 (2013).
127. Freestone I, Meeks N, Sax M, Higgitt C: The Lycurgus Cup — A Roman nanotechnology. *Gold Bull* 40(4), 270-277 (2007).
128. Perez-Arantegui J, Molera J, Larrea A *et al.*: Luster pottery from the thirteenth century to the sixteenth century: A nanostructured thin metallic film. *J Am Ceram Soc* 84(2), 442-446 (2001).
129. Daniel MC, Astruc D: Gold nanoparticles: Assembly, supramolecular chemistry, quantum-size-related properties, and applications toward biology, catalysis, and nanotechnology. *Chemical reviews* 104(1), 293-346 (2004).
130. Kessler R: Engineered nanoparticles in consumer products: understanding a new ingredient. *Environmental health perspectives* 119(3), a120-125 (2011).
131. Mueller NC, Nowack B: Exposure modeling of engineered nanoparticles in the environment. *Environmental science & technology* 42(12), 4447-4453 (2008).
132. Chan WC, Maxwell DJ, Gao X, Bailey RE, Han M, Nie S: Luminescent quantum dots for multiplexed biological detection and imaging. *Current opinion in biotechnology* 13(1), 40-46 (2002).
133. Neuberger T, Schöpf B, Hofmann H, Hofmann M, Von Rechenberg B: Superparamagnetic nanoparticles for biomedical applications: Possibilities and limitations of a new drug delivery system. *J Magn Magn Mater* 293(1), 483-496 (2005).
134. Dykman L, Khlebtsov N: Gold nanoparticles in biomedical applications: recent advances and perspectives. *Chemical Society reviews* 41(6), 2256-2282 (2012).

135. Hansen SF, Maynard A, Baun A, Tickner JA: Late lessons from early warnings for nanotechnology. *Nature nanotechnology* 3(8), 444-447 (2008).
136. Kunzmann A, Andersson B, Thurnherr T, Krug H, Scheynius A, Fadeel B: Toxicology of engineered nanomaterials: focus on biocompatibility, biodistribution and biodegradation. *Biochimica et biophysica acta* 1810(3), 361-373 (2011).
137. Elsaesser A, Howard CV: Toxicology of nanoparticles. *Advanced drug delivery reviews* 64(2), 129-137 (2012).
138. Nel A, Xia T, Madler L, Li N: Toxic potential of materials at the nanolevel. *Science* 311(5761), 622-627 (2006).
139. Seaton A, Donaldson K: Nanoscience, nanotoxicology, and the need to think small. *Lancet* 365(9463), 923-924 (2005).
140. Anderson RM, May RM: Coevolution of hosts and parasites. *Parasitology* 85(02), 411-426 (1982).
141. Marques JT, Carthew RW: A call to arms: coevolution of animal viruses and host innate immune responses. *Trends in Genetics* 23(7), 359-364 (2007).
142. Switzer WM, Salemi M, Shanmugam V *et al.*: Ancient co-speciation of simian foamy viruses and primates. *Nature* 434(7031), 376-380 (2005).
143. Li M, Al-Jamal KT, Kostarelos K, Reineke J: Physiologically based pharmacokinetic modeling of nanoparticles. *ACS nano* 4(11), 6303-6317 (2010).
144. Moghimi SM, Hunter AC, Andresen TL: Factors controlling nanoparticle pharmacokinetics: an integrated analysis and perspective. *Annual review of pharmacology and toxicology* 52, 481-503 (2012).
145. Nohynek GJ, Lademann J, Ribaud C, Roberts MS: Grey goo on the skin? Nanotechnology, cosmetic and sunscreen safety. *Critical reviews in toxicology* 37(3), 251-277 (2007).
146. Yamago S, Tokuyama H, Nakamura E *et al.*: In vivo biological behavior of a water-miscible fullerene: 14C labeling, absorption, distribution, excretion and acute toxicity. *Chemistry & biology* 2(6), 385-389 (1995).
147. Kreyling WG, Semmler M, Erbe F *et al.*: Translocation of ultrafine insoluble iridium particles from lung epithelium to extrapulmonary organs is size dependent but very low. *Journal of toxicology and environmental health. Part A* 65(20), 1513-1530 (2002).
148. Geiser M, Kreyling WG: Deposition and biokinetics of inhaled nanoparticles. *Particle and fibre toxicology* 7, 2 (2010).
149. Kreyling WG, Semmler-Behnke M, Seitz J *et al.*: Size dependence of the translocation of inhaled iridium and carbon nanoparticle aggregates from the lung of rats to the blood and secondary target organs. *Inhalation toxicology* 21 Suppl 1, 55-60 (2009).
150. Aggarwal P, Hall JB, Mcleland CB, Dobrovolskaia MA, Mcneil SE: Nanoparticle interaction with plasma proteins as it relates to particle biodistribution, biocompatibility and therapeutic efficacy. *Advanced drug delivery reviews* 61(6), 428-437 (2009).
151. Owens Iii DE, Peppas NA: Opsonization, biodistribution, and pharmacokinetics of polymeric nanoparticles. *International journal of pharmaceutics* 307(1), 93-102 (2006).
152. Bartneck M, Keul HA, Zwadlo-Klarwasser G, Groll J: Phagocytosis independent extracellular nanoparticle clearance by human immune cells. *Nano letters* 10(1), 59-63 (2010).
153. Brinkmann V, Zychlinsky A: Beneficial suicide: why neutrophils die to make NETs. *Nat Rev Microbiol* 5(8), 577-582 (2007).
154. Wick P, Malek A, Manser P *et al.*: Barrier capacity of human placenta for nanosized materials. *Environmental health perspectives* 118(3), 432-436 (2010).
155. Kreuter J: Influence of the surface properties on nanoparticle-mediated transport of drugs to the brain. *Journal of nanoscience and nanotechnology* 4(5), 484-488 (2004).
156. Deng ZJ, Liang M, Monteiro M, Toth I, Minchin RF: Nanoparticle-induced unfolding of fibrinogen promotes Mac-1 receptor activation and inflammation. *Nature nanotechnology* 6(1), 39-44 (2011).

157. Keegan GM, Learmonth ID, Case CP: Orthopaedic metals and their potential toxicity in the arthroplasty patient: A review of current knowledge and future strategies. *The Journal of bone and joint surgery. British volume* 89(5), 567-573 (2007).
158. Chen N, He Y, Su Y *et al.*: The cytotoxicity of cadmium-based quantum dots. *Biomaterials* 33(5), 1238-1244 (2012).
159. Verma A, Stellacci F: Effect of surface properties on nanoparticle-cell interactions. *Small* 6(1), 12-21 (2010).
160. Mortensen NP, Hurst GB, Wang W, Foster CM, Nallathamby PD, Retterer ST: Dynamic development of the protein corona on silica nanoparticles: composition and role in toxicity. *Nanoscale* 5(14), 6372-6380 (2013).
161. Monopoli MP, Walczyk D, Campbell A *et al.*: Physical-chemical aspects of protein corona: relevance to in vitro and in vivo biological impacts of nanoparticles. *Journal of the American Chemical Society* 133(8), 2525-2534 (2011).
162. Lesniak A, Fenaroli F, Monopoli MP, Aberg C, Dawson KA, Salvati A: Effects of the presence or absence of a protein corona on silica nanoparticle uptake and impact on cells. *ACS nano* 6(7), 5845-5857 (2012).
163. Schrurs F, Lison D: Focusing the research efforts. *Nature nanotechnology* 7(9), 546-548 (2012).
164. Teeguarden JG, Hinderliter PM, Orr G, Thrall BD, Pounds JG: Particokinetics in vitro: dosimetry considerations for in vitro nanoparticle toxicity assessments. *Toxicological sciences : an official journal of the Society of Toxicology* 95(2), 300-312 (2007).
165. Khanbeigi RA, Kumar A, Sadouki F *et al.*: The delivered dose: Applying particokinetics to in vitro investigations of nanoparticle internalization by macrophages. *Journal of Controlled Release* 162(2), 259-266 (2012).
166. Hinderliter PM, Minard KR, Orr G *et al.*: ISDD: A computational model of particle sedimentation, diffusion and target cell dosimetry for in vitro toxicity studies. *Particle and fibre toxicology* 7(1), 36 (2010).
167. Monteiro-Riviere NA, Inman AO, Zhang LW: Limitations and relative utility of screening assays to assess engineered nanoparticle toxicity in a human cell line. *Toxicology and applied pharmacology* 234(2), 222-235 (2009).
168. Worle-Knirsch JM, Pulskamp K, Krug HF: Oops they did it again! Carbon nanotubes hoax scientists in viability assays. *Nano letters* 6(6), 1261-1268 (2006).
169. Han X, Gelein R, Corson N *et al.*: Validation of an LDH assay for assessing nanoparticle toxicity. *Toxicology* 287(1-3), 99-104 (2011).
170. Kroll A, Pillukat MH, Hahn D, Schnekenburger J: Current in vitro methods in nanoparticle risk assessment: limitations and challenges. *European journal of pharmaceutics and biopharmaceutics : official journal of Arbeitsgemeinschaft fur Pharmazeutische Verfahrenstechnik e.V* 72(2), 370-377 (2009).
171. Fischer HC, Chan WC: Nanotoxicity: the growing need for in vivo study. *Current opinion in biotechnology* 18(6), 565-571 (2007).
172. Kasper J, Hermanns MI, Bantz C *et al.*: Inflammatory and cytotoxic responses of an alveolar-capillary coculture model to silica nanoparticles: comparison with conventional monocultures. *Particle and fibre toxicology* 8(1), 6 (2011).
173. Wottrich R, Diabate S, Krug HF: Biological effects of ultrafine model particles in human macrophages and epithelial cells in mono- and co-culture. *International journal of hygiene and environmental health* 207(4), 353-361 (2004).
174. Corot C, Robert P, Idee JM, Port M: Recent advances in iron oxide nanocrystal technology for medical imaging. *Advanced drug delivery reviews* 58(14), 1471-1504 (2006).
175. Wahajuddin, Arora S: Superparamagnetic iron oxide nanoparticles: magnetic nanoplatforms as drug carriers. *International journal of nanomedicine* 7, 3445-3471 (2012).
176. Kodama RH: Magnetic nanoparticles. *J Magn Magn Mater* 200(1-3), 359-372 (1999).

177. Dave SR, Gao X: Monodisperse magnetic nanoparticles for biodetection, imaging, and drug delivery: a versatile and evolving technology. *Wiley interdisciplinary reviews. Nanomedicine and nanobiotechnology* 1(6), 583-609 (2009).
178. Bañobre-López M, Teijeiro A, Rivas J: Magnetic nanoparticle-based hyperthermia for cancer treatment. *Reports of Practical Oncology and Radiotherapy* 18(6), 397-400 (2013).
179. Zhang E, Kircher MF, Koch M, Eliasson L, Goldberg SN, Renstrom E: Dynamic magnetic fields remote-control apoptosis via nanoparticle rotation. *ACS nano* 8(4), 3192-3201 (2014).
180. Roch A, Muller RN, Gillis P: Theory of proton relaxation induced by superparamagnetic particles. *Journal of Chemical Physics* 110(11), 5403-5411 (1999).
181. Muller RN, Gillis P, Moiny F, Roch A: Transverse Relaxivity of Particulate Mri Contrast-Media - from Theories to Experiments. *Magnet Reson Med* 22(2), 178-182 (1991).
182. Gossuin Y, Gillis P, Hocq A, Vuong QL, Roch A: Magnetic resonance relaxation properties of superparamagnetic particles. *Wiley interdisciplinary reviews. Nanomedicine and nanobiotechnology* 1(3), 299-310 (2009).
183. Wang YXJ, Hussain SM, Krestin GP: Superparamagnetic iron oxide contrast agents: physicochemical characteristics and applications in MR imaging. *European radiology* 11(11), 2319-2331 (2001).
184. Weissleder R, Stark DD, Engelstad BL *et al.*: Superparamagnetic iron oxide: pharmacokinetics and toxicity. *AJR. American journal of roentgenology* 152(1), 167-173 (1989).
185. Weissleder R, Elizondo G, Wittenberg J, Lee AS, Josephson L, Brady TJ: Ultrasmall superparamagnetic iron oxide: an intravenous contrast agent for assessing lymph nodes with MR imaging. *Radiology* 175(2), 494-498 (1990).
186. Metz S, Lohr S, Settles M *et al.*: Ferumoxtran-10-enhanced MR imaging of the bone marrow before and after conditioning therapy in patients with non-Hodgkin lymphomas. *European radiology* 16(3), 598-607 (2006).
187. Daldrup-Link HE, Rummeny EJ, Ihssen B, Kienast J, Link TM: Iron-oxide-enhanced MR imaging of bone marrow in patients with non-Hodgkin's lymphoma: differentiation between tumor infiltration and hypercellular bone marrow. *European radiology* 12(6), 1557-1566 (2002).
188. Simon GH, Raatschen HJ, Wendland MF *et al.*: Ultrasmall superparamagnetic iron-oxide-enhanced MR imaging of normal bone marrow in rodents: original research original research. *Academic radiology* 12(9), 1190-1197 (2005).
189. Panahifar A, Mahmoudi M, Doschak MR: Synthesis and in vitro evaluation of bone-seeking superparamagnetic iron oxide nanoparticles as contrast agents for imaging bone metabolic activity. *ACS applied materials & interfaces* 5(11), 5219-5226 (2013).
190. Pareta RA, Taylor E, Webster TJ: Increased osteoblast density in the presence of novel calcium phosphate coated magnetic nanoparticles. *Nanotechnology* 19(26), 265101 (2008).
191. Frank JA, Miller BR, Arbab AS *et al.*: Clinically applicable labeling of mammalian and stem cells by combining superparamagnetic iron oxides and transfection agents. *Radiology* 228(2), 480-487 (2003).
192. Bulte JW, Kraitchman DL: Monitoring cell therapy using iron oxide MR contrast agents. *Current pharmaceutical biotechnology* 5(6), 567-584 (2004).
193. Schafer R, Ayturan M, Bantleon R *et al.*: The use of clinically approved small particles of iron oxide (SPIO) for labeling of mesenchymal stem cells aggravates clinical symptoms in experimental autoimmune encephalomyelitis and influences their in vivo distribution. *Cell transplantation* 17(8), 923-941 (2008).
194. Arbab AS, Yocum GT, Kalish H *et al.*: Efficient magnetic cell labeling with protamine sulfate complexed to ferumoxides for cellular MRI. *Blood* 104(4), 1217-1223 (2004).
195. Kostura L, Kraitchman DL, Mackay AM, Pittenger MF, Bulte JW: Feridex labeling of mesenchymal stem cells inhibits chondrogenesis but not adipogenesis or osteogenesis. *NMR in biomedicine* 17(7), 513-517 (2004).
196. Henning TD, Sutton EJ, Kim A *et al.*: The influence of ferucarbotran on the chondrogenesis of human mesenchymal stem cells. *Contrast media & molecular imaging* 4(4), 165-173 (2009).

197. Van Buul GM, Farrell E, Kops N *et al.*: Ferumoxides-protamine sulfate is more effective than ferucarbotran for cell labeling: implications for clinically applicable cell tracking using MRI. *Contrast media & molecular imaging* 4(5), 230-236 (2009).
198. Ittrich H, Lange C, Togel F *et al.*: In vivo magnetic resonance imaging of iron oxide-labeled, arterially-injected mesenchymal stem cells in kidneys of rats with acute ischemic kidney injury: detection and monitoring at 3T. *Journal of magnetic resonance imaging : JMRI* 25(6), 1179-1191 (2007).
199. Corot C, Petry KG, Trivedi R *et al.*: Macrophage imaging in central nervous system and in carotid atherosclerotic plaque using ultrasmall superparamagnetic iron oxide in magnetic resonance imaging. *Investigative radiology* 39(10), 619-625 (2004).
200. Arbab AS, Yocum GT, Rad AM *et al.*: Labeling of cells with ferumoxides-protamine sulfate complexes does not inhibit function or differentiation capacity of hematopoietic or mesenchymal stem cells. *NMR in biomedicine* 18(8), 553-559 (2005).
201. Bulte JW, Kraitchman DL, Mackay AM, Pittenger MF: Chondrogenic differentiation of mesenchymal stem cells is inhibited after magnetic labeling with ferumoxides. *Blood* 104(10), 3410-3412; author reply 3412-3413 (2004).
202. Balakumaran A, Pawelczyk E, Ren J *et al.*: Superparamagnetic iron oxide nanoparticles labeling of bone marrow stromal (mesenchymal) cells does not affect their "stemness". *PloS one* 5(7), e11462 (2010).
203. Singh N, Jenkins GJ, Asadi R, Doak SH: Potential toxicity of superparamagnetic iron oxide nanoparticles (SPION). *Nano reviews* 1, (2010).
204. Lunov O, Syrovets T, Rocker C *et al.*: Lysosomal degradation of the carboxydextran shell of coated superparamagnetic iron oxide nanoparticles and the fate of professional phagocytes. *Biomaterials* 31(34), 9015-9022 (2010).
205. Delcroix GJ, Jacquart M, Lemaire L *et al.*: Mesenchymal and neural stem cells labeled with HEDP-coated SPIO nanoparticles: in vitro characterization and migration potential in rat brain. *Brain research* 1255, 18-31 (2009).
206. Reddy AM, Kwak BK, Shim HJ *et al.*: Functional characterization of mesenchymal stem cells labeled with a novel PVP-coated superparamagnetic iron oxide. *Contrast media & molecular imaging* 4(3), 118-126 (2009).
207. Chen CL, Zhang H, Ye Q *et al.*: A new nano-sized iron oxide particle with high sensitivity for cellular magnetic resonance imaging. *Molecular imaging and biology : MIB : the official publication of the Academy of Molecular Imaging* 13(5), 825-839 (2011).
208. Landazuri N, Tong S, Suo J *et al.*: Magnetic targeting of human mesenchymal stem cells with internalized superparamagnetic iron oxide nanoparticles. *Small* 9(23), 4017-4026 (2013).
209. Wang L, Neoh KG, Kang ET, Shuter B, Wang SC: Biodegradable magnetic-fluorescent magnetite/poly(dl-lactic acid-co-alpha,beta-malic acid) composite nanoparticles for stem cell labeling. *Biomaterials* 31(13), 3502-3511 (2010).
210. Chastellain M, Petri A, Hofmann H: Particle size investigations of a multistep synthesis of PVA coated superparamagnetic nanoparticles. *Journal of colloid and interface science* 278(2), 353-360 (2004).
211. Alves MH, Jensen BE, Smith AA, Zelikin AN: Poly(vinyl alcohol) physical hydrogels: new vista on a long serving biomaterial. *Macromolecular bioscience* 11(10), 1293-1313 (2011).
212. Baker MI, Walsh SP, Schwartz Z, Boyan BD: A review of polyvinyl alcohol and its uses in cartilage and orthopedic applications. *Journal of biomedical materials research. Part B, Applied biomaterials* 100(5), 1451-1457 (2012).
213. Petri-Fink A, Chastellain M, Juillerat-Jeanneret L, Ferrari A, Hofmann H: Development of functionalized superparamagnetic iron oxide nanoparticles for interaction with human cancer cells. *Biomaterials* 26(15), 2685-2694 (2005).
214. Cengelli F, Maysinger D, Tschudi-Monnet F *et al.*: Interaction of functionalized superparamagnetic iron oxide nanoparticles with brain structures. *The Journal of pharmacology and experimental therapeutics* 318(1), 108-116 (2006).

215. Chung TH, Wu SH, Yao M *et al.*: The effect of surface charge on the uptake and biological function of mesoporous silica nanoparticles in 3T3-L1 cells and human mesenchymal stem cells. *Biomaterials* 28(19), 2959-2966 (2007).
216. Petri-Fink A, Hofmann H: Superparamagnetic iron oxide nanoparticles (SPIONs): from synthesis to in vivo studies--a summary of the synthesis, characterization, in vitro, and in vivo investigations of SPIONs with particular focus on surface and colloidal properties. *IEEE transactions on nanobioscience* 6(4), 289-297 (2007).
217. Petri-Fink A, Steitz B, Finka A, Salaklang J, Hofmann H: Effect of cell media on polymer coated superparamagnetic iron oxide nanoparticles (SPIONs): colloidal stability, cytotoxicity, and cellular uptake studies. *European journal of pharmaceutics and biopharmaceutics : official journal of Arbeitsgemeinschaft fur Pharmazeutische Verfahrenstechnik e.V* 68(1), 129-137 (2008).
218. Cobelli N, Scharf B, Crisi GM, Hardin J, Santambrogio L: Mediators of the inflammatory response to joint replacement devices. *Nat Rev Rheumatol* 7(10), 600-608 (2011).
219. Brown C, Williams S, Tipper JL, Fisher J, Ingham E: Characterisation of wear particles produced by metal on metal and ceramic on metal hip prostheses under standard and microseparation simulation. *Journal of materials science. Materials in medicine* 18(5), 819-827 (2007).
220. Catelas I, Medley JB, Campbell PA, Huk OL, Bobyn JD: Comparison of in vitro with in vivo characteristics of wear particles from metal-metal hip implants. *Journal of biomedical materials research. Part B, Applied biomaterials* 70(2), 167-178 (2004).
221. Scharf B, Clement CC, Zolla V *et al.*: Molecular analysis of chromium and cobalt-related toxicity. *Scientific reports* 4, 5729 (2014).
222. Billi F, Benya P, Kavanaugh A, Adams J, Mckellop H, Ebramzadeh E: The John Charnley Award: an accurate and extremely sensitive method to separate, display, and characterize wear debris: part 2: metal and ceramic particles. *Clinical orthopaedics and related research* 470(2), 339-350 (2012).
223. Ito S, Matsumoto T, Enomoto H, Shindo H: Histological analysis and biological effects of granulation tissue around loosened hip prostheses in the development of osteolysis. *Journal of orthopaedic science : official journal of the Japanese Orthopaedic Association* 9(5), 478-487 (2004).
224. Pandit H, Glyn-Jones S, Mclardy-Smith P *et al.*: Pseudotumours associated with metal-on-metal hip resurfacings. *The Journal of bone and joint surgery. British volume* 90(7), 847-851 (2008).
225. Thomas P, Braathen LR, Dorig M *et al.*: Increased metal allergy in patients with failed metal-on-metal hip arthroplasty and peri-implant T-lymphocytic inflammation. *Allergy* 64(8), 1157-1165 (2009).
226. Gallo J, Goodman SB, Konttinen YT, Raska M: Particle disease: biologic mechanisms of periprosthetic osteolysis in total hip arthroplasty. *Innate immunity* 19(2), 213-224 (2013).
227. Jiang Y, Jia T, Gong W, Wooley PH, Yang SY: Effects of Ti, PMMA, UHMWPE, and Co-Cr wear particles on differentiation and functions of bone marrow stromal cells. *Journal of biomedical materials research. Part A* 101(10), 2817-2825 (2013).
228. Massart R, Dubois E, Cabuil V, Hasmonay E: Preparation and Properties of Monodisperse Magnetic Fluids. *J Magn Magn Mater* 149(1-2), 1-5 (1995).
229. Schulze K, Koch A, Schopf B *et al.*: Intraarticular application of superparamagnetic nanoparticles and their uptake by synovial membrane - an experimental study in sheep. *J Magn Magn Mater* 293(1), 419-432 (2005).
230. Schulze F, Dienelt A, Geissler S *et al.*: Amino-polyvinyl Alcohol Coated Superparamagnetic Iron Oxide Nanoparticles are Suitable for Monitoring of Human Mesenchymal Stromal Cells In Vivo. *Small*, (2014).
231. Pretsch E, Buhlmann P., Affolter C.: Structure Determination of Organic Compounds. Tables of Spectra Data. Springer, New York. (2000).

232. Mansur HS, Orefice RL, Mansur AaP: Characterization of poly(vinyl alcohol)/poly(ethylene glycol) hydrogels and PVA-derived hybrids by small-angle X-ray scattering and FTIR spectroscopy. *Polymer* 45(21), 7193-7202 (2004).
233. Zhang Y, Kohler N, Zhang M: Surface modification of superparamagnetic magnetite nanoparticles and their intracellular uptake. *Biomaterials* 23(7), 1553-1561 (2002).
234. Schneider CA, Rasband WS, Eliceiri KW: NIH Image to ImageJ: 25 years of image analysis. *Nature methods* 9(7), 671-675 (2012).
235. Schneider G, Guttmann P, Heim S *et al.*: Three-dimensional cellular ultrastructure resolved by X-ray microscopy. *Nature methods* 7(12), 985-987 (2010).
236. Schulze F, Crowe LA, Gramoun A *et al.*: Accumulation of amino-polyvinyl alcohol coated superparamagnetic iron oxide nanoparticles in bone marrow: implications for local stromal cells. *Nanomedicine (Lond)*, (2015 Manuscript accepted).
237. Geback T, Schulz MM, Koumoutsakos P, Detmar M: TScratch: a novel and simple software tool for automated analysis of monolayer wound healing assays. *BioTechniques* 46(4), 265-274 (2009).
238. Livak KJ, Schmittgen TD: Analysis of relative gene expression data using real-time quantitative PCR and the 2(-Delta Delta C(T)) Method. *Methods* 25(4), 402-408 (2001).
239. Dobson KR, Reading L, Haberey M, Marine X, Scutt A: Centrifugal isolation of bone marrow from bone: an improved method for the recovery and quantitation of bone marrow osteoprogenitor cells from rat tibiae and femurae. *Calcified tissue international* 65(5), 411-413 (1999).
240. Akcan T: Survival and function of mesenchymal stromal cells after exposure to superparamagnetic iron oxide nanoparticles in vivo. Master in Biotechnology, 85 (2013).
241. Kim YH, Yoon DS, Kim HO, Lee JW: Characterization of different subpopulations from bone marrow-derived mesenchymal stromal cells by alkaline phosphatase expression. *Stem cells and development* 21(16), 2958-2968 (2012).
242. Cartiera MS, Johnson KM, Rajendran V, Caplan MJ, Saltzman WM: The uptake and intracellular fate of PLGA nanoparticles in epithelial cells. *Biomaterials* 30(14), 2790-2798 (2009).
243. Andreas K, Georgieva R, Ladwig M *et al.*: Highly efficient magnetic stem cell labeling with citrate-coated superparamagnetic iron oxide nanoparticles for MRI tracking. *Biomaterials* 33(18), 4515-4525 (2012).
244. Oyama M, Tatlock A, Fukuta S *et al.*: Retrovirally transduced bone marrow stromal cells isolated from a mouse model of human osteogenesis imperfecta (oim) persist in bone and retain the ability to form cartilage and bone after extended passaging. *Gene therapy* 6(3), 321-329 (1999).
245. Shirley D, Marsh D, Jordan G, Mcquaid S, Li G: Systemic recruitment of osteoblastic cells in fracture healing. *Journal of orthopaedic research : official publication of the Orthopaedic Research Society* 23(5), 1013-1021 (2005).
246. Tamama K, Fan VH, Griffith LG, Blair HC, Wells A: Epidermal Growth Factor as a Candidate for Ex Vivo Expansion of Bone Marrow–Derived Mesenchymal Stem Cells. *STEM CELLS* 24(3), 686-695 (2006).
247. Ball SG, Shuttleworth CA, Kielty CM: Vascular endothelial growth factor can signal through platelet-derived growth factor receptors. *Journal of Cell Biology* 177(3), 489-500 (2007).
248. Vieira AV, Lamaze C, Schmid SL: Control of EGF receptor signaling by clathrin-mediated endocytosis. *Science* 274(5295), 2086-2089 (1996).
249. O'brien J, Wilson I, Orton T, Pognan F: Investigation of the Alamar Blue (resazurin) fluorescent dye for the assessment of mammalian cell cytotoxicity. *European journal of biochemistry / FEBS* 267(17), 5421-5426 (2000).
250. Gonzalez RJ, Tarloff JB: Evaluation of hepatic subcellular fractions for Alamar blue and MTT reductase activity. *Toxicology in vitro : an international journal published in association with BIBRA* 15(3), 257-259 (2001).

251. Kitamura S, Sugihara K, Ohta S: Drug-metabolizing ability of molybdenum hydroxylases. *Drug metabolism and pharmacokinetics* 21(2), 83-98 (2006).
252. Battelli MG, Bolognesi A, Polito L: Pathophysiology of circulating xanthine oxidoreductase: New emerging roles for a multi-tasking enzyme. *Biochimica et biophysica acta* 1842(9), 1502-1517 (2014).
253. Arora S, Rajwade JM, Paknikar KM: Nanotoxicology and in vitro studies: the need of the hour. *Toxicology and applied pharmacology* 258(2), 151-165 (2012).
254. Oberdorster G: Nanotoxicology: in vitro-in vivo dosimetry. *Environmental health perspectives* 120(1), A13; author reply A13 (2012).
255. Teeguarden JG, Mikheev VB, Minard KR *et al.*: Comparative iron oxide nanoparticle cellular dosimetry and response in mice by the inhalation and liquid cell culture exposure routes. *Particle and fibre toxicology* 11(1), 46 (2014).
256. Burke WT, Harris C: Total Cell Counts of the Bone Marrow of Normal Albino Rats from 1 to 50 Weeks of Age. *Blood* 14(4), 409-414 (1959).
257. Shi Z, Neoh KG, Kang ET *et al.*: (Carboxymethyl)chitosan-modified superparamagnetic iron oxide nanoparticles for magnetic resonance imaging of stem cells. *ACS applied materials & interfaces* 1(2), 328-335 (2009).
258. Lohmann CH, Meyer H, Nuechtern JV *et al.*: Periprosthetic tissue metal content but not serum metal content predicts the type of tissue response in failed small-diameter metal-on-metal total hip arthroplasties. *The Journal of bone and joint surgery. American volume* 95(17), 1561-1568 (2013).
259. Beraudi A, Catalani S, Montesi M *et al.*: Detection of cobalt in synovial fluid from metal-on-metal hip prosthesis: correlation with the ion haematic level. *Biomarkers : biochemical indicators of exposure, response, and susceptibility to chemicals* 18(8), 699-705 (2013).
260. De Smet K, De Haan R, Calistri A *et al.*: Metal ion measurement as a diagnostic tool to identify problems with metal-on-metal hip resurfacing. *The Journal of bone and joint surgery. American volume* 90 Suppl 4, 202-208 (2008).
261. Lass R, Grubl A, Kolb A *et al.*: Comparison of synovial fluid, urine, and serum ion levels in metal-on-metal total hip arthroplasty at a minimum follow-up of 18 years. *Journal of orthopaedic research : official publication of the Orthopaedic Research Society* 32(9), 1234-1240 (2014).
262. Case CP, Langkamer VG, James C *et al.*: Widespread dissemination of metal debris from implants. *The Journal of bone and joint surgery. British volume* 76(5), 701-712 (1994).
263. Davda K, Lali FV, Sampson B, Skinner JA, Hart AJ: An analysis of metal ion levels in the joint fluid of symptomatic patients with metal-on-metal hip replacements. *The Journal of bone and joint surgery. British volume* 93(6), 738-745 (2011).
264. Schoon J: Cobalt- and Chromium-ion exposition due to hip implant wear: Local levels and consequences for human mesenchymal stem cells in vitro. Master in Toxicology, 77 (2014).
265. Hsu SH, Chen CT, Wei YH: Inhibitory effects of hypoxia on metabolic switch and osteogenic differentiation of human mesenchymal stem cells. *Stem cells* 31(12), 2779-2788 (2013).
266. Volkmer E, Kallukalam BC, Maertz J *et al.*: Hypoxic preconditioning of human mesenchymal stem cells overcomes hypoxia-induced inhibition of osteogenic differentiation. *Tissue engineering. Part A* 16(1), 153-164 (2010).
267. Andrews RE, Shah KM, Wilkinson JM, Gartland A: Effects of cobalt and chromium ions at clinically equivalent concentrations after metal-on-metal hip replacement on human osteoblasts and osteoclasts: implications for skeletal health. *Bone* 49(4), 717-723 (2011).
268. Barceloux DG: Chromium. *Journal of toxicology. Clinical toxicology* 37(2), 173-194 (1999).
269. Su Y, Hu M, Fan C *et al.*: The cytotoxicity of CdTe quantum dots and the relative contributions from released cadmium ions and nanoparticle properties. *Biomaterials* 31(18), 4829-4834 (2010).

Selbständigkeitserklärung

Die Vorliegende Dissertation ist von mir selbst und ohne Hilfe Dritter verfasst worden. Sie stellt auch in Teilen keine Kopie von arbeiten anderer Autoren dar. Ich versichere, keine außer den hier angegebenen Hilfsmitteln und Literaturstellen verwendet zu haben.

I hereby declare that this thesis has been written by me and without the help of third parties. The current work is not an entire or partial copy of other authors' work. I declare that I have not used any tools or references except those cited in this work.

Berlin, den

Frank Schulze